INTEGRATED OPTOFLUIDIC PARTICLE MANIPULATION

by

JUSTIN THOMAS BLAKELY

B.S., University of California, Irvine, 2005

A Thesis Submitted in Partial Fulfillment
of the Requirements for the Degree of

MASTER OF APPLIED SCIENCE

in the Department of Electrical and Computer Engineering

SUPERVISORY COMMITTEE

INTEGRATED OPTOFLUIDIC PARTICLE MANIPULATION

by

JUSTIN THOMAS BLAKELY
B.S., University of California, 2005

Supervisory Committee

Dr. Reuven Gordon (Department of Electrical and Computer Engineering)
Supervisor

Dr. David Sinton (Department of Mechanical Engineering)
Co-Supervisor

Dr. Colin Bradley (Department of Mechanical Engineering)
Outside Member

ABSTRACT

SUPERVISORY COMMITTEE

Dr. Reuven Gordon, (Department of Electrical and Computer Engineering)
Supervisor

Dr. David Sinton (Department of Mechanical Engineering)
Co- Supervisor

Dr. Colin Bradley (Department of Mechanical Engineering)
Outside Member

Optical confinement and manipulation of matter, or optical trapping, is widely adopted at micro-scales as a research tool in disciplines of biology, engineering, and physics. Microfluidic systems are attractive from the standpoint of low sample volumes, laminar flow, and viscous damping and offer an ideal environment for trapping of miniaturized objects and microorganisms. Various trapping configurations are presented in this thesis using a custom fabricated consumer-grade optofluidic chip and are of significant scientific and practical importance.

Microfluidics and fiber optics are integrated in-plane to achieve several flow-dependent particle trapping mechanisms on-chip. Each mechanism results from a combination of fluid drag and optical scattering forces. Parallel and offset fibers, orthogonally oriented to the flow, show cyclic cross-stream particle transit with flow-dependent particle trajectories and loss. Upstream-angled fibers with flow result in circulatory particle trajectories. Asymmetric angled fibers result in continuous particle circulation whereas symmetry with respect to the flow axis enables both stable trapping and circulation modes. Stable trapping of single particles, self-guided multi-particle arrays and stacked particle assemblies are demonstrated with a single upstream-oriented fiber. Size tuning of trapped multiple particle assemblies is also presented. The planar interaction of fluid

drag and optical forces results in novel possibilities for cost-effective on-chip diagnostics, mixing, flow rate monitoring, and cell analysis.

An opto-hydrodynamic theory is adopted to verify experimentally observed particle array dynamics in a dual-beam fiber-optic trap. When applied to dielectric microsphere particles, the theory confirms the inhomogeneous self-organization and the spontaneous emergence of self-sustained oscillations in particle arrays. In the presence of small-scale symmetry-breaking, self-sustained oscillations are shown to occur spontaneously from an exchange between the optical scattering and the gradient optical forces, in the absence of inertia that is central to the dynamics of ion traps. Experimental results show non-uniform equilibrium particle spacing and spontaneous self-sustained oscillation for large particle numbers. Self-organization and oscillation is of general interest to other systems involving multi-particle optical interactions.

TABLE OF CONTENTS

List of Tables

List of Figures

ACKNOWLEDGEMENT

Grateful acknowledgement is due to those who made this study possible: Dr. Jinye Zhang for his technical assistance with optical devices and overall moral support; Dr. Mitsunori Kawano for his timeless development and implementation of an opto-hydrodynamic theory for the simulation of optically bound particles; to Professor Reuven Gordon for his untold persistence and technical advice; and to Professor David Sinton for his friendly encouragement, generosity with time allocation, and transfer of written technical skills. Continued gratitude is expressed to my supervisors and CAMTEC for generously granting research and conference-related funding. Additional appreciate is directed to my father, Dr. Thomas A. Blakely Jr., and grandfather, Dr. Thomas A. Blakely Sr., for encouraging me academically throughout the years.

DEDICATION

In loving memory of my father

CHAPTER 1

INTRODUCTION

1.1 OPTOFLUIDICS

The trapping, or tweezing, of particles has been of great interest to science and engineering [1-4] since Ashkin demonstrated trapping of dielectric particles using radiation forces produced by continuous laser beams [5]. Microfluidics [6] is a rapidly emerging field which aims to create lab-on-chip capability for bioanalysis and other applications [7, 8], with advantages towards low-cost biochip integration, portability, low sample volumes, and parallel processing of the analyte. Several researchers have considered integrating optics in the microfluidic environment, which has spawned the field of optofluidics [9-11]. Light emitted from optical fibers imparts momentum to dielectric matter and is used to control the dynamics of particles in stream. Optical and drag forces show distinct flow and power dependencies and represent two independent handles on particle control and a variety of potential lab-on-chip applications. In this work we demonstrate particle manipulation inside a fabricated polydimethylsiloxane (PDMS) optofluidic chip, where optical and hydrodynamic forces interact to enable selective particle control, *i.e.* power- and flow-dependent displacement, particle oscillation, array formation, waveguiding, and size reduction of particle chains. In cases involving multiple fiber integration, intentionally applied biases in fiber orientation enable distinct single and multi-particle rotation while interacting with applied flow. Optical binding, or the self-organization of particles forming an array, is also demonstrated in a dual-beam optical trap using counter-propagating fiber beams. Two types of inhomogeneous particle spacing and the onset of spontaneous array oscillation are experimentally determined and verified with an opto-hydrodynamic theory.

1.2 Motivation

In the past several years, there has been increasing interest towards the integration of optical delivery directly into a microfluidic lab-on-chip for non-contact manipulation of species with enhanced functionality. On-chip optical integration greatly simplifies conventional, external optical trapping setups by reducing the dependence on bulky objective lenses and mechanical alignment apparatuses. Complexity, cost, and optical power yields are often factors which limit the extent of optofluidic integration. This work incorporates the use of standard inexpensive high power fiber-connected telecom laser diodes integrated directly into a custom fabricated PDMS microfluidic chip.

1.3 Research Objectives

The approach of this work is to demonstrate new functionality in the field of optical trapping within an integrated optofluidic chip. Selectively altering the optical, fluid, and geometrical characteristics in this environment is of interest from a physical perspective and shows potential for enhancing on-chip capabilities.

The oscillating behaviour of self-formed multi-particle arrays have been observed experimentally in the past [12], however a theory which fully explains the occurrence of dynamic motion and inhomogeneous spacing has not been well established. The dynamics and spacing attributes of particle arrays formed within this integrated system are characterized experimentally and theoretically verified through collaborative work with Dr. Kawano in the development of an opto-hydrodynamic theory.

1.4 Contributions

The flow-dependent novelty of this work arose predominantly from an experimental standpoint and is explained qualitatively, whereas the chapter dealing with particle arrays was experimentally and theoretically verified. Actively biasing fibers with respect to microfluidic flow showed cyclic particle behaviour with applications toward specimen reorientation and localized mixing. Discrete particle waveguiding was observed in systems where light opposed flow and indicates a system of optofluidic waveguiding

which is entirely distinct from established methods. Control over particle position was demonstrated as a function of output power and opposing flow velocity in setups containing a lensed optical fiber and the application of a simple flow-rate meter was demonstrated. Other flow-dependent novelties include size trimming of particle assemblies and the demonstration of large-scale particle swarms. The majority of the flow-dependent work was recently published in a popular journal for on-chip diagnosis, *Lab on a Chip* [13] and presented orally at *CLEO* 2007, *APS* 2007, and *CLEO* 2008.

The work on particle arrays presented notable coherence between experimental and theoretical work and is the first such demonstration to fully explain the onset of spontaneous particle oscillation. The majority of this work was also recently published in the distinguished journals, *Physical Review B* [14] and *Optics Express* [15]. Conference publications included *OMEMS* 2007 and *CLEO* 2008.

1.5 Thesis Outline

This thesis is organized into 8 chapters. Chapter 2 provides the theoretical basis for single and dual-beam optical trapping and discusses the effects of particle size on incident wavelength. The influence of the microfluidic environment, specifically drag, on trapping is also discussed. Chapter 3 provides an overview of past trapping work with an emphasis on integrated optics. Chapter 4 offers an in depth account of the techniques employed for custom fabrication of microfluidic chips with integrated optical fibers, while Chapters 5 explores flow-dependent effects of optical trapping. Chapter 6 investigates particle array formation and oscillation dynamics while Chapter 7 concludes these findings and offers a prospectus for advancement. Chapter 8, titled *Avenues for Exploration*, characterizes recent discoveries, including power- and polarization-induced particle oscillation, continuous particle circulation, active storage, and a 3-dimenstional particle assembly rotator. The influence of optical heating on trapped particles is considered in §8.2 and, in §8.3, trapping within immiscible systems was found to enable massive tornado-like circulatory behaviour. Finally, §8.4 presents the experimental results for a self-trapped stream of Rayleigh particles in solution, the theory of which was published elsewhere in *Physical Review A* [16] and *CLEO Pacific Rim* 2007.

CHAPTER 2

OPTICAL TRAPPING & MICROFLUIDICS THEORY

In this chapter, the fundamental concepts involved in optical trapping of micron-sized transparent spheres are introduced. Theory is presented for optical and drag force determination and a force dependence on particle size and wavelength is discussed. Lastly, microfluidic effects on trapping phenomena are considered.

2.1 TRAPPING PRINCIPLES

Whenever a flow of energy exists, such as in an electromagnetic wave, the wave itself carries momentum. Light waves, being electromagnetic waves, contain linear and angular momentum and can exert forces and torques on matter. The radiation pressure exerted by laser light has been used to trap and manipulate micro-particles since the pioneering work of Arthur Ashkin [5] in 1970. From a quantum perspective, light is made up of numerous photons with energy, $E=hc/\lambda$, and momentum, $p=E/c=h/\lambda$, where h is Planck's constant (6.626×10^{-34} J·s), c is the speed of light, and λ is the incident wavelength. Typical quantities for light at 980 nm are 2.03×10^{-19} J and 6.76×10^{-28} kg·m/s for the photon and linear momentum magnitudes, respectively. From Newton's second law, the time rate of momentum change for a particle is equal to the resultant force acting on the particle, $F=dp/dt$, and is in the direction of the force, where dp/dt is the result of light imparting momentum to the particle in accordance with the conservation of momentum (the total momentum in the light-particle system before and after a collision is conserved). Since momentum is also a vector, any change in electric field orientation, *i.e.* polarization, will produce a torque and change the orientation of a trapped particle and is a consequence of angular momentum [17-20].

Using the relation for photon energy and Newton's second law, the force imparted to a sphere in a medium with refractive index, n_m, can be written in the form [21],

$$F_s = \frac{I_o n_m C_{pr}}{c}, \tag{2.1}$$

where F_s is the scattering force, $I_o = 2P/\pi w_o^2$ is the incident beam intensity at the sphere location, P and w_o are the beams output power and mode field radius at the sphere location, respectively, C_{pr} is the sphere's radiation pressure cross-section, and c is the speed of light in vacuum. The sphere's radiation pressure cross-section for non-absorbing particles, such as the case with polystyrene spheres, is proportional to the momentum removed from the original beam and not reradiated by the sphere, that is, not forward scattered or absorbed. The radiation pressure cross-section is then proportional to the momentum transferred to a scattered particle, however is generally a function of the state of incident polarization and particle orientation for non-spherical particles [21]. The radiation pressure cross-section, C_{pr}, is related to the sphere's size, geometry, and refractive index and is equal to the total momentum removed from the incident beam, C_{sc}, minus that forward scattered, $C_{sc}\overline{\cos\theta}$, or $C_{pr} = C_{sc} - C_{sc}\overline{\cos\theta}$. The mean cosine value represents scattered light from the sphere and is generally an integration of the reduced Poynting vector [22]. From this relation it is clear that larger scattered angles result in an increase in the radiation pressure cross-section, thus imparting a greater force. The calculation of C_{pr} generally requires complicated numerical techniques which are beyond the scope of this thesis [22-24].

The intensity term given in Eq. (2.1) is directly related to the time-averaged Poynting vector, however the optical force on a microsphere cannot respond to the instantaneous high frequency components of the time-varying electric field, and are considered in this work to have little effect. In terms of the electric field, the average irradiance, or intensity, of the output light is given by, $I_o = \frac{1}{2} n_m c \varepsilon_o E_o^2$, where ε_o is the absolute permittivity and E_o is the electric field amplitude. The outward, or axial, scattering force given in Eq. (2.1) can be directly controlled by varying the optical intensity and is the prominent means contributing to particle motion and trapping reported in this thesis. Force components also exists in the radial and backwards (towards the optical source)

directions which acts to pull particles in the direction of increasing optical intensity. These components are termed gradient forces and are inherent in highly diverging or converging laser beams.

Conventional optical trapping requires steep gradients of light that are produced when a single collimated laser beam is tightly focused using an objective of high numerical aperture (NA). A tightly focusing lens, for example, will have a stronger gradient pull compared to a weakly focusing lens, whereas weakly focusing, or weakly diverging lenses contain a preferential axial force. The objective is often a water-immersion objective and can be placed directly in the medium containing the samples to be trapped, or positioned above a transparent sample chamber. The trapped samples are then trapped in place near the focus of the objective lens. For optical forces to be sufficiently exerted on the specimen, thereby enabling trapping, the specimen ideally will have an index of refraction greater than the surrounding medium. Biological macromolecules, which consist largely of water, are usually insufficiently refractile to be trapped alone [25] and require high refractive index particles to be attached as a handle. It is also necessary for trapped bodies to transmit a portion of the incident light, that is, they must contain a level of transparency at the wavelength and length scales in question in order to avoid heating and radiometric forces.

2.1.1 Geometrical Optics Regime ($r >> \lambda$)

When a ray of light strikes a sphere, a fraction of the incident momentum is either reflected at the surface, or retransmitted through the sphere. The fraction of light reflected and refracted (transmitted) at the surface can be interpreted from Fresnel's equations and is a function of the incident polarization, incident angle (for a spheres, a finite range of continuous angle distributions exist), and refractive index contrast between the sphere and surrounding medium. Incident ray angles are determined by their orientation and position relative to the sphere's surface and refracted angles follow directly from Snell's law. Numerical techniques are generally required to sum the contribution of all entrance, exit, and internally reflected rays. Forces are generated by light's momentum change at points of refraction and reflection, the efficiency of which is

termed the scattering efficiency, Q. With the ray optics model, the scattering force exerted on a particle is given by [26],

$$F_s = Q_s \frac{n_m P_i}{c}, \tag{2.2}$$

where Q_s is a dimensionless number known as the axial scattering efficiency, n_m is the refractive index of the medium, P_i is the optical power incident to the sphere, and c is the speed of light in vacuum. The quantity $n_m P_i/c$ is the incident momentum per second of a ray with power P_i in medium n_m and Q can be thought of as the fraction of momentum transferred to the sphere. For perfectly reflecting particles $Q = 2$; for perfectly absorbing particles, $Q = 1$, and for non-absorbing transparent particles, $Q < 1$, typically between 0.05 and 0.5. Similarly, a separate scattering efficiency, Q_g, exists for the gradient force, F_g, and expressions for Q_s and Q_g are [26],

$$Q_s(\theta_i) = 1 + r\cos(2\theta_i) - \frac{t^2\left[\cos(2\theta_i - 2\theta_r) + r\cos(2\theta_i)\right]}{1 + r^2 + 2r\cos(2\theta_r)}, \tag{2.3}$$

$$Q_g(\theta_i) = r\sin(2\theta_i) - \frac{t^2\left[\sin(2\theta_i - 2\theta_r) + r\sin(2\theta_i)\right]}{1 + r^2 + 2r\cos(2\theta_r)}, \tag{2.4}$$

where θ_i is a ray angle incident to the sphere surface, θ_r is the refracted angle defined by Snell's Law, $n_1 \cdot \sin(\theta_1) = n_2 \cdot \sin(\theta_2)$, and t and r are the Fresnel transmission and reflection coefficients, respectively. For transverse electric (TE) waves, for example, the Fresnel transmission and reflection coefficients are, respectively [27],

$$t = \frac{2\cos(\theta_i)}{\cos(\theta_i) + \left[\left(\frac{n_p}{n_m}\right)^2 - \sin^2(\theta_i)\right]^{1/2}}, \tag{2.5}$$

$$r = \frac{\cos(\theta_i) - \left[\left(\frac{n_p}{n_m}\right)^2 - \sin^2(\theta_i)\right]^{1/2}}{\cos(\theta_i) + \left[\left(\frac{n_p}{n_m}\right)^2 - \sin^2(\theta_i)\right]^{1/2}}, \tag{2.6}$$

where n_p is the refractive index of the sphere.

Figure 1(a) shows a simplified ray optics model used to explain the origin of gradient and scattering forces from transmitted rays where the particle size is assumed to be much larger than the incident wavelength. A sphere with refractive index, n_p, is initially located off-axis in the path of a Gaussian beam. The light ray nearest to the optical axis carries momentum, $P_{A,i}$ which is proportional to its intensity at this location. Further from the beam axis, another light ray carries momentum $P_{B,i}$ and is smaller than $P_{A,i}$ due to the Gaussian nature of the beam (intensity decreases radially as in a bell curve distribution). Both rays strike the surface of the sphere and pass through with a direction change in accordance with Snell's law and a magnitude change determined by the reflection and transmission coefficients. Angles of incidence and the effective refractive index generally determine the fraction of light that is reflected and transmitted, however for simplicity, it is assumed that the entire ray passes through the sphere. The rays then impact the inner surface of the sphere, where again a portion will reflect back into the sphere and the remainder will refract out of the sphere. Depending on positioning within the sphere, the ray may undergo several cycles of internal reflection before exiting. The momentum of the exited rays are shown as $P_{A,f}$ and $P_{B,f}$. Subtracting the exit vectors from the entrance vectors for Ray A results in momentum change, $-\Delta P_A$, the resultant of which is shown in Figure 1. Similarly, the resultant change in momentum for Ray B, $-\Delta P_B$, is shown. The total change in momentum for the two-ray system is $-(\Delta P_A + \Delta P_B)$ and corresponds to a change in light momentum, $-\Delta P_{light}$. From momentum conservation, $-\Delta P_{light} = \Delta P_{sphere} = F_{sphere}$, where F_{sphere} is the force imparted to the sphere. This force can be resolved into two orthogonal components, the gradient force, $F_g(\hat{x})$, which pulls the particle in the direction of increasing optical intensity, *i.e.* in the radial direction, and the scattering force, $F_s(+\hat{z})$, which acts to funnel the particle down the optical axis. This result shows a simplified case containing two rays and in practice, the procedure is extended to include the summation of a finite series of reflected and refracted rays while taking into account the characteristics of the system.

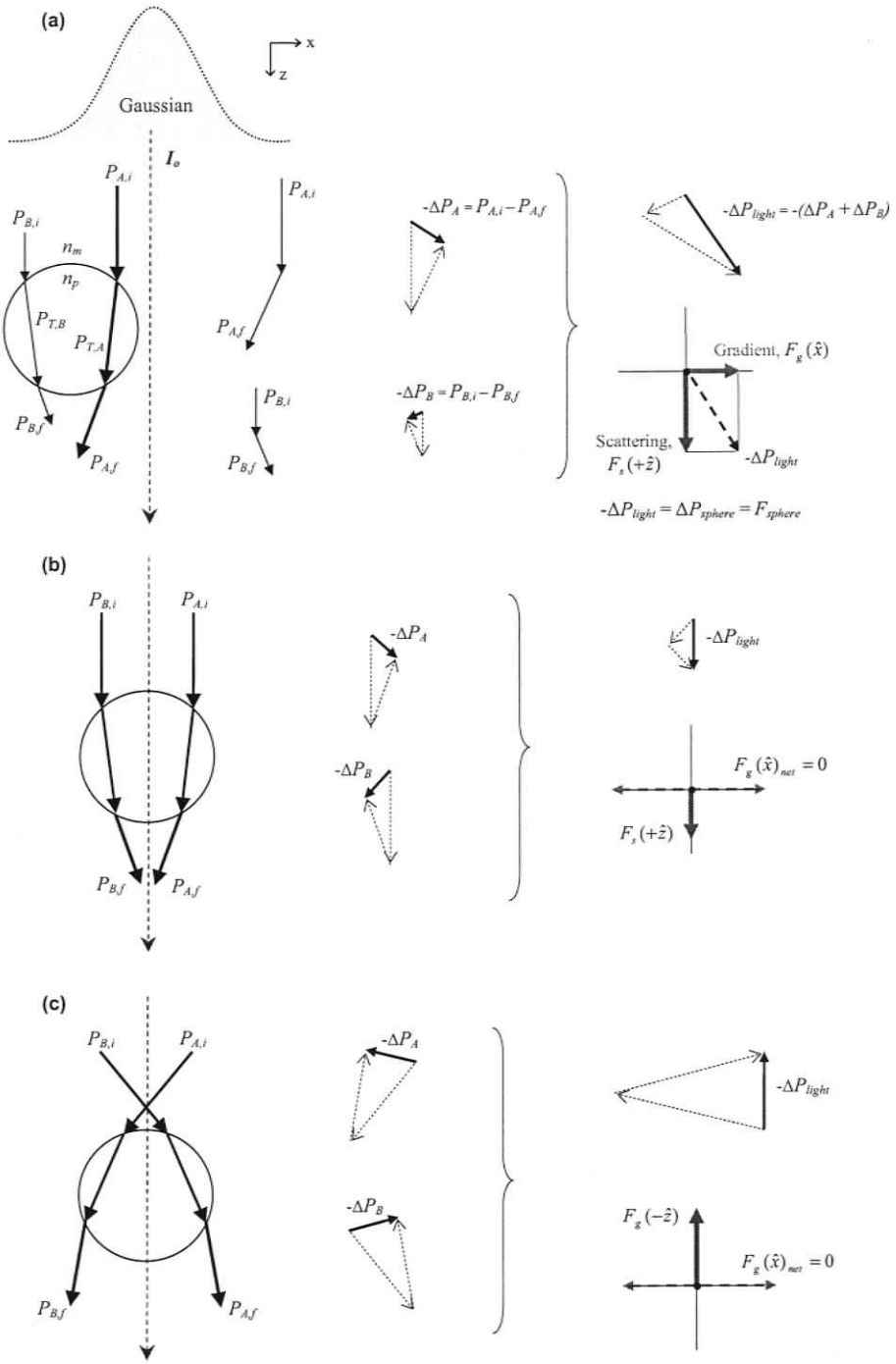

Figure 1 Simple ray optics model used to describe the origin of gradient and scattering forces in a Gaussian beam. (a) Sphere positioned off-axis in a collimated beam. (b) Sphere positioned on-axis in a collimated beam. (c) Sphere positioned on-axis in a tightly focused beam.

Figure 1(b) shows a particle positioned on-axis of the same collimated beam depicted in Figure 1(a), however due to particle and beam symmetry, the net gradient force in the x-direction is zero. If an external force acts to displace the particle from the beam axis, the net gradient force will no longer be zero and an optical restoring force acts to pull the particle back onto the optical-axis. For a particle to stably trap with a single beam, tight focusing is used to create a large backwards gradient force in the –z-direction, thereby exceeding the scattering force in the +z-direction. Figure 1(c) shows two symmetric rays incident on a sphere resulting in the axial gradient force, $F_g(-\hat{z})$. With this geometry, scattering forces due to refraction are minimal, however axial gradient forces still must exceed scattering forces from surface reflection for stable trapping to occur (see Figure 2(b)). Single-beam trapping is traditionally accomplished by tightly focusing light onto a specimen with a microscope objective or a highly tapered optical fiber [28], creating rays which impact the sphere at angles large relative to the normal. The larger the incident angle, the higher the gradient force, reaching a maximum at ~70° [26]. Similarly, when the incident light is primarily normal to the surface as in Figure 1(b), the scattering force is the dominant force and propels the particle down the beam axis.

Alternately, a particle can be trapped between two collinear beams, where the scattering force from one beam balances the scattering force from the other, and radial gradient forces, being small, act to further increase the stability of the trap. In this configuration, a sphere will trap at mid-distance between beams assuming identical beam conditions. Divergent counter propagating beams emitted from optical fibers are used extensively in the present work, where scattering forces are the dominant forces.

Figure 2(a) shows a sphere located on the axis of a weakly diverging Gaussian beam. Two rays are drawn symmetric to the beam axis and impact the sphere surface at a distance of 0.7 times the sphere radius. For only two rays drawn with this orientation, it is clear that the resultant force is predominantly the axial scattering force. If the incident beam is now resolved into a distribution of 4 plane waves, taking rays at surface distances $0.15 \cdot r_o$ and $0.70 \cdot r_o$, we see in Figure 2(b) that axial gradient and scattering forces occur simultaneously, whereby the scattering force from a moderately diverging beam is the dominant force. Similarly, if surface reflection is included in the analysis, as in Figure 2(c), it is further evident that scattering forces dominate the effect of axial gradient forces

with the given beam geometry.

For an order of magnitude approximation of the three force components, $F_s(+\hat{z})$, $F_g(-\hat{z})$, and $F_g(\hat{x})$, Eq. (2.2) can be solved by integrating over a finite distribution of incident angles for the upper left quadrant of the sphere. For sphere sizes less than the beam waist size, a cross-sectional area proportionality factor $(r_o/w_o)^2$ is added to Eq. (2.2), where r_o is there sphere radius and w_o is the Gaussian beam waist radius. Eq. (2.2) is then rewritten as,

$$F = \frac{n_m P}{c}\left(\frac{r_o}{w_o}\right)^2 Q, \tag{2.7}$$

where [29],

$$Q = \int_{\theta_1}^{\theta_2} Q(\theta_i)\cdot \sin(2\theta_i)\cdot e^{-2(r_o/w_o)^2 \sin^2(\theta_i)}\cdot d\theta_i\,. \tag{2.8}$$

For a divergent beam with plane waves incident at 10° with respect to the optical axis, the angular distribution across the sphere with respect to the normal is from 10° ($=\theta_1$) to 80° ($=\theta_2$). Typical parameters employed experimentally were r_o = 1 μm, w_o = 4.93 μm, and $Q(\theta_i)$ follows directly from Eq. (2.3) & (2.4) for scattering, Q_s, and gradient, Q_g, trapping efficiencies, respectively. Carrying out the integration using Maple (Maplesoft, Waterloo, ON), it is found that Q_s = 0.443 and Q_g = 0.133. Eq. (2.7) can then be solved and resolved into orthogonal radial and axial components. The axial scattering force comprising the upper spherical hemisphere (2 quadrants) is then [26], $F_s(+\hat{z}) = 2F_s\cos(\varphi)$ = 4.7 pN, where φ is the divergent beam angle with respect to the beam axis, in this case 10°. The axial gradient force is [26], $F_g(-\hat{z}) = 2F_g\sin(\varphi)$ = 0.25 pN, and the radial gradient force, $F_g(\hat{x}) = F_g\cos(\varphi)$ = 0.97 pN. From this approximation, it is evident that the axial scattering force is greater than the axial gradient force by a factor of 19. Similarly, when the beam divergence is decreased to 3.5°, as is the case with a straight cleaved optical fiber, $F_s(+\hat{z})/F_g(-\hat{z})$ increases to 21, and the radial gradient force decreases by 25%. It can also be shown that for a highly convergent beam as in Figure 1(c), the axial gradient force dominates the axial scattering force, thereby enabling single beam traps. For two-beam traps, the radial gradient force is expected to double.

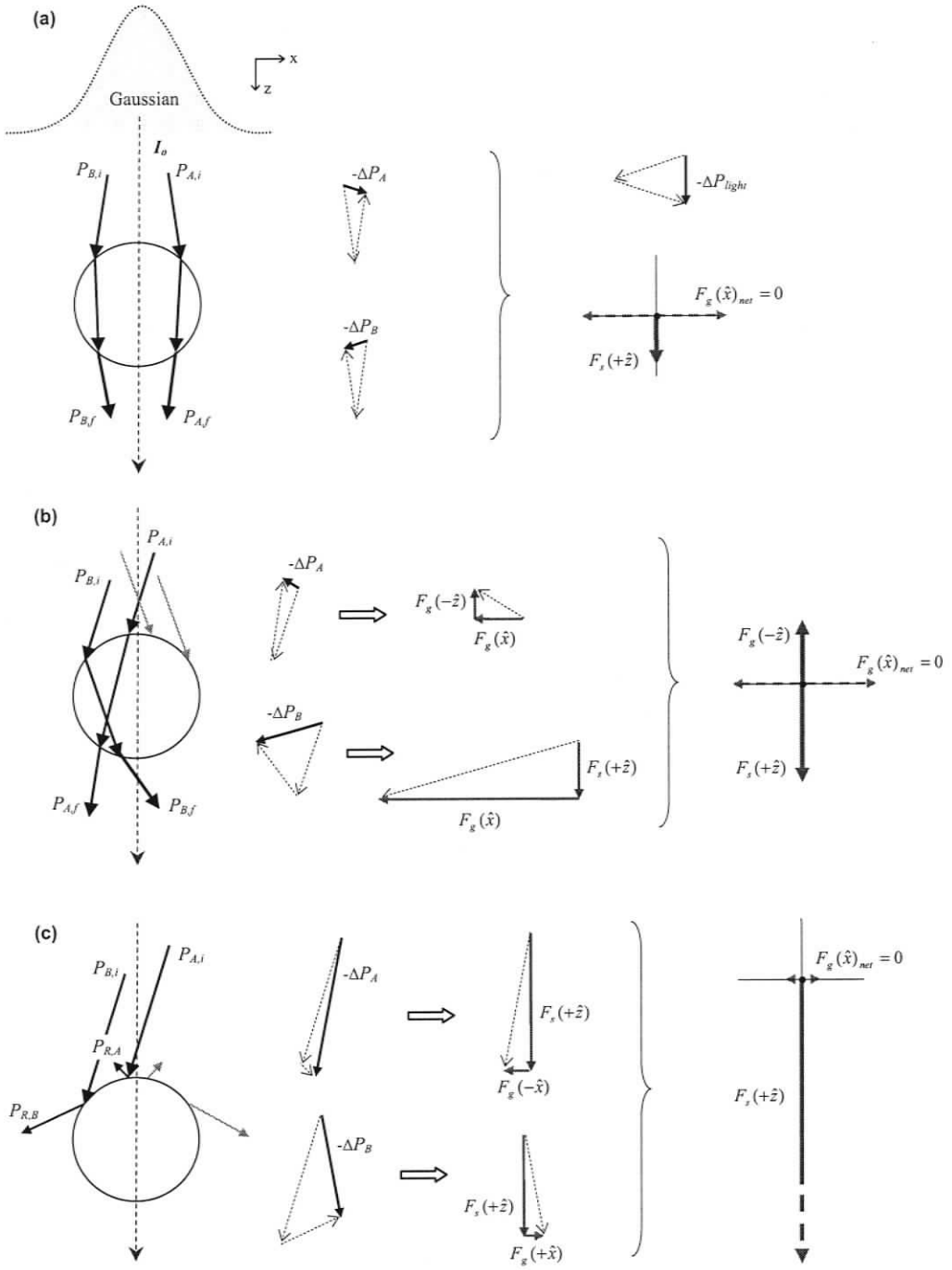

Figure 2 Ray optics model for a diverging beam. (a) Two rays of a weakly diverging beam drawn at $0.70 \cdot r_o$. (b) Rays drawn at $0.15 \cdot r_o$ and $0.70 \cdot r_o$, where the inner ray gives rise to a gradient force in the -z-direction and the outer ray gives rise to a scattering force in the +z-direction. (c) Rays reflected from the sphere surface resulting in large scattering forces.

2.1.2 Rayleigh Regime ($r << \lambda$)

A dipole model is generally considered when the particle radius is less than ~ $\lambda/20$ [30]. When light is incident on a Rayleigh-sized particle, an electric dipole is induced across the particle, scattering light equally in both the forward and backward directions. Within this regime, C_{pr} in Eq. (2.1) equates to C_{sc} [30] and an analytic solutions exists for the scattering force as [3],

$$F_s = \frac{128\pi^5 n_m r_o^6 I_o}{3\lambda^4 c}\left(\frac{(n_p/n_m)^2-1}{(n_p/n_m)^2+2}\right)^2, \tag{2.9}$$

where r_o is the sphere radius, λ is the wavelength of incident light, and n_p and n_m are the refractive indices of the particle and host medium, respectively. Similarly, a Rayleigh particle also experiences a gradient force in the direction of increasing intensity and is expressed as [3],

$$F_g = \frac{2\pi r_o^3}{c}\left(\frac{(n_p/n_m)^2-1}{(n_p/n_m)^2+2}\right)\nabla I_o. \tag{2.10}$$

The gradient force arises from the interaction of the induced dipole with the beam's electric field inhomogeneities (gradients) and is proportional to the dispersive real part of the sphere's complex polarizability [31]. The scattering force is due to momentum transfer from the incident field and is proportional to the dissipative imaginary part of the complex polarizability [31]. Generally, both these force components are a consequence of cycles of absorption and reradiation of light by the induced dipole. For Rayleigh particles, random thermal motion, or Brownian diffusion, becomes an important factor in optical trapping stability. For particles to stably trap between two beams or in a single-beam gradient force trap, the thermal energy associated with Brownian motion must be smaller than the optical potential of the trap. The stability criterion is given by the Boltzmann factor [32] and can be simplified as [30],

$$\frac{2\pi n_m r_o^3}{c}\left(\frac{(n_p/n_m)^2-1}{(n_p/n_m)^2+2}\right)\frac{2P}{\pi w_o^2} \geq 10 k_B T, \tag{2.11}$$

where k_B is the Boltzmann constant (1.38×10^{-23} J/K) and T is the medium temperature in Kelvin. The term on the left represents the optical potential of the trap, while the term on the right represents kinetic energy due to Brownian motion. For the conditions of the present work, with n_m=1.33, n_p=1.574, P=100 mW, w_o=4.5 μm at the particle location, and T=293 K (room temperature), the minimum particle size to stably trap is 160 nm.

2.1.3 Intermediate Regime ($r \sim \lambda$)

The majority of particles trapped fall within an intermediate regime, $0.1\lambda < r < 10\lambda$. At these particle sizes, the Rayleigh approximation fails due to the increased significance of wave optical effects and microscopic interaction of light and matter. The optical ray theory also fails as light no longer scatters anisotropically in the predominantly (forward) axial direction and backscattered lobes become more pronounced. A portion of the results presented in this thesis are simulated with the collaborate efforts of Dr. Kawano and used a Maxwell's stress tensor (MST) [33] with generalized multipole technique (GMT) [34]. With this approach, the net force exerted on an arbitrary object is determined by the Maxwell stress tensor, which is a relation conforming to the conservation law of electromagnetic energy and linear momentum. The fields inside and out of the sphere were determined using GMT, where the boundary conditions at the surface must be continuous. Variations to the MST approach also exist [35-37], while other approaches have been based on, for example, a discrete dipole approximation (DDA) [38], a Matrix-T method [39], a Finite-Difference-Time-Domain (FDTD) technique [40, 41], generalized Lorenz-Mie theory (GLMT) [23, 42, 43], and a coupled dipole method (CDM) [44, 45].

2.2 Microfluidic Phenomena

Mass transport in a microfluidic environment differs greatly compared to its macroscopic counterpart. Micro-scale flows are predominantly laminar (flowing in perfectly parallel layers) and free of turbulence due to viscous forces strongly dominating the effects of inertia [6]. Laminar flows prevail in microfluidic devices due to a dramatic reduction in length scales and an increase in the associated surface area to volume ratio. Consider, for

example, a 1 μm diameter bead in a water-filled 250 μm × 250 μm microchannel of arbitrary length. When water in the channel is pumped from an external source at flow rate, Q, the bead will transition at the rate of the water due to viscous drag and not any slower. When fluid flow is shut off, the bead stops instantly as if the bead is bound to the region of fluid surrounding it. In other words, past forces exerted on the particle have no impact to its present state and drifting due to momentum is non-existent. A similar situation exists with optical forces, particularly, when laser light is turned off, bead motion stops instantly. Particle dynamics in a microfluidic system are, therefore, determined only by instantaneous forces.

The Reynolds number is a dimensionless numbers which relates inertial to viscous forces and is often used as an indicator to predict when turbulent flow will. The Reynolds number is given by,

$$\mathrm{Re} = \frac{LU}{\nu}, \tag{2.12}$$

where L is the characteristic length scale (*i.e.*, the channel width), U is the average velocity in the channel, and ν is the kinematic viscosity of the fluid. The kinematic viscosity is related to the shear, or dynamic viscosity by $\nu = \eta/\rho$, where η is the dynamic viscosity and ρ is the fluid density. For scenarios depicted in this work, typical length scales are 250 μm, flow velocities do not exceed 700 μm/s, and the kinematic viscosity at 20 °C is 1 $\times 10^{-6}$ m^2/s resulting in a Reynolds number of 0.2. Reynolds numbers less than 1000 – 2000 are generally considered to be laminar [46] and the flows depicted in thesis are not expected to contain turbulent components. Particle motion in the surrounding fluid is completely dominated by viscous drag.

For a spherical particle in a medium with negligible inertial forces, the drag force exerted on a particle may be quantified from Stokes' drag force on a sphere as,

$$F_d = 6\pi\eta r_o u, \tag{2.13}$$

where η is the room temperature dynamic viscosity of the medium (1 $\times 10^{-3}$ Pa·s at 20 °C for water), r_o is the sphere radius, and u is the planar velocity of the medium. The Stokes' drag force approximation shown here is used extensively in this work and is considered valid for microfluidic systems where viscous effects dominate inertia. Viscous drag is

also a vector and the direction of the imparted force can be determined by the direction of the constituent flow velocity.

2.2.1 Optical-drag Force Balance

The optical-drag force balance in conjunction with a diverging beam acting against flow can be obtained by equating Equations (2.2) and (2.13) and solving for axial displacement from the beam's focus, z. It is found that [29],

$$z = \frac{\pi w_o^{\,2}}{\lambda}\sqrt{\frac{n_m P Q r_o}{3\pi\eta c w_o^{\,2} u} - 1}, \tag{2.14}$$

where w_o is the mode-field radius at the beam's focus and P is the total output power. The incident optical power, P_i, from Eq. (2.2) may not necessarily equal the total output power, P, when the cross sectional area of a trapped sphere is smaller than the area defined by the laser mode. Eq. (2.14) takes this into account by fractionalizing the respective areas. In cases where a lensed optical fiber was employed, w_o was estimated to reside ~10 μm within the silica-medium interface for 980 nm light in water. The beam is a diverging Gaussian with an assumed TEM_{00} single-mode transverse electromagnetic intensity distribution. The mode field radius arises in Eq. (2.14) because the intensity profile due to a Gaussian varies axially as [47],

$$w(z) = w_o\sqrt{1 + \frac{z^2\lambda^2}{\pi^2 w_o^{\,2}}}. \tag{2.15}$$

Similarly, the on axis beam intensity decreases non-linearly with increasing distance from the focus as [47],

$$I(z) = \frac{I_o \pi^2 w_o^{\,4}}{\pi^2 w_o^{\,4} + \lambda^2 z^2}. \tag{2.16}$$

2.3 SUMMARY

In this chapter, the theory behind optical trapping in a microfluidic environment was established and different regimes of trapping were discussed. A summary of the four prominent forces exerted on a particle residing in a microfluidic channel are given in Table 1.

Table 1 Contributing force components used in trapping experiments.

Force	Handle	Symbol	Diagram
Scattering	Optical Intensity	$F_s(+\hat{z})$	
Gradient (axial)	Beam Shape (Lensed vs. Cleaved Fiber)	$F_g(-\hat{z})$	
Gradient (radial)	Beam Shape (Lensed vs. Cleaved Fiber)	$F_g(\pm\hat{x})$	
Drag	Flow Rate	F_d	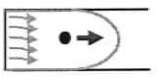

The scattering force, $F_s(+\hat{z})$, acts in the direction of beam propagation and naturally decreases axially for a divergent beam. Scattering forces can be increased by tuning the optical intensity via injection current to a laser diode. The axial gradient force, $F_g(-\hat{z})$, acts in a direction opposite to the scattering force and is negligible for the weakly and moderately diverging beams employed in this work. The radial gradient force, $F_g(\hat{x})$, acts radially in the direction of increasing optical intensity and, in the context of this thesis, can be increased by using a widely divergent lensed optical fiber as opposed to a straight cleaved fiber. Lastly, the drag force on a particle can be manipulated by varying the flow rate and direction of the impacting fluid.

CHAPTER 3

LITERATURE REVIEW

In this chapter, an overview of past work related to the integration of optics and microfluidics is provided. Particular attention is given to fiber-integrated systems, traps used in uni-beam optical chromatography, and demonstrations involving optically bound matter in a dual-beam trap.

3.1 INTEGRATED TRAPPING

Many lab-on-chip technologies rely on external optics for characterization and operation. An important capability of optics is provided by optical scattering and gradient forces, which allow for precise noninvasive means for trapping (or tweezing). Optical trapping has been used to transport [48, 49] and manipulate cells [50, 51] unravel DNA [52], manipulate droplets [53] and sort particles and micro-organisms [48, 54] without physical contact. The direct integration of optics and fluidics, or optofluidics, is an emerging area with potential to extend lab-on-chip functionalities [9, 10]. Planar integration of optical elements and microfluidics is particularly attractive from a lab-on-chip application perspective [55]. It also allows for a flexible compact framework in that bulky external optics operating in the third dimension are not required.

Conventional optical trapping utilizes external optics [32] where intensely focused laser light from a microscope objective converges onto the object to be trapped, thus imparting light momentum and moving the object to the beam's focus. To miniaturize optical hardware, optical components such as liquid waveguides, lenses, prisms and beamsplitters [56-58] can be formed in-place directly out of the manufacturing polymer, typically a silicone-based elastomer. Optical delivery can be miniaturized by implementing optical fibers [59], etched tapered fibers [28], VCSEL arrays [60] and more

recently a semiconductor substrate for both the laser and integrated microfluidic trapping channel [61]. This latter method offers novel advancements towards on-chip light source integration and precise optical alignment, but is currently restricted due to beam divergence, low output power, and cost. Alternately, for applications where inexpensive integrated high optical power is required, fiber integration inside polydimethylsiloxane (PDMS) [62-64] has been employed. These works use raised SU-8 photoresist structures as the fiber aligning mechanism and an overcoat of PDMS as the seal, and more recent work [65, 66] demonstrated an all PDMS method for optical fiber pre-alignment and integration.

Recently, embedded optical fibers in microfluidic systems have shown promise in extending the capabilities of cell analysis techniques. An optical stretcher method has been developed for cancerous detection of mouse fibroblasts and epithelial cells through surface-induced optical cell deformity testing [67]. Dual-beam fiber traps have been deployed in Raman spectroscopy measurements for determining the chemical composition of primary human keratinocyte cells [68]. Additionally, embedded fiber integration has shown promise in fluorescence detection of DNA-based bacteria samples [69] and particle counting and velocity measurements through the feedback of scattered light [70].

With respect to the combination of flow and optical trapping, stable particle trapping has been demonstrated in flowing microfluidic environments where optical trapping forces dominate the influence of drag [71, 72]. An elegant optofluidic trapping strategy was recently presented where the evanescent field surrounding integrated solid core waveguides effectively trapped and transported particles along the guides [49]. With this strategy, optically-powered upstream, downstream and cross-stream particle transport was demonstrated. Directly opposing optical and fluidic forces have been used for various applications under the name optical chromatography (OC). This method has been employed to separate polystyrene particles and erythrocyte cells based on size [29], determine antigen-antibody reaction rates and concentrations through OC separation [73], empirically measure a microorganism's motional force [74], measure trapped particle size [75], estimate erythrocyte cell elasticity [76], and separate particles based on refractive index [77, 78]. Compared with conventional optical tweezing, trapping stability in these

configurations is limited by flow irregularities (*i.e.* imperfect device sealing or flow which may not be entirely antiparallel to the beam axis) and a minimally divergent beam (small radial force component).

3.2 Optical Binding

The control of light by matter [79], and of matter by light [5], is combined in the field of "optical interaction." Interesting physics arises within this regime ($r \sim \lambda$), such as the self-organization of dielectric particles, for example polystyrene microspheres, into arrays analogous to atomic systems [80]. A simplistic method to trap micrometer-sized dielectric particles is performed using counter-propagating divergent beams from optical fibers, which enables trapping of single particles [59] and self-organized multi-particle arrays [81]. The self-organized multi-particle trap offers an intriguing system for studying optical interactions between particles, with applications towards contract-free storage of biological cells [81] and ion traps for quantum computing [82]. Recently, there has been much interest in understanding the underlying physics behind optical binding in multi-particle arrays [12, 37, 44, 45, 81, 83-85]. For two particles, the dual-beam optical trap has shown bistability and hysteresis [83] and inter-particle restoring forces have been mapped out through normal mode correlations [86]. Forces have been calculated for two particle systems [44, 45, 83, 85-87] and dynamic interactions have been added for two particles, however, only for two spatial dimensions and without hydrodynamic interactions [37]. McGloin *et al.* demonstrated a nonlinear decrease in particle spacing as beam separation is increased and showed numerically that spacing for a three-particle array is smaller than that for two-particle array [85]. Equilibrium positions in a two-particle array with coherent sources also show sensitivity to refractive index contrast and standing wave effects [44], whereby several equilibrium positions can exist for two particles. Conveyor belt motion of particles has been demonstrated for coherent beams where the phase of one beam was altered, thus inducing particle repositioning [88]. In addition, extensions of optical binding to micron-sized oil droplets in air have been established [89].

For more particles, equilibrium positions for up to 7 trapped particles in an array have been demonstrated [12] as well as a strong dependency of equilibrium spacing on particle size [81]. Although several studies have contributed to understanding the behaviour of trapped particles in a dual-beam system, further investigations are still necessary, to explain the phenomena associated with large number multi-particle arrays [37, 87]. Currently, no theory has explained fully the occurrence of inhomogeneous particle spacing, both for a particle number dependency and a dependence on inter-array particle positions (*i.e.* inner and outer inter-particle spacings differ for a fixed number particle array).

The self-formation of linear arrays with spontaneous oscillation has been observed [90], and particle escape was described in terms of diffusion [12]. The origins of the spontaneous oscillation, however, were not described. Unlike dynamical theories for ion traps [91], there is effectively no inertia for micron-sized particles in water, which makes the opto-hydrodynamic system fundamentally different.

3.3 Summary

Previous work on the planar integration of optics and microfluidics was introduced in this chapter. Trapping configurations involving optical chromatography, where a single beam opposes flow, were also discussed in terms of particle separation by size and refractive index difference and extensions to biological applications were presented. Past work on optically bound particle arrays for a dual-beam system was also introduced and the occurrence of array oscillation has been observed.

In the present work, particular attention is given to a regime of trapping where the particle size is approximately equal to the trapping wavelength. In Chapter 5, same-sized particles were observed to form regularly spaced numerous particle arrays upstream in the single fiber configuration. Biasing the beam paths in two- and three- fiber configurations showed selectivity for particle circulations. Inter-particle spacing and array oscillation are characterized and verified with computational methods in Chapter 6. The following chapter will provide a detailed account of the optofluidic chip fabrication process and provide the methodology for experimental measurement and data acquisition.

CHAPTER 4

EXPERIMENTAL TECHNIQUES

In this chapter, a detailed account of the experimental setup, optofluidic chip fabrication technique, and methods of data acquisition will be discussed.

4.1 OPTOFLUIDIC CHIP FABRICATION

Quick and inexpensive fabrication of microfluidic channels is beneficial for research-based biochemistry and chemical analysis applications. Micrometer scale channels are often preferred over their macro counterparts due to their potential as inexpensive and disposable consumer grade lab-on-chip devices. Miniaturization requires less material and reactants for synthesis and allows for parallel processing with decreased analysis time. Poly(dimethylsiloxane), or PDMS, is a commonly adopted elastomer used in micro-channel fabrication and is the material employed in this work for optofluidic chip fabrication. PDMS is less expensive than glass or silicon, is less brittle, is easy to seal, and can be readily mass fabricated. PDMS can also be made either hydrophilic or hydrophobic, depending on initial post-fabrication treatment and can seal either reversibly or irreversibly. Clean rooms are not required for fabrication, nor are expensive electron beam mask writers.

The microfluidic chips were fabricated using established soft-lithography techniques [92, 93]. A photomask was first created using AutoCAD (Autodesk, San Rafael, CA) and printed locally (Island Graphics, Victoria, BC) on a transparency using a high-resolution printer (5000 dpi – approximately 5 μm resolution). The photomask included both microchannels as well as vias for optical fiber insertion. The widths of the vias and microchannels were set through the drafting process and were typically between 250 μm and 300 μm. Upscaled versions of typical photomasks are shown in Figure 3, where the

chip centre represents the intersection of two fiber vias (horizontal) and a fluidic microchannel (vertical).

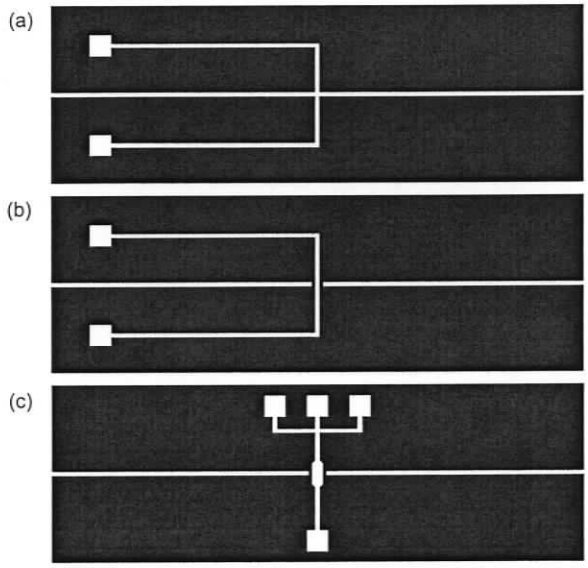

Figure 3 Typical photomasks used in dual-fiber trapping experiments. White areas represent the transparent region of the photomask. The squares are reservoir locations for fluid input and output, and the intersection is where the two optical fiber vias (horizontal) contact the fluid channel (vertical). (a) Fiber vias come in direct contact with the fluid channel. (b) Fiber vias independently sealed from the fluid channel. (c) A multiple inlet mask used in two-phase flow experiments.

In preparation of an SU-8 master (used to cast duplicate PDMS chips), a conventional glass micro-slide is prepared by removing surface contaminants. Some of these methods included soaking the slide in methanol followed by a de-ionized water rinse, and treating the slide in a piranha etch solution, typically a 3:1 mixture of sulfuric acid, H_2SO_4, and hydrogen peroxide, H_2O_2. The piranha etch solution removes all organic residues, however caution should be used as it can become explosive for a high ratio of hydrogen peroxide. Instead of using the piranha etch, OmniCoating can be spun onto the slide at 3000 rpm for 30 seconds or the slide can be O_2 plasma treated for additional surface cleaning. The slide was then placed on a hot plate for 5 minutes at 200 °C for dehydration. It was generally found that out of the box n-type silicon wafers provided idealistic surface properties and will be considered here in place of a glass micro-slide.

An epoxy-based negative tone photoresist (Nano SU-8 100, MicroChem, Newton, MA) was applied to the wafer surface using an eyedropper or syringe. The SU-8 was applied until the thickness was sufficient to accommodate the desired vertical dimensions of the channel structure. The SU-8 coated wafer is placed into a user programmable spin coater (Cookson Electronics, SCS G3P-8) to remove excess SU-8 from the wafer surface. Specific layer thicknesses are determined by rotational speed and duration, where estimates for 250 μm thick SU-8 100 are provided by MicroChem [94]. The adopted recipe was to ramp the wafer spin cycle to 500 rpm at 100 rpm/s and dwell for 10 s (spread cycle), followed by a 1000 rpm cycle with a ramp of 300 rpm/s for 25 s (uniformity cycle). The SU-8 coated wafer was then soft baked on a hot plate to allow for evaporation and densification of the SU-8 film. A process consisting of ramped heating by means of a pre-bake at 65 °C for 30 minutes followed by a soft-bake at 95 °C for 90 minutes was adopted from MicroChem for improved coating fidelity. This step also aids in the elimination of air bubbles that may remain after spinning coating. In early trials, only SU-50 was available, which can be spun to a maximum thickness of 100 μm. After soft-baking, a second 100 μm thick layer was spun on and baked, however air bubble elimination became problematic with the second layer, discouraging further development with SU-8 50.

The wafer/SU-8 combination layer was then exposed to near ultraviolet light (350 nm - 400 nm) through the transparent regions of the photomask (Figure 3). The exposed areas of SU-8 harden, or become cross-linked, that is, molecules in SU-8 form covalent bonds due to chemical reactions initiated by UV radiation. The cross-linked sections will later form the desired structural mold for the optofluidic chip. UV exposure times depend on light intensity and film thickness and must be carefully monitored to avoid over or under exposure. Over exposure results in excessive cross-linking at the SU-8 surface, causes an undesirable T-topping effect and increased susceptibility to brittle cracking. Under exposure results in weak cross-linking at the wafer-SU-8 surface, thereby decreasing SU-8 adhesion to the wafer. For the 250 μm thick SU-8 structure, best results were obtained for an exposure time of 95 s – 105 s at 350 W (Tamarack Scientific, H-500 Short Arc Power Supply and UV bulb). When lifting the exposed wafer, it is important not to tilt it with respect to gravity as this was found to arc otherwise straight channels.

Following UV exposure, the wafer underwent a post-exposure bake to complete the molecular cross-linking process. As with the soft-bake step, baking times depend on film thickness and ramping the bake temperature is recommended. A 1 minute pre-bake at 65 °C followed by a post-exposure bake at 95 °C for 22 minutes was used. The wafer was then placed into a glass jar containing MicroChem SU-8 developer to etch non-cross linked portions of the master. Development times are approximated in the SU-8 100 specification sheet [94] and depend on film thickness, frequency of perturbation, and usage history of the developer. The average development time was found to be 23 minutes; over development should be avoided as it has the effect of weakening the bonds at the SU-8-wafer interface. Decreasing the severity of perturbation towards the end of the development stage was found to reduce the probability of undesired SU-8 structural detachment from the wafer surface. Underdeveloped sections appeared as white streaks and could be removed by immersing portions of the wafer in developer. Development was directly followed by an ethonal/water rinse and 1 hour of drying at room temperature. The result is a raised epoxy SU-8 structure on a silicon wafer as shown in Figure 4. This will serve as a master to cast in liquid PDMS. Duplicate fabrication runs containing 8 glass and silicon wafers were adopted to increase product yield.

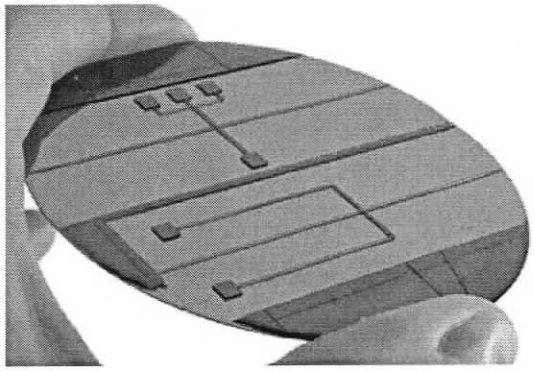

Figure 4 Silicon wafer containing a 250 μm thick raised SU-8 structure used for the molding of PDMS microfluidic chips.

At this stage in the fabrication process a liquid PDMS base known as Sylgard 184 Silcone Elastomer (Dow Corning, Midland, IL) was mixed in a 10:1 mass ratio with a curing agent inside a plastic Petri dish. Mixing was performed by hand, in a circular

fashion using a small wooden rod for at least 5 minutes. During mixing, numerous air bubbles develop and were removed by placing the mixture into a vacuum chamber (Isotemp Vacuum Oven Model 580A, Fisher Scientific, Pittsburgh, PA) for 30 minutes. Once de-gassed, the silicon master was placed into this PDMS-containing Petri dish and pressed to the bottom. For curing, the Petri dish was placed on an 80 °C hot plate for approximately 4 hours, enabling the silicon hydride groups in the curing agent to react with the vinyl groups in the base to form a cross-linked solid elastomer [95]. Curing times depend on PDMS thickness and temperature and given the current facilities, the curing temperature was limited by the melting temperature of the plastic Petri dish. Once cured, the PDMS mold was gently stripped from the SU-8 master resulting in exposed 3-dimensional microchannels in PDMS as shown in Figure 5.

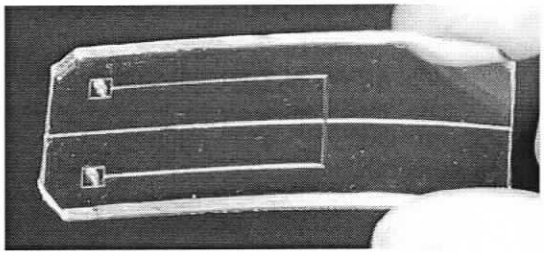

Figure 5 Flexible PDMS mold containing the hollow microchannels upon removal from the SU-8 master.

Holes (1/16" in diameter) are punched into the PDMS at the microfluidic channel facets (square reservoirs) so that press fitted nano-tubing can later be inserted. Before the chip can be used for fluid flow it must be properly sealed to a transparent rigid base. This was done by sealing the bare face of the PDMS (air exposed channels) to a pre-cleaned 1" × 3" micro-slide by plasma treatment. Both the PDMS mold and glass slide are placed face up inside a vacuum sealed plasma oven for 30 seconds, removed, and gently brought together to form a tight seal. Care must be taken when plasma bonding so that air does not become trapped between the PDMS and glass layers. The quality of the plasma gas can be determined by the glow colour inside the plasma treater; if the colour is initially purple, it can be adjusted to the desired hot pink by introducing a small amount of air into the chamber. The plasma treatment oxidizes the PDMS, creating Silanol, or Si-OH groups, thereby oxidizing the glass creating –OH containing groups [95]. When these

two faces are joined, they create –O–Si–O covalent bonds, forming an irreversible seal. Spinning a thin layer of PDMS on the glass base micro-slide (3000 rpm for 30 s) was found to improve adhesion, however this PDMS-PDMS sandwich configuration has the limitation of restricting optical heat dissipation as discussed further in §8.2. A summary of the fabrication steps leading to a final microfluidic chip are shown in Figure 6.

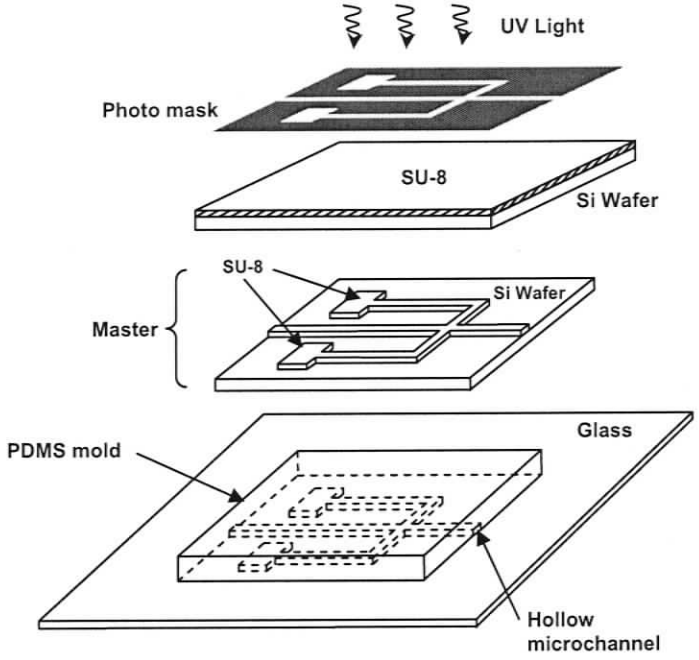

Figure 6 A photomask was first created using CAD software and printed on a transparency using a high-resolution printer. The photomask included both microchannels as well as vias for future optical fiber insertion. UV exposure through the photomask was used to pattern a 250 µm thick negative-tone SU-8 photoresist on a silicon wafer. The unexposed photoresist was developed away to leave a raised epoxy structure. Liquid PDMS was molded onto the raised channel structure, cured, removed, hole-punched, and irreversibly sealed to a PDMS-coated glass microscope slide via plasma pretreatment.

PDMS is inherently hydrophobic so plasma treatment also creates an oxide layer allowing for the surface to become temporarily hydrophilic. A hydrophilic surface permits ease in water insertion and prevents air bubble formation inside the channel, however for PDMS to maintain in a hydrophilic state, water must be introduced immediately after plasma bonding. If water does not remain in the microfluidic channels, they will eventually return to their natural hydrophobic state. Alternately, it is often

desired in experiments requiring two-phase, water-in-oil conditions to render the chip initially hydrophobic; this can be accomplished with a 2-day hot bake at 110 °C.

Figure 7(a) shows a typical assembled optofluidic chip used in these experiments. Following chip assembly, optical fibers were cleaved and inserted into the molded 250 μm × 250 μm vias. These dimensions can be reduced to 125 μm × 125 μm after the protective fiber jacket is stripped, however fibers would need to be fixed in place as fiber silica with these dimensions is highly prone to fracture. In the two-fiber configuration of Figure 7(b), fibers were inserted until they were separated by a distance of 80 - 200 μm, crossing the perpendicular microfluidic channel used for particle delivery. Pre-wetting the fiber vias with water was found to ease manual insertion of the fibers. The molding of the fiber vias ensured pre-alignment of the optical fibers and eliminated the need for an external fiber aligning mechanism.

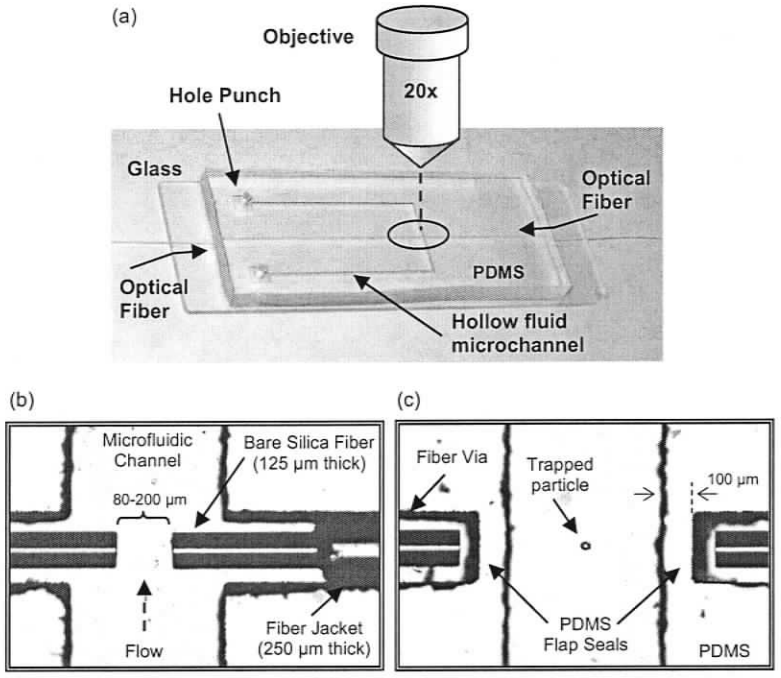

Figure 7 (a) Image of a typical optofluidic chip sealed to a standard 1" × 3" micro-slide with integrated optical fibers (horizontal) and microfluidics (vertical). Square notches on the chip surface permitted attachment of press-fitted tubing for fluid delivery. The objective was employed for imaging only. Microscope image of the embedded optical fibers in direct contact with the fluid channel (b) and sealed from the fluid channel with 100 μm thick PDMS flaps (c).

Angular fiber biasing was controlled through photomask design, whereas fiber separation could be adjusted manually post-fabrication. This method also permitted the fibers to be switched, for instance from a straight-cleaved fiber to a lensed fiber depending on the application. In early trials the photomasks were designed such that fiber vias were sealed off from the microchannels using PDMS flaps as indicated in Figure 3(c). Figure 7(c) shows a microscope image of the implemented 100 μm wide PDMS flap seals and optical fibers. Flaps of this width (100 μm) and depth (250 μm) were experimentally found to indicate an aspect ratio limit of 2.5:1 for the fabrication conditions containing SU-8 100 on silicon wafers. For higher aspect ratios, SU-8 adhesion to the wafer surface was weak and the SU-8 would often detach during the master development stage.

On a few occasions, a high aspect ratio of 4.2:1 was achieved on the wafer, however the master was not salvageable for repeat prototyping and it was necessary to manually pick SU-8 shrapnel from the PDMS mold. It was found that interface losses from the flap seals significantly reduced optical transfer to the particles and direct contact of the fiber end with the solution was the preferred implementation as it also allowed for an adjustable fluid gap between fibers. Given the planar microfabrication technique applied here, the heights of the fluid channels, ~250 μm, were determined by the outer jacket diameters (Figure 7(b)) of the standard single-mode, silica 1550 nm optical fibers employed (Corning Incorporated, Corning, NY).

4.2 Experimental Setup

The optofluidic traps used two 14-pin butterfly 980 nm wavelength fiber-pump laser diodes (LD) connectorized to standard telecom single-mode 1550 nm optical fibers (SDL-S9380, Seastar Optics). This wavelength (980 nm) is common in high power laser diodes and is ideal for minimizing biological cell damage [96]. The field intensity distribution inside the fiber is assumed to exhibit predominantly LP_{01} mode characteristics (HE_{11}), however the cut-off wavelength for single mode operation in the 1550 nm fiber is ~1450 nm, and it is therefore likely that higher order LP_{11} modes exist. A V parameter was estimated based on typical core radii, numerical aperture, and

wavelength and was found to be 3.7, indicating the existence of degenerate TE_{01}, TM_{01}, and two HE_{21} modes at 980 nm [97, 98]. If, for example, a Laguerre-Gaussian (LG) mode [99], or do-nut mode, is the primarily excited mode, the intensity profile assumes a single ring shape and a particle significantly smaller than the mode field diameter (MFD), *e.g.* a 1 μm sphere, will trap slightly off axis within the x-y plane intensity pattern (z-direction propagation). This leads to the existence of more than one equilibrium trapping position in the x-y plane with micron variance, that is, assuming the force exerted from a counter-propagating source is constant throughout the x-y plane. For particle sizes approximately equal to the MFD, little effect on trapping force [26] and position is expected for the employed non-absorbing micro-spheres. Angular momentum associated with do-nut modes have, however, been used to rotate metallic [100] and absorbing [101] spheres. Angular momentum associated with elliptically polarized light has been used to rotate birefringent particles [19] and to non-birefringent particles with a high degree of asymmetry (a consequence of anisotropic scattering) [102], however these effects are insignificant for transparent polystyrene spheres. Nonetheless, weakly guided LP_{11} modes will generally not exist exclusively from one another and the superposition of all existing modes is expected to approximate the behaviour of a Gaussian in the fluid medium.

Pin outs of the 14-pin module were determined using a multi-meter as specification sheets were not available. Laser diodes were mounted to a Thorlabs LM14S2 (Thorlabs, Newton, NJ) and an ILX LDM-4980 Series (ILX Lightwave, Bozeman, MT) mount after internal case rewiring. The mounts were interfaced to two identical ILX LDC-3724 laser diode controllers through external cabling. For the case where a Thorlabs mount was interfaced to an ILX controller, custom DB9 cabling was prepared. Figure 8(a) shows a Seastar Optics laser diode mounted in the ThorLabs LD mount with custom cabling. The laser diodes were driven at injection currents between 50 mA and 250 mA and maintained at a constant temperature of 20 °C. Optical power calibration was measured externally using a high sensitivity digital power meter and photodiode sensor (Thorlabs PM132, Newton, NJ). Figure 8(b) shows the measured P vs. I calibration results, where the fundamental linear relation, $P = 0.51(I) - 5.27\ mA$, was measured experimentally and

used to determine the output optical powers above the threshold current, I_{th}, of 17 mA. Typical optical powers used in the experiments ranged from 20 mW to 120 mW.

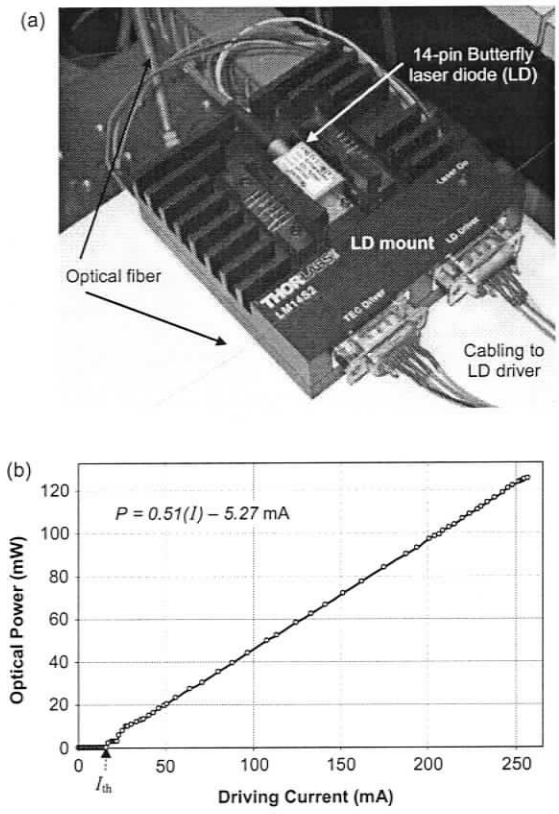

Figure 8 (a) 980 nm Seastar Optics SDL-S9380 [Model: BFSWA0980] 14-pin butterfly fiber-pump laser diode mounted in a Thorlabs LM14S2 LD mount. (b) Measured *L-I* curve for the respective laser diode.

In experiments requiring a fiber polarization controller (FPC), a 14-pin single-mode butterfly 1550 nm GaInAsP DFB-laser diode (CQF 935/808, JDS Uniphase, Milpitas, CA) was operated between 10 mW and 55 mW. In cases where a single lensed fiber was used, a 1550 nm polarization maintaining fiber (OZ Optics, Ottawa, ON), with ~2 μm spot size in air (f = 12 μm), was fusion spliced to the 980 nm pump laser diode fiber. Lensed optical fibers designed for single-mode operation at 980 nm are available commercially, however they were not employed for reasons of cost and limited stock. For setups containing two optical fibers, separate SDL-S9380 laser diodes were used and optical powers were approximately equivalent as measured by the driving current of the

laser diode controllers. In most cases, bare silica fibers were cleaved at less than 500 μm from the protective buffer (jacket) to limit the amount of exposed silica. Chipped or fractured fiber tips are usually evident upon visual inspection through a microscope, or on an IR card. When checking for damage on an IR card, the spot will appear as either non-uniform or speckled and the fiber will need re-cleaving.

The particles employed were 1 μm, 2 μm, and 9 μm diameter polystyrene microspheres (PSMs) (Bangs Laboratories, Fishers, IN) with a refractive index of 1.574 at 980 nm [103]. The variation in PSM size is ±8% and leads to deviations in scattering force estimates of ⟨±23%⟩ for 1 μm and 2 μm PSMs, and ⟨±9%⟩ for 9 μm PSMs [based on estimates obtained from Bangs Laboratories, (Eq. 2.1), and Mie scattering [104]]. Similarly, drag force estimates are expected to vary by ±8%. The 1 μm PSMs were fluorescein-labelled to enable fluorescence imaging and aid in the visualization of particle motion. Certain molecules are tagged to the PSMs, usually polyaromatic hydrocarbons [105], which absorb photons of a specific wavelength (or energy), *e.g.* 490 nm blue light, and emit photons of a slightly longer wavelength, *e.g.* 513 nm green light. During the excitation process, a molecule's valence band electrons transition to an excited, or elevated energy state. Inter- and intra-molecular vibrations cause the electron to decay to a slightly lower energy state and finally to the ground state, thereby emitting a photon of slightly lower energy (Stokes' shift). The fluorescence lifetime is on the order of a nanosecond and is insignificant compared to the timescales of particle motion. The sphere concentration in water was dilute, approximately 0.01 - 0.001% by volume. The flow of particle solution into the chip was controlled with a syringe pump (Harvard Apparatus, Holliston, MA) and a standard 1 mL syringe press fitted to 100 μm inner diameter polymer tubing. Typical flow velocities were less than 300 μm/s and are comparable with velocities found in other optical-drag trapping experiments [77, 78]. Flow provided by the syringe pump was laminar and stepped flow induced by the pump's stepper motor was not visible for low flow rates. Figure 9 shows the experimental setup with employed components labelled.

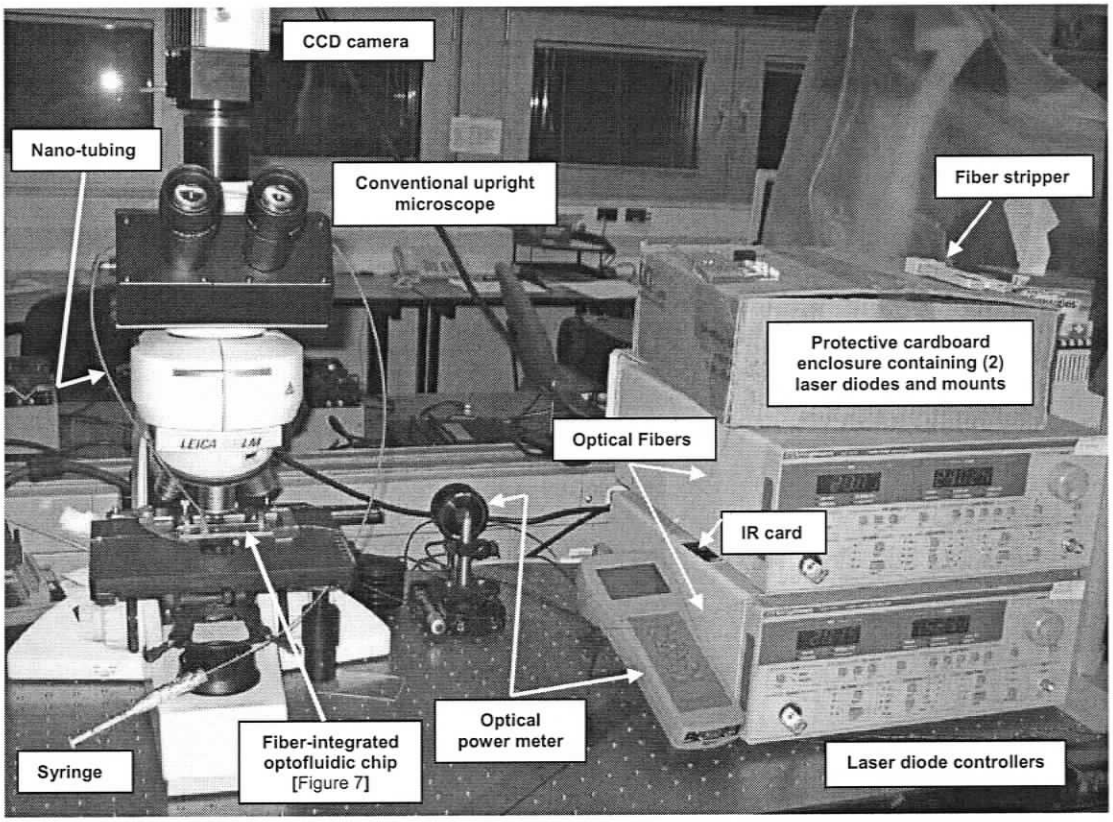

Figure 9 Experimental setup in the Microfluidics Lab at the University of Victoria. Typical components used are labelled.

4.3 Measurement and Imaging

Particles were imaged using standard fluorescence and bright field microscopy, where typically 20× (NA = 0.40) objectives (DMLM, Leica Microsystems, Germany) were employed on a conventional upright microscope. Video images at 30 fps were obtained using a Canon SD 400 CCD camera coupled to the microscope objective, while still images were often obtained using a pre-attached Retiga 1300i CCD camera. The acquired images had a resolution of 640 by 480 pixels and were exported in TIF format to MATLAB (Mathworks, Natick, MA) for post-processing. To facilitate fluorescence imaging, emitted light from a mercury bulb was shone through a microscope coupled blue band pass filter (~490 nm) and directed onto the fluorescent spheres through the standard objective lens. To determine particle paths, or streaks, the images were first normalized by subtracting a dark-field, added as matrices, then inverted and converted to

grayscale. Mean particle velocities and inter-particle spacing measurements were determined using known size calibrations (typically the fiber diameter) and pixel counting. Similarly, array oscillation periods were measured from known image capture rates (30 fps) and total exposure duration of all frames of interest. Each frame had a typical exposure time of 33 ms and the estimated imaging resolution with 10×, 20×, and 50× objectives was 2.3 pixels/μm^2, 9 pixels/μm^2, and 49 pixels/μm^2, respectively. Flow velocities were determined through particle tracking and streak imaging in the plane and region of interest. Uncertainties with this method arise when a tracked particle changes flow planes and is not visibly obvious, or accounted for, *i.e.* during a single frame's exposure time. This is generally corrected by averaging flow rate measurements. Other uncertainties include the extent to which divergent beam optical scattering forces have on tracer particles far up axis or within the outer limits of the MFD. The effects of optical interaction on tracer particles would act to underestimate flow velocities, however these effects were not visibly apparent on utilized tracer particles.

4.4 Summary

In this chapter, the steps involved with the fabrication of fiber-integrated optofluidic chips were discussed in detail. The adoption of established soft-lithography techniques allowed for the inexpensive rapid prototyping of PDMS microfluidic chips employed in this work. External imaging allowed for the characterization of particle trapping behaviour, flow velocity, and flow direction. The following chapter will present experimental results for systems containing one, two, and three fibers with dependencies on flow rate and fiber orientation.

CHAPTER 5

FLOW–DEPENDENT TRAPPING & MANIPULATION

In this chapter, the flow-dependent nature of single- and multi-particle traps are considered between counter propagating sources. Biased beam paths are shown to enable circulatory trajectories for trapped particles in a system with a defined flow rate and direction. Trapping directly against flow enabled a positional dependence on optical power and on flow rate, allowing for the demonstration of a simple flow rate meter. With a lensed fiber configuration, stacked particle trimming and mass particle swarms were observed. Regularly spaced numerous particle arrays in an upstream-oriented trap are also characterized and indicate a form of discrete particle waveguiding.

5.1 INTRODUCTION

While several trapping strategies are applicable to a flowing microfluidic environment, optofluidic trapping strategies that inherently incorporate a combination of angularly-biased optical and fluid drag forces have not been demonstrated to date. Optical and drag forces show distinct flow and power dependencies and represent two independent handles on particle control and a variety of potential lab-on-chip applications. Here, we demonstrate particle manipulation using a combination of optical and hydrodynamic forces. Flow imparts a Stokes' drag force onto the particles, which is a function of flow rate and direction. Light emitted from optical fibers impart photon momentum to particles in the axial direction (scattering force) and in the perpendicular direction (gradient force). Where the scattering force is also used as a propelling mechanism, the gradient force acts as an inward stabilizing mechanism. A variety of optofluidic trap configurations are developed and demonstrated using video microscopy and streak imaging. Through the combination of optical and drag forces, stable particle trapping,

circulating particle traps, and the trapping of an array of particles are demonstrated. In addition, a lateral, or axial, position dependence on optical intensity and flow velocity is used to control the size of stacked particle configurations.

5.2 Dual-beam Trap

Before considering the effects of microfluidic flow on optical trapping schemes, the case of a dual-beam fiber trap is investigated in the absence of flow. Figure 10(a) shows two overlaid images demonstrating stable particle trapping between two cleaved optical fibers. The fibers are transversely aligned to within 1.5 μm and separated laterally by 145 μm. Fiber 1 operates at 980 nm with optical powers varying between 25 mW and 122 mW and Fiber 2 emits at a wavelength of 1550 nm with a fixed optical power of 54 mW. The trapped polystyrene microsphere (PSM) was 9 μm in diameter and the largest displacement, Δz, achieved in this system was 104 μm. Equilibrium particle positions from the fiber facet vs. optical power are shown in Figure 10(b).

The positional dependence on power is non-linear due to Gaussian beam broadening, specifically, the intensity per unit area along the beam axis decreases non-linearly with increasing distance from the source (Eq. 2.16), and with losses through the medium. Additionally, at larger axial displacements, increasing optical power is needed to transition the particle by the same displacement because the intensity of the counter propagating source (Fiber 2) is increasing non-linearly with respect to the PSM's direction of motion. Trapping positions less than 80 μm from Fiber 1 showed a positional dependence on optical power of ~2.4 μm/mW and for larger displacements, ~0.4 μm/mW. The effects of a 1550 nm over a 980 nm source is expected to increase the radiation pressure cross-section on a 9 μm sphere by a factor of 1.13 as determined from Wiscombe's scattering algorithms [24, 104], resulting in a scattering force increase of ~13%, however absorption losses in water are expected increase at 1550 nm. Nonetheless the mid-distance equilibrium position occurred with both fibers emitting ~50 mW. The gas phase shown in the image was the result of optical joule heating induced by the 1550 nm fiber and is discussed further in §8.2. The remainder of this chapter will consider 980 nm sources, except where specified.

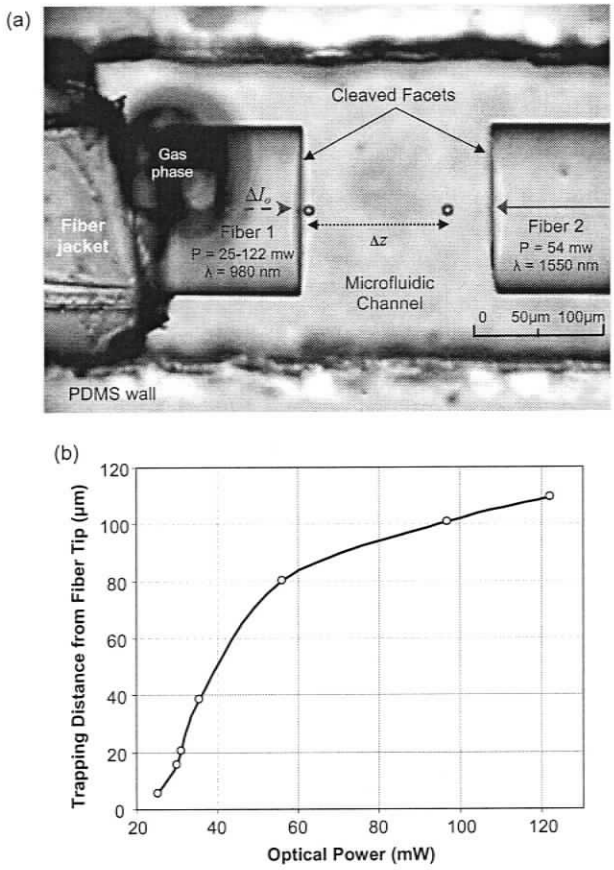

Figure 10 (a) Two overlaid images demonstrating single PSM displacement with increasing optical power from Fiber 1. The sphere shown has a 9 μm diameter. (b) Measured result showing PSM position as a function of optical power. The z-position displacement is with respect to the left fiber facet.

5.2.1 Transverse Offset Fibers

Figure 11(a) shows two cleaved single-mode counter propagating optical fibers separated by a vertical offset of approximately 8 μm and horizontal displacement of 75 μm. Output powers were ~100 mW at 980 nm. For zero and low flow conditions (0 - 20 μm/s), particles are shuttled back and forth along the parallel trajectories indicated due to optical scattering forces, F_{s1} and F_{s2}. Particle velocities up to 300 μm/s were obtained. Once the particles contacted the opposite fiber surface, a combination of particle grouping and optical gradient forces resulted in re-entrainment of the particles in the adjacent scattering beam and the process repeated.

For increased flow velocities (~40 μm/s), flow-induced drag forces, F_d, on the particle become large relative to the optical gradient force, and a particle propagating along the beam path of Fiber 2 may be re-routed midstream into the path of Fiber 1, as indicated in Figure 11(a). With the given offset geometry and flow direction, loop-back occurs only when propagating from Fiber 2 to Fiber 1 and in the clockwise direction. Similarly, a particle initially propagating along the beam path of Fiber 1 may be ejected from the beam path and proceed in the direction of fluid flow. As with the loop-back case, loss only occurs when being propelled by Fiber 1 due to the direction of flow. Figure 11(b) demonstrates these preferential loop-back, loss, and shuffle mechanisms with overlaid particle streak images. Where the particles contact the opposing fiber, they form pyramid-like groupings, as indicated by the dark areas on the facets of each fiber. The dark vertical streaks above the trapping region represent particle paths in the flow.

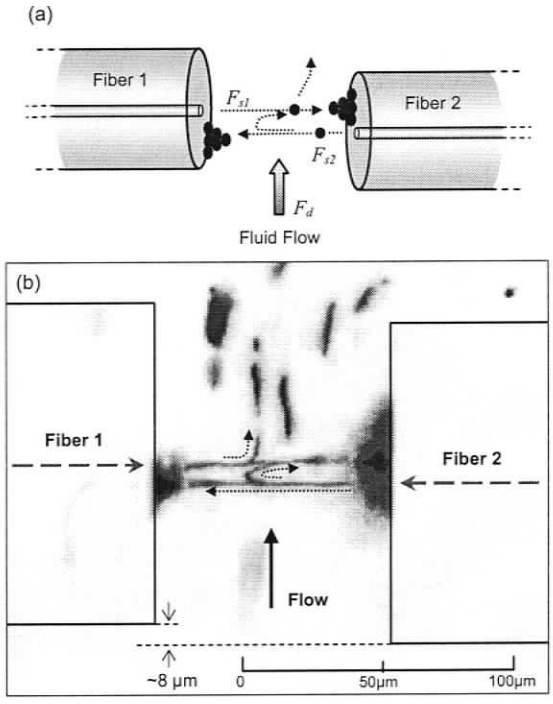

Figure 11 (a) Schematic showing parallel and offset cleaved optical fibers. Particles group and are optically propelled across the flow stream at low flow rates. Higher flow rates result in a preferential turn-around loop and particle loss in the direction of the flow. (b) Three overlaid sets of particle streak imagery demonstrating 1 μm fluorescent particle shuffling, loopback, and loss [13].

5.2.2 Angled Fibers

In Figure 12(a) a 2° angular offset is adopted for Fiber 2, where directions of optical scattering and fluid drag forces are indicated by the dashed lines. With this arrangement, the scattering force from Fiber 1 initially propels a particle to the right. As the gradient force from Fiber 1 weakens with axial distance, the combination of flow drag force, F_d, (velocity of 3 μm/s) and the gradient force from Fiber 2 provides sufficient upward force to draw the particle into the beam path of Fiber 2, where the scattering force, F_{s2}, then dominates. The particle now traverses the channel upstream to the left with a 2° offset, completing the circulation. A single-particle circulating trajectory is shown in the streak image of Figure 12(b). Similar trajectories for 2, 3, and 4 particle arrays were also observed with the long axis of the trajectory being longer than in the single particle case. The stability of the circulating traps was found to increase with increasing particle numbers, however, the 2° trapping configuration was extremely sensitive to flow in general. For flow velocities larger than ~3 μm/s, single particle circular trapping was not observed, and multiple particle circulations occurred for flow velocities up to ~9 μm/s. For larger flow rates, particles entering the trap location were propelled slightly right, then left, and lost to the flow. Reversed flow resulted in some particle path deviations, but no stable trapping. For this 2° trap configuration, stable particle circulations required a slight upstream fiber bias combined with a relatively low flow rate. This rotational scheme may find application in cellular microscopy where the rotation of symmetrical objects cannot be directly applied by conventional means [19, 102]. This demonstration would further benefit by adopting non-spherical trapping specimens, such as ellipsoidal particles, or half-hemisphere fluorescent spheres to conclusively establish that particles are rotating on their mutual axis through the course of a single circulation.

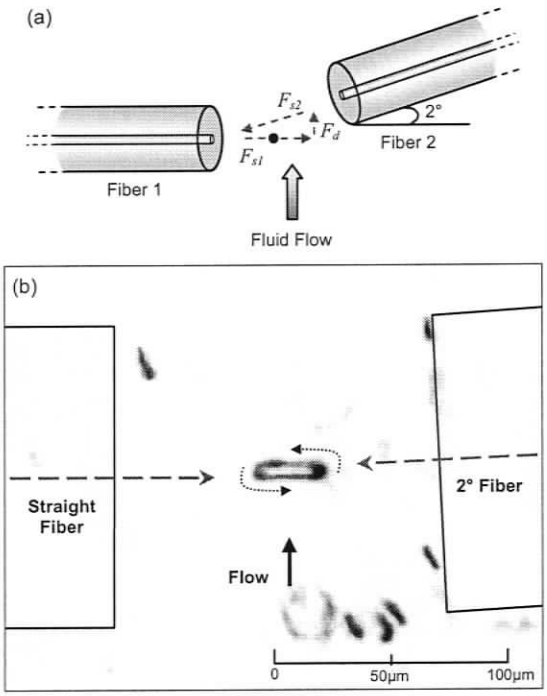

Figure 12 (a) Two optical fibers with Fiber 2 at a 2° angular offset with respect to Fiber 1. Elliptical circulation results for low vertical flow rates (mean velocity of 3 μm/s). (b) Streaking imagery of a single 1 μm fluorescent sphere undergoing elliptical circulation due to angular fiber offset and a low upward flow velocity of 3 μm/s (out of plane fluorescent particle rings have been edited for image clarity) [13].

Figure 13(a) shows two cleaved optical fibers, both of which are rotated in-plane by 10° and separated laterally by 150 μm. For low flow velocities (~17 μm/s at the midplane), stable, in-place, particle trapping was observed as the resultant scattering force, $F_{s,\,net}$, from the two fibers countered the drag force induced by flow, F_d. The trap location occurred at the intersection of the two beam paths. At higher flow velocities (~40 μm/s) multiple particle interactions induced counter-rotating particle paths as shown in Figure 13(a). The mechanics of this bowtie-like configuration are similar to those described earlier in the context of the circulating 2° trap. Figure 13(b) shows paths taken by 1 μm fluorescent spheres, where all trapped particles return to the point of beam intersection indicated by the dotted lines. Arrowheads shown in the zoomed portion of Figure 13(b) show the symmetric nature of the circulations, the left side being clockwise, and right side being counter-clockwise. Larger circulations, particularly visible on the left side, resulted from multiple particles orbiting together. As in the 2° trap case, vertical

streaking outside the trapping region indicated the flow direction and magnitude. Curvature in the flow field is visible near Fiber 1 due to chip manufacturing imperfections, however flow is locally straight on the scale of particle circulations at mid-distance between the fibers. As compared to the 2° case, the 10° trap showed stable and circulatory trapping at a larger range of flow velocities; this is attributed to a larger projection of the forward scattering force in the upstream direction. Large multi-particle circulations such as these may provide new opportunities for localized mixing of laminar streams in a microfluidic lab-on-chip.

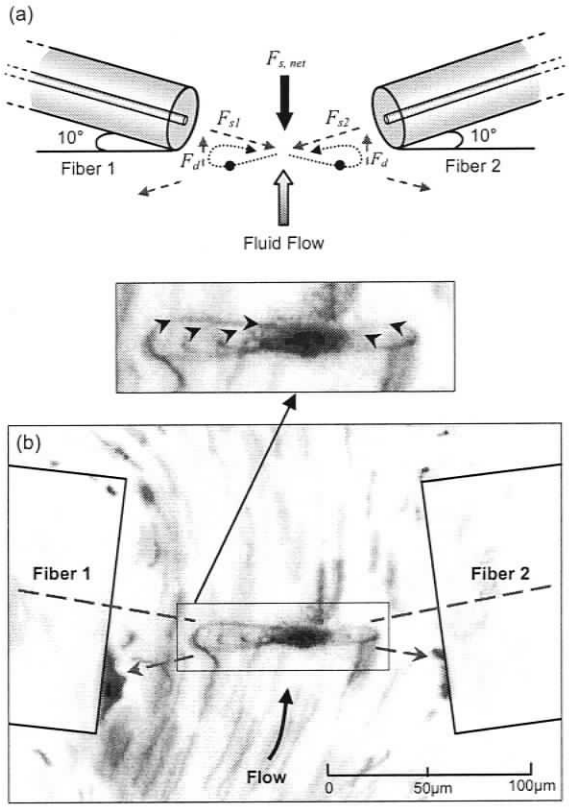

Figure 13 (a) Two 10° rotationally misaligned optical fibers with a varying upward flow rate. For flow velocities of 17 μm/s, stable particle trapping is observed for a single 1 μm particle. Increasing the flow rate by 150% results in dual counter rotating multi-particle trapping. (b) Overlaid particle images (~35) showing a bowtie configuration. Particles left of the trap centre undergo a clockwise preferential trajectory, while particles on the right undergo a counter-clockwise trajectory [13].

Figure 14 shows three fibers, two of which are counter-propagating (vertical) and another which is horizontal and offset by 10°. The vertical position of a 9 μm PSM at

location (1) was adjusted by tuning the optical intensities of Fibers 2 and 3 such that the PSM was positioned to intersect with the beam axis of Fiber 1. The flow velocity at the initial trapping position (1) was ~300 μm/s and in the direction identified by the flow arrow. The output powers of Fibers 1, 2, and 3 were 49 mW, 68 mW, and 56 mW, respectively. Consider a particle initially at equilibrium and located on the axis of the three fibers as depicted by position (1) in Figure 14. When the flow abruptly ceases (for a duration of ~0.03 s), scattering and drag forces no longer balance and the PSM spontaneously releases from the trap and is propelled along the axis of Fiber 1 to position (2). At this point, optical intensity will sufficiently diminish and Stokes' drag acts to transition the particle downstream to (3), where scattering forces from Fiber 3 propel it back to (1). The period for one oscillation was 2.5 s. The (1) to (2), (2) to (3), and (3) to (1) transition distances (and durations) for the 9 μm sphere were 111 μm (0.6 s), 106 μm (1.5 s), and 57 μm (0.3 s), respectively. The particle will remain at position (1) until the flow is again pulsed or until another particle falls within the beam axis of Fiber 3, thus disturbing the force balance at position (1). In the case of two circulating particles, impulse disturbances in the flow were not necessary for repeat circulation. PSMs with a 2 μm diameter were also found to circulate, however the period was 1.2 s and the (1) to (2), (2) to (3), and (3) to (1) transition distances (and durations) were 31 μm (0.3 s), 24 μm (0.6 s), and 26 μm (0.2 s), respectively. Alternately, it is expected that circulation will also occur for abrupt changes in optical intensity from Fiber 1 with flow constant.

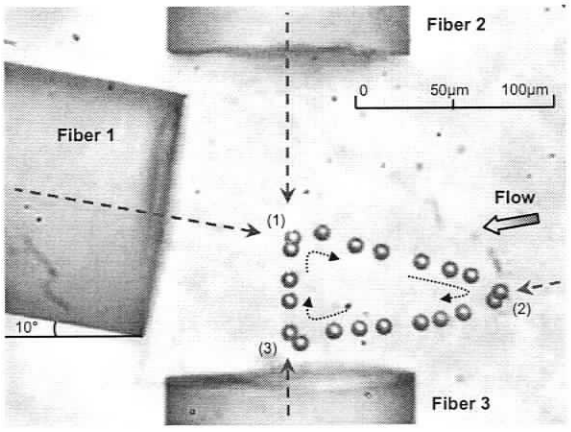

Figure 14 Overlaid images demonstrating single particle circulation with a three-fiber implementation and flow. The spheres shown in the image have a 9 μm diameter.

5.3 Upstream-Oriented Fibers

5.3.1 Particle-Optical Waveguide

A third flow-dependent optofluidic trapping strategy may be realized by directly aligning the forward scattering force with an opposing drag force. Implementing this strategy with a straight-cleaved fiber and counter-oriented flow resulted in a trapped array of 1 μm particles. A streak image of this (approximately) 50-particle array is shown in Figure 15. The trapped particles were stationary over the imaging period of 1 s and external particles indicated the flow magnitude and direction. The local flow velocity was estimated at 35 μm/s and the total array length was measured to be 340 μm. Unlike the situation described by particle-optical self-trapping [16], where a localized increase in the host fluid refractive index near a diverging beam induces waveguiding, each sphere in this array acts as a lens to refocus scattered light onto adjacent spheres, simultaneously guiding light and spheres upstream. The larger forward scattering force associated with cascaded focusing accounts for adjacent upstream particles obtaining an equilibrium position and allows for these long propagation distances and large numbers of trapped particles with orderly inter-particle spacing. The inter-particle spacing averaged over the array was 7 μm and the furthest upstream pairs had a closer spacing compared to the downstream particles by a factor of 2. This is comparable to the inter-particle spacing trend seen in dual fiber experiments utilizing a 980 nm source and 1 μm particles [14, 15]. Irregular gaps evident in the figure may be the result of positional delays of the particles or hydrodynamic effects, however viscous damping of the particles is almost instant.

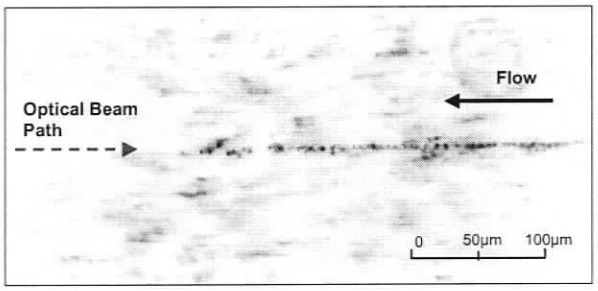

Figure 15 Time sequence imagery of a numerous ~50 particle array being trapped against low flow with planar velocity of 35 μm/s. In this case a cleaved single-mode fiber is used with flow being approximately antiparallel to that of the optical beam path [13].

Oscillations have been observed in dual-beam particle systems which may give insight as to the dynamics of the chain formation upstream [12, 14, 15]. Array lengths of up to 600 μm have been achieved, demonstrating a new regime of trapping [106] in which optical chromatography [29] is not applicable. In an optical chromatographic trap, the 1 μm spheres would be competing for a similar location along the beam axis to balance optical and drag forces. Array formations resulting from optical interactions between discrete particles have been demonstrated previously using counter propagating laser light [12, 84] single beam laser light acting against a wall [80], and with collinear optical fibers [81], and have the effect of waveguiding light through cascaded focusing. The present work is the first demonstration of particle array formations resulting from counter-oriented optical scattering and drag forces. Although stable over short periods (~1 s), this trapping mechanism was very sensitive to changes in flow velocity and particle concentration. A lack of long-term stability is attributed to the extended optical and fluidic particle-particle interactions resulting from a minimally divergent output beam.

5.3.2 Particle Position Control

Incorporating an optical fiber with a tapered, or lensed, tip introduces greater divergence in the beam geometry. At the employed wavelength, the beam was determined to be constantly diverging in the fluid medium. An upstream-oriented trap with lensed fiber is shown schematically in Figure 16(a) where F_s, F_g, and F_d represent the forward scattering, gradient, and drag forces, respectively. As shown, the axial position of the particle results from a balance of the forward scattering and drag forces; and gradient forces act to maintain the particle on the optical/flow axis. Unlike setups employed in optical chromatography, where a minimally divergent beam is used to create a long axial active region for particle sorting, we adopt a divergent PANDA-type 1550 nm lensed fiber to create a short working distance for flow monitoring. Additionally, the introduction of a taper reduces flow disturbances near the fluid-fiber boundary, which is beneficial for maintaining trapping positions near the fiber tip. In contrast to the upstream-oriented trap with straight-cleaved fiber, stable single particle trapping was demonstrated with the upstream-oriented lensed fiber, as shown in the particle streak

image of Figure 16(b) with a mean velocity of ~200 μm/s in the trapping plane. The particle trapped approximately 28 μm upstream from the fiber tip, located in a diverging beam with an estimated mode field diameter, $2w_o$, of 10 μm at the particle location (Eq. 2.15). The dependence of trapped particle position on flow rate was demonstrated with particles trapping further upstream for decreased flow rates. Likewise without applied flow, particles continued to be propelled in the forward scattering direction and no stable trapping occurred.

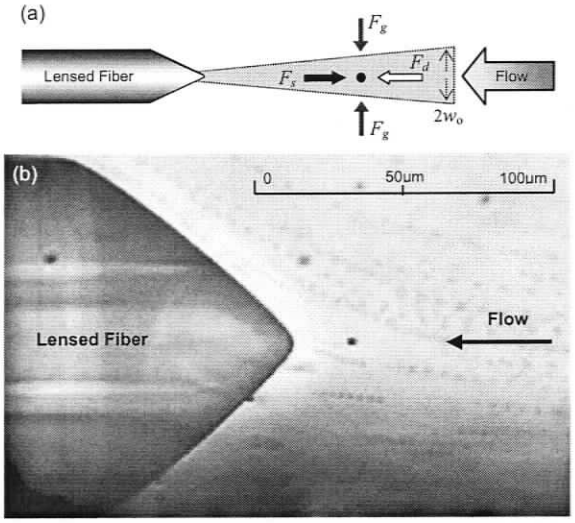

Figure 16 Upstream-oriented single particle trap. (a) Schematic showing the scattering force from a lensed fiber is used to balance the drag force induced by fluid flow on the particle. A lensed fiber is utilized to increase trap stability through the increased optical gradient force inherent to a diverging beam. (b) Time sequence imagery of a single 2 μm particle being trapped with an opposing flow velocity of 200 μm/s [13].

The axial force balance that enables the upstream-oriented trapping mechanism may be quantified using classical flow and optical Mie theory. For the upstream-oriented trap with lensed fiber configuration shown in Figure 16, the forward scattering force on the spherical particle due to optical momentum transfer is given in Eq. (2.1). The radiation pressure cross-section for the 2 μm sphere and was evaluated based on Wiscombe's Mie scattering algorithms [24, 104] and found to be approximately 0.66 μm^2. While it is difficult to predict the exact output beam geometry in water, an estimation was made based on input light characteristics, lens curvature and host medium refractive index. Using intensity estimates based on incident optical power, lensed fiber geometry, and

particle position, a scattering force of approximately 2.3 pN was determined, where the laser's output power, P, was measured at 30 mW. The mode field radius, w_o, at the position of the particle was determined from Eq. (2.15) and is a source of uncertainty in the present estimation. The actual scattering force is plausibly larger due to the presence of side lobes from a diverging beam which act to increase the average angle of scattered light, therefore increasing the radiation pressure cross-section and scattering force. More complicated computations [23, 30, 34-36, 40-43, 107] are possible for analysis, however they are beyond the scope of this work.

A counter propagating Stokes' drag force of approximately 3.8 pN is determined from Eq. (2.13), where η, r_o, and v were taken as 10^{-3} Pas, 1 μm, and 200 μm/s, respectively. The drag force provided here is expected to be overestimated somewhat as it does not include the potential effects of optical joule heating on fluid viscosity [108], and decreased flow velocities near the fiber tip. The estimated drag force value ($F_d \sim 3.8$ pN) is, however, in relatively close agreement with the order-of-magnitude optical force estimate from Eq. (2.1) ($F_s \sim 2.3$ pN), validating the optofluidic force balance trapping mechanism.

The force balance in conjunction with a diverging beam acting against constant flow indicates that particle position is a function of optical intensity. Varying the optical intensity by means of tuning the laser diode's input current enables particles to be translated upstream for higher intensities, or downstream for lower intensities. Similar methods of motion control have been demonstrated in systems consisting of two counter propagating laser beams [64] and in optical chromatographic particle separation configurations [29]. This method of motion control is shown in Figure 17 with two overlaid images, where the downstream particle location corresponded to a steady output optical power of 16 mW (6 μm from fiber tip) and the upstream location was achieved with 93 mW (79 μm from fiber tip). In both cases the sphere was stably trapped. The centre-to-centre displacement, Δz, was found to be 73 μm in a steady flow with mean velocity of 270 μm/s and indicates an average particle shift of 1 μm/mW, however particle displacements per milliwatt are not entirely linear over this range. Using estimates based on input light characteristics, lens curvature, and host medium properties, flow trapping displacements were compared with theory (Eq. 2.14) [29] as shown in

Figure 17(b) and were found to be in good agreement. Uncertainties in this calculation arise with estimations for the scattering efficiency, Q, and the mode field diameter, $2w_o$, which were taken at 0.5 and 7 μm, respectively. The trend shown here is similar to that observed in Figure 10(b) for the case of counter-propagating beams. The difference here is that the counter-propagating source (flow) is constant and the larger decrease in the power line slope of Figure 10(b) was due to a counter-propagating source with non-constant optical intensity.

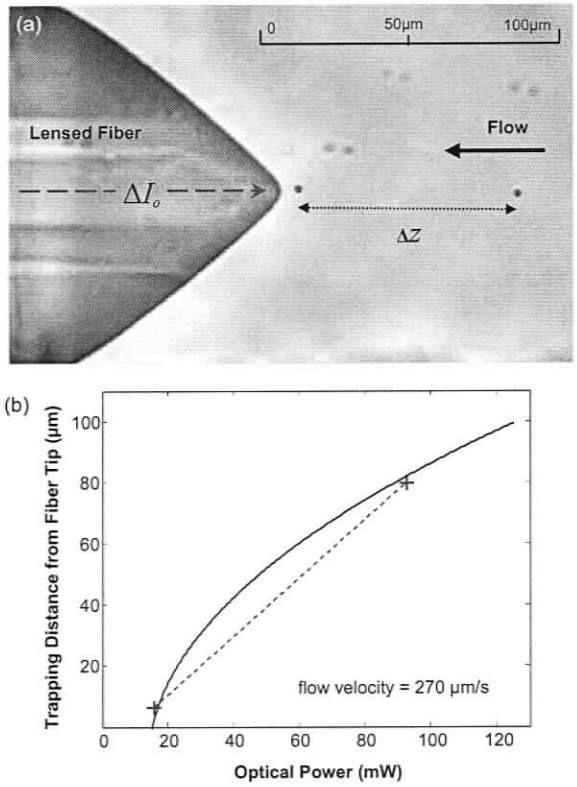

Figure 17 (a) Two overlaid images demonstrating displacement of a single 2 μm particle by varying the optical intensity in an opposing flow velocity of ~270 μm/s [13]. (b) Theoretical relationship between trapping distance and output optical power, where crosses indicate measured particle displacements and the dashed line represents a linearization in particle shift of 1 μm/mW.

5.3.3 Flow Rate Meter

Alternately, with constant optical power, the particle position could be changed via the fluid velocity. Fixing the output optical power at 93 mW while varying the flow velocity

yielded a positional trapping dependence on flow as demonstrated in Figure 18(a). In-plane flow measurements were obtained through particle tracking for separate flow tests. Particles trapping at 38 μm and 76 μm from the fiber for velocities of 804 μm/s and 312 μm/s, respectively. Measured velocities were compared with theory [29] as shown in Figure 18(b), where the crosses indicate measured displacements and the interconnecting dashed line represents an average particle shift of 0.08 μm for every 1 μm/s change in fluid velocity. A relatively small error of 3% occurred at the furthest upstream position, z_2, and a larger error of 15% occurred at position z_1, and may be the result of larger flow gradients near the fiber tip. Positional dependence on velocity enables on-chip flow rate monitoring that does not necessitate the need for specially dyed molecules, light sources, or streak imaging [105].

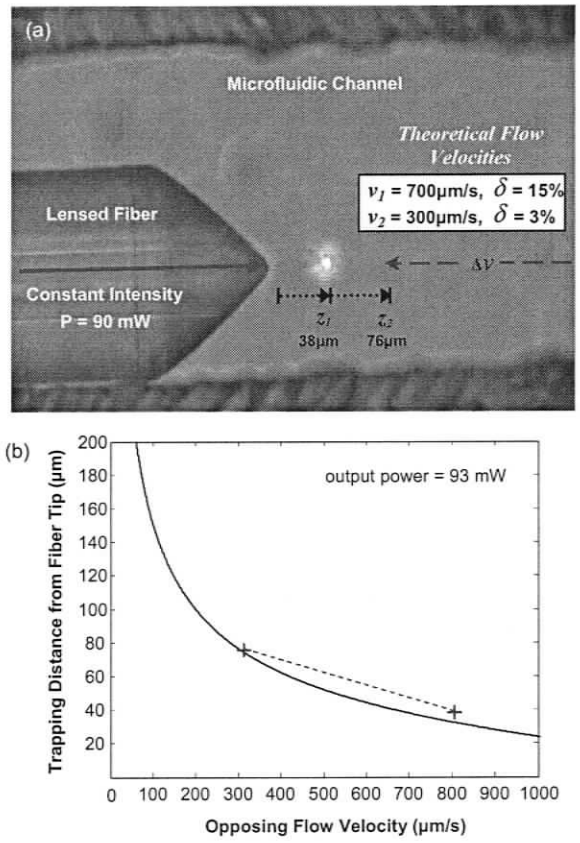

Figure 18 Application of a lensed optical fiber to monitor flow rate in a microfluidic channel. Theoretical relationship between trapping distance (2 μm spheres) and opposing flow velocity, where crosses indicate measured particle displacements and the dashed line represents a linearization in particle shift of 0.08 μm/(1 μm/s).

5.3.4 Particle Assemblies

In addition to single particle trapping, 2 μm particles joined in a line to form linear particle assemblies. In contrast to the spaced particle arrays discussed earlier, the particles in these configurations are in physical contact, and referred to here as particle assemblies. Such assemblies were observed only for 2 μm and larger particles in an upstream-oriented trap mode. With flow velocity and optical intensity constant, trapped axial positions of the particle assemblies were found to be a function of the number of particles, as plotted to scale in Figure 19. As the number of particles in the assembly increases, the increased drag forces are not sufficiently offset by the net optical scattering forces, and the equilibrium trapping position moves downstream towards the fiber tip, as indicated by the arrowheads in Figure 19.

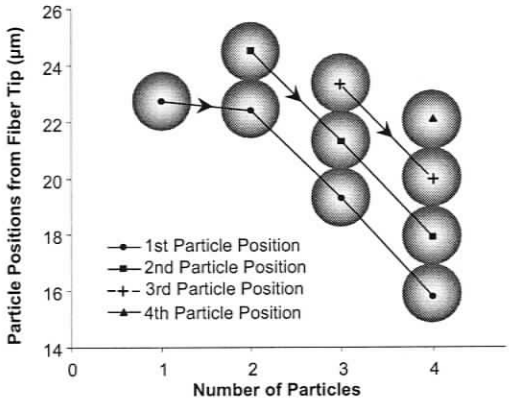

Figure 19 Plot of the equilibrium particle positions from the upstream-oriented lensed fiber tip for the 1st, 2nd, 3rd, and 4th particles in an assembly as a function of the total number of particles in the assembly (2 μm spheres were used). Particle sizes and displacements are to scale [13].

The upstream-oriented trap tended to collect particles over time, and in the case of 2 μm or larger particles, particle assemblies would form. The assembly in Figure 20 consists of three parallel stacked layers of 2 μm spheres with 3 spheres in each layer. Assembly translation is illustrated with the two overlaid images, where the left-most trap location occurred for an optical power of 20 mW and the right-most location for 80 mW. The centre-to-centre displacement, Δz, was measured to be 38 μm in a steady flow with mean velocity of 300 μm/s. As in the case of a single trapped particle, if optical intensity

is held constant, the particle assembly will remain trapped in position as long as flow remains constant.

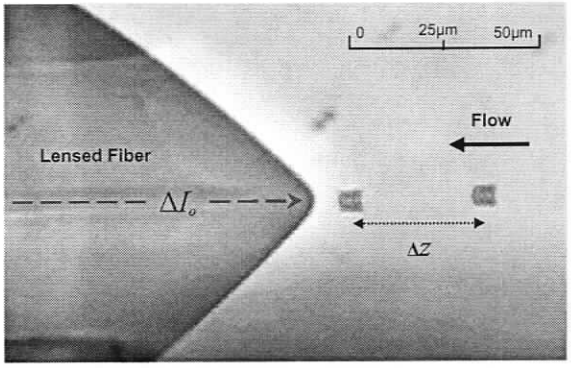

Figure 20 Two overlaid images demonstrating active optical repositioning of a 9-particle assembly of 2 μm spheres in an opposing flow velocity of 300 μm/s.

In the context of particle assemblies, a method to trim the number of trapped particles is desirable. Reducing optical intensity provided a mechanism to actively tune the number of trapped particles. Figure 21(a) shows a five-particle assembly of 2 μm spheres undergoing stable flow-dependent trapping. As optical power was reduced, the assembly moved downstream towards the fiber-fluid boundary where flow gradients exist across the particles as shown in Figure 21(b). Near to the fiber tip, drag forces on upstream particles will be larger compared to drag forces on downstream particles. At the upstream location, scattering forces can no longer offset the influence of drag, and a particle is lost to flow. In addition, a larger vertical flow component at this boundary further reduces particle stability, particularly due to the relatively weak gradient force in these systems. The remaining trapped particles could be repositioned upstream, as shown in Figure 21(c), by increasing optical power. This process was then repeated as in Figure 21(d)-(e) to eliminate additional particles, however, careful control of optical intensity was needed to ensure that the entire assembly was not lost to downstream flow.

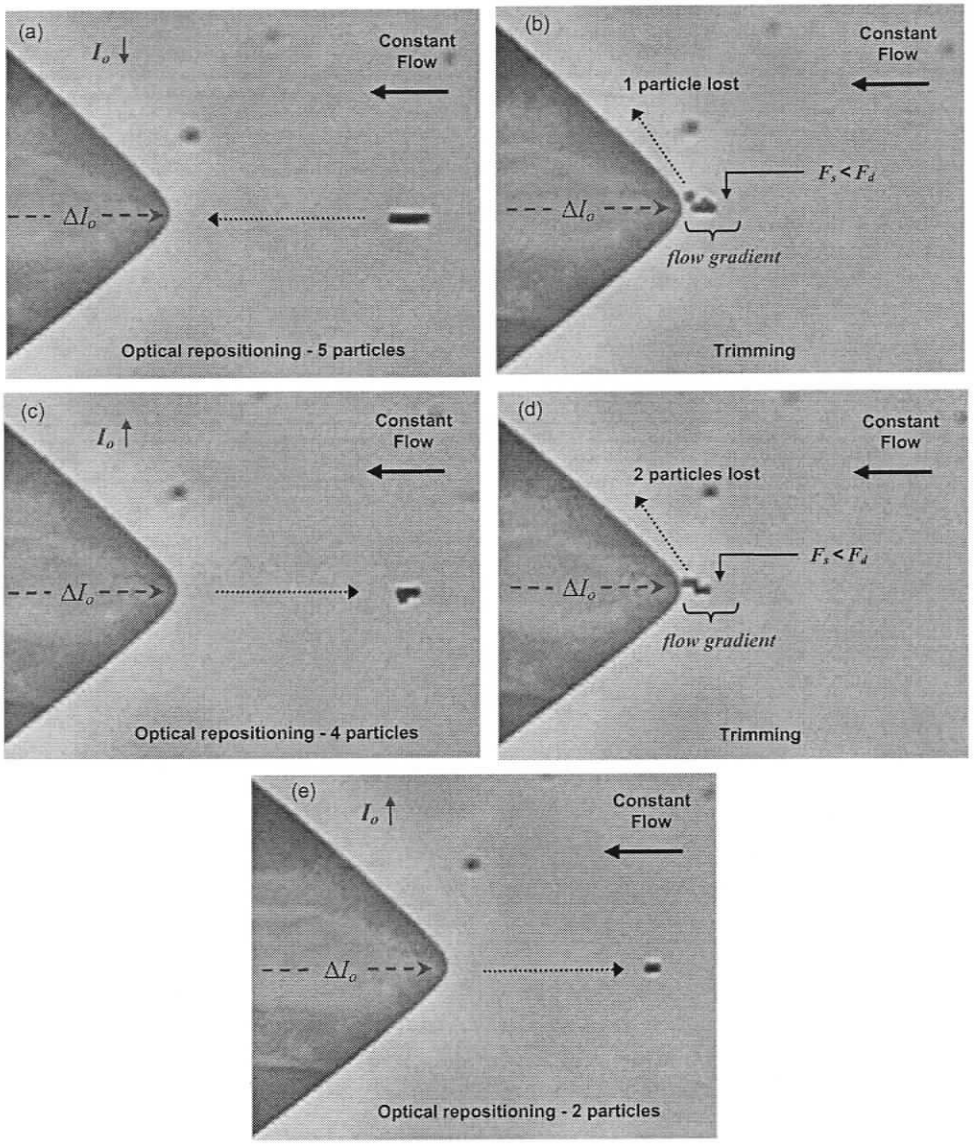

Figure 21 Still images demonstrating assembly size-tuning with the upstream-oriented trap. The in plane flow velocity was fixed at 200 μm/s and the sphere diameter is 2 μm. (a) A five particle assembly is repositioned downstream by decreasing the optical intensity. (b) One particle being trimmed from a five-particle assembly. (c) The remaining four particles once translated back upstream by increasing the optical intensity. (d) Two additional particles trimmed. (e) The remaining two particles trapped upstream [13].

5.3.5 Particle Arrays

In upstream-oriented traps with a lensed fiber, 1 μm particles did not form assemblies with particles in apparent contact. Instead, orderly array-style inter-paticle spacing was observed for these smaller particles. The regime change from assemblies of 2 μm particles to arrays of 1 μm particles is attributed to an increase in optical scattering forces associated with smaller particles. This larger optical scattering force component may be related to an increase in diffracted light around smaller spheres, such as with dielectric surface waves [21, 109], thus imparting an additional force to adjacent particles, or to smaller spheres containing more angular components of forward scattered light (where certain particle sizes and wavelengths create a resonance condition which enhances the radiation pressure cross-section from what is expected [106]) as compared to larger spheres. The coupling of whispering-gallery modes from a pair of transparent microspheres can also lead to separation-dependent resonant optical forces between spheres [87]. In contrast to the similar flow-trapped arrays using a cleaved fiber (Figure 15), the inter-particle spacing in a lensed fiber trap was found to vary strongly in the axial direction in response to the increased beam divergence as shown in Figure 22. The inter-particle arrowheads in Figure 22(a) depict downstream particles refocusing the predominantly forward scattered light onto adjacent upstream particles. Figure 22(b) shows a time sequence image of an 8-particle array with an orderly upstream decrease in inter-particle spacing being trapped with an opposing 130 μm/s flow velocity. Particle displacements were measured with reference to the furthest downstream particle ($z = 0$) and are shown in Figure 22(c) to increase nonlinearly in the forward scattering z-direction for the i^{th} particle. Similarly, the trend in inter-particle pair spacing was found to decrease with increasing distance upstream as in Figure 22(d). For more than 8 particles, furthest upstream particles formed a pressed chain as in Figure 19, while downstream particles maintained regular inhomogeneous spacing. Previously reported arrays using counter-propagating beams showed particle spacing to vary parabolically, forming a potential well of minimum energy [12]. Regular particle spacing may be due to spheres acting as quasi point scatters, thereby interfering with incident light to form an up-axis interference pattern [81] or to the quantized nature of reradiated photon

momentum. With the optofluidic array trap demonstrated here, specific inter-particle spacing is attributed to a combination of diverging beam geometry, hydrodynamics, particle-particle optical interactions, and optical losses through the medium. This self-organization of matter in a balanced optical-drag system offers a new approach for studying optical interactions between particles, with applications involving contact-free storage of biological cells [81].

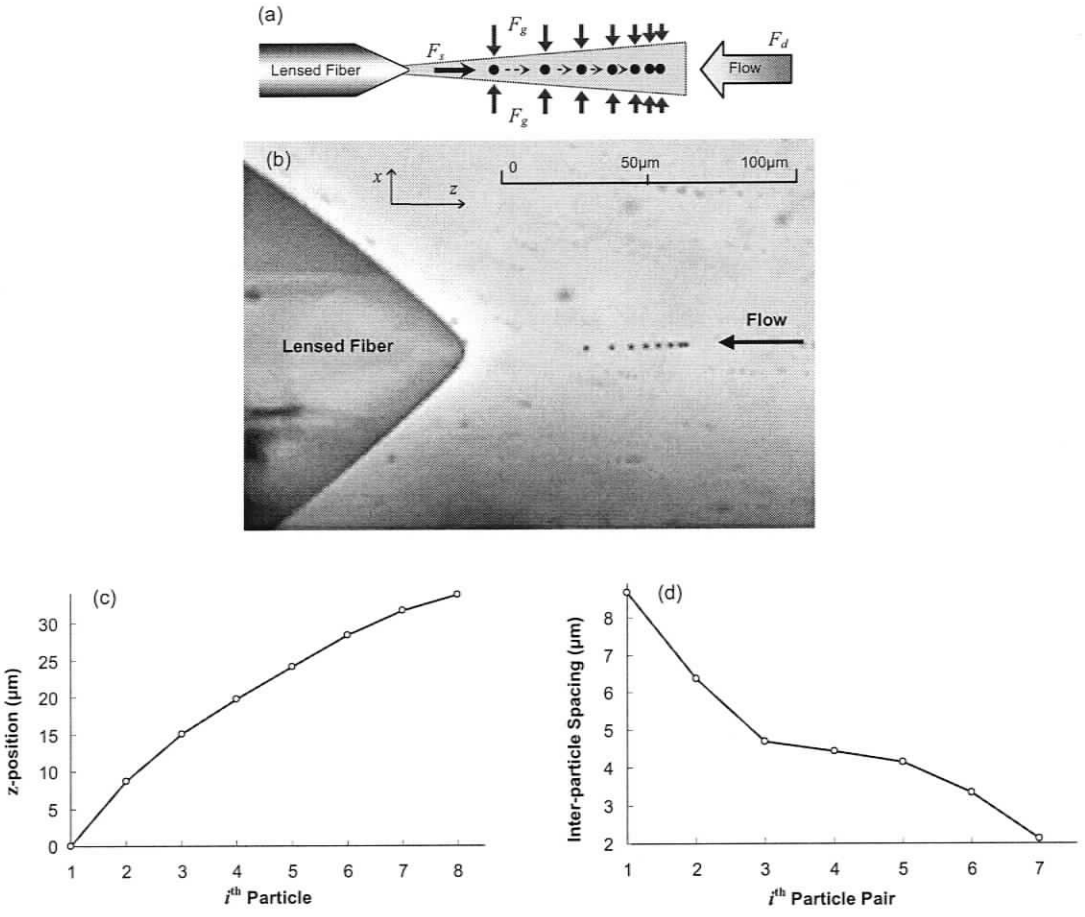

Figure 22 Upstream-oriented array trap. (a) Schematic of an array of 1 μm spheres trapped against fluid flow leading to varying inter-particle spacing [13]. (b) Time sequence imagery of an 8-particle array being trapped with an opposing flow velocity of 130 μm/s. (c) Nonlinear increase in the position of the i^{th} particle. (d) Decrease in inter-particle spacing for further upstream particle pairs.

5.3.6 Particle Swarms

Circulating optical trapping is considered again where high concentrations of 2 μm PSMs were found to swarm with preferential counter-rotational trajectories at high output powers (120 mW). In Figure 23, particles are initially propelled upstream by the optical scattering force where they enter and form a swarm centre. Once particles reach the furthest upstream position, fluidic drag acts as a loopback mechanism to move particles downstream forming the swarm edges, where at a distinct position scattering forces dominate again to transition particles back upstream. The formation of swarming particles instead of particle assemblies is attributed to the increased significance of inter-particle hydrodynamic interactions at high particle concentrations and gradient optical forces at the estimated equilibrium position of ~140 μm from the fiber tip. Particles at this location are only weakly held to the propagation axis due to beam broadening and particle interference. Particle trajectories were found to be clockwise for the lower half and counter-clockwise for the upper half of the swarm. Flow velocities were measured at 200 μm/s in the trapping plane and the maximum vertical diameter of the swarm was 30 μm.

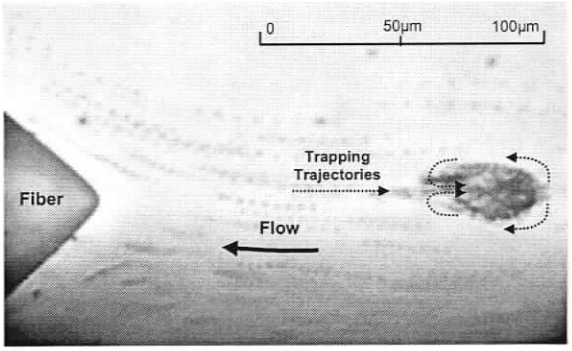

Figure 23 Time sequence imagery of 2 μm spheres undergoing counter-rotating circulation. Trajectories taken are indicated by the dashed lines and accompanying arrows.

5.4 Summary

In this section, new particle trapping capabilities were demonstrated through the planar integration of optics and fluid drag to actively control trapping dynamics. Through selective biasing of in-plane counter propagating optical sources, flow is employed to create single and multi-particle circulations. The functionality of these flow-induced circulation trap modes can be extended to enable the rotation of trapped specimens or to applications requiring microfluidic mixing in a localized environment. In cases where a single upstream-oriented fiber was used, optically and hydrodynamically bound arrays of numerous particles were demonstrated. This organization of matter could lead to methods for large-scale cell confinement used in bio-analysis or for particle counting through optical feedback. Single-particle trapping and precise axial position control was possible in systems containing an upstream-oriented lensed fiber. A positional dependence on optical intensity (constant flow) and flow velocity (constant intensity) was observed. The knowledge of a trapped particle's position in a given flow may be useful for designing new devices for flow rate monitoring and calibration. In the following chapter, the subject of particle array spacing, such as that observed in §5.3.5, will be studied in further detail in the context of a dual-fiber trap.

CHAPTER 6

OPTICALLY-BOUND ARRAYS IN A DUAL-BEAM TRAP

In this chapter, a general opto-hydrodynamic theory is adopted to verify experimentally observed array dynamics and amplitude modulation in two dimensions. The theory agrees, qualitatively and quantitatively, with the observed inhomogeneous self-organization dynamics of particles in optically-bound linear arrays. Inhomogeneous inter-particle spacing and the onset of spontaneous oscillation for a critical number of particles are also reproduced by the theory. The dynamic simulation shows that the critical onset of oscillation is caused by a misalignment of the beam axes, as is found in the experiment.

6.1 EXPERIMENTAL RESULTS

Figure 24(a) shows the dual-beam fiber-optic experimental setup used to observe self-organization and oscillations of particles. The two cleaved facets of the fiber were separated by 160 μm and emit light along the z-axis. Each fiber emits 100 mW of light from two separate fiber-coupled 980 nm laser diodes. The beam-width at the fiber was approximately 6 μm. The combined fiber length was 2 m, which is far greater than the coherence length of these lasers, so coherent interference was absent. The experimental parameters chosen here are similar to past works [12, 13, 83, 86].

As shown schematically in Figure 24(a), the dual-beam trap balances the counter-propagating scattering force on the polystyrene microsphere (PSM) from each beam in the z-direction when the fiber offset, D_{off}, is small, or when the sphere is sufficiently large compared to the offset. A trap is formed in the x-direction by the gradient force, where the PSM is pulled in the direction of increasing optical intensity. For intentionally biased

or angled fibers, Figure 12 demonstrated single particle oscillation. Figure 24(b) shows self-organized linear arrays of PSMs stably trapped between the optical fibers. The spacing between the PSMs is dependent on the number of particles in the array, and the PSMs closest to the centre of the trap have a closer inter-particle spacing. Figure 24(c) shows the onset of self-sustained oscillations for 13 PSMs with an x- and z-direction amplitude of 3.1 μm and 19 μm, respectively. The period of oscillation was 0.5 seconds and the transverse fiber offset was 4 ± 1 μm. For this system, 11 or less PSMs stably trapped while small amplitude fluctuations occurred for 12 PSMs. For 13 or more PSMs, spontaneous oscillation occurred.

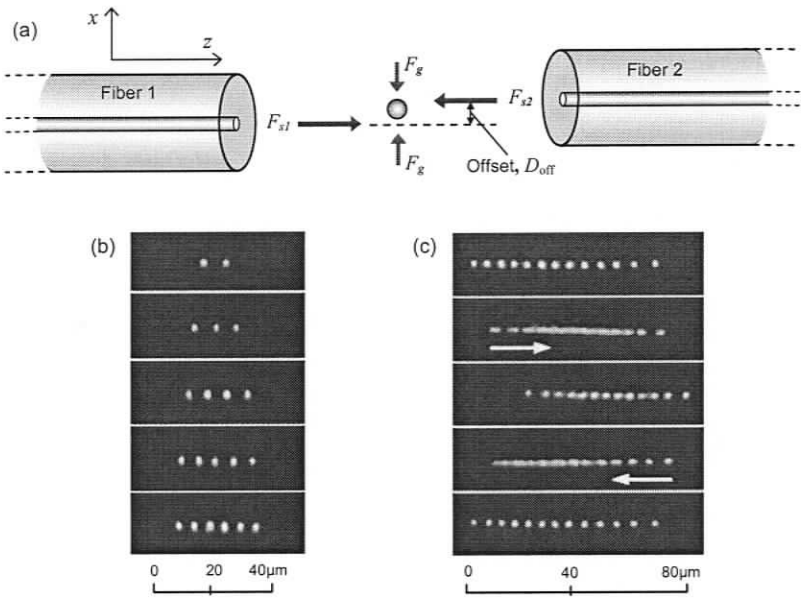

Figure 24 (a) Schematic of a 1 μm dielectric particle trapped within a dual-beam fiber-optic trap. The gradient force pushes the particle in the direction of increasing beam intensity along the x-axis and the counter-propagating scattering forces are balanced to position the sphere between the optical fibers. F_{s1}, F_{s2} are the optical scattering forces from Fibers 1 and 2, and F_g is the gradient optical force. (b) Still images of self-organized linear arrays of stably trapped fluorescent PSMs for 2 to 6 particles [14]. (c) Images of an oscillating array of 13 particles with 0.5 s period [14].

Experiments were repeated with an offset between the fibers of 5 ± 1 μm. For this condition, the onset of oscillation occurred for less PSMs and smaller amplitude oscillations of approximately 9.3 μm in the z-direction and 2.6 μm in the x-direction were observed for 8 PSMs. The period of oscillation was also 0.5 seconds. For the same

offset, with 13 PSMs, the z- and x-direction amplitudes were 32 μm and 5 μm, respectively. For larger offsets, z-direction amplitudes are greater because a longer axial transition distance is needed before the opposing beam intensity is sufficiently large to draw particles in by gradient forces. The increase in x-direction amplitude follows directly from the increase in radial offset. Figure 25(a)-(b) shows the measured trajectory of the outermost PSM for the case of 13 and 8 PSMs. The solid data point represents the PSMs initial position and the solid line indicates the trajectory taken over one period of oscillation. Paths for the inner particles followed similar trajectories, however amplitudes decreased by ~2%.

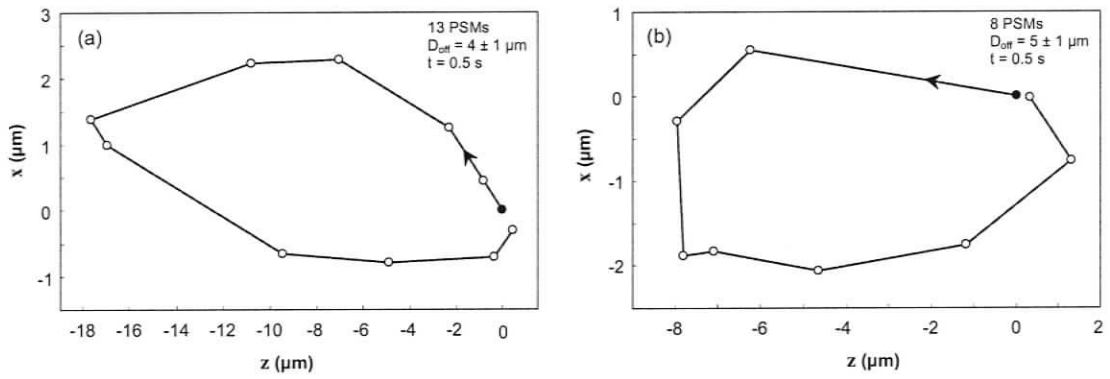

Figure 25 (a) Experimental trajectory in the x-z plane of outermost particle for 13 PSMs when the fibers were offset by 4 ± 1 μm. The starting point (arbitrarily assigned at the origin) is shown with a solid circle and the direction of oscillation is shown with an arrow. (b) Trajectory of the outermost particle for 8 PSMs when the fibers were offset by 5 ± 1 μm [14].

6.2 Opto–Hydrodynamic Theory

To understand the optical interactions shown in Figure 24, an opto-hydrodynamic theory is adopted through collaborative research with Dr. Kawano. Although analytic solutions exist for the optical interaction between particles, these are only valid in the Rayleigh regime [45]. The theory here uses a generalized multipole technique (GMT) to describe the light scattering from the PSMs [34]. This method can be applied in both the Rayleigh and Mie regimes, including a high refractive index contrast. As the particle size and/or the refractive index contrast become larger, higher orders of basis expansion are needed, which means a larger sized matrix equation should be solved. The GMT expands the

scattered electric field outside the particles using a series of Hankel function vectorial spherical waves, and inside the particles using a series of Bessel function vectorial spherical waves. The corresponding magnetic field is calculated from the electric field using Maxwell's equations. Boundary conditions at the surface of each sphere are matched using an integral least-squares fit to determine the coefficients of the vectorial spherical waves. Convergence was found with the number of basis functions for each PSM truncated at less than 10. Once the electromagnetic field is calculated using GMT, Maxwell's stress tensor (MST) analysis is used to calculate the forces on each particle. The forces were then used to calculate the incremental trajectory for each particle, and the process was repeated. To further validate the GMT, a finite-difference time-domain (FDTD) method was used, with good quantitative agreement. The FDTD method can be used for arbitrary particle shapes, not only spheres, however calculation time is prohibitive. The GMT theory is generally applicable, and it may be used to explore the dynamics of PSMs in other experimental configurations, such as those demonstrating optical binding [80], not limited to the configuration depicted in Figure 24. Extended detail on the opto-hydrodynamic theory used for particle array simulations has been reported in a joint publication with Dr. Kawano [15] and can be found simultaneously in the Appendix.

6.3 Stationary Particles

Figure 26(a) shows the observed equilibrium particle positions for up to 12 particles for a given beam offset, $D_{off} = 0$. For more than twelve particles, the experiments showed self-sustained particle oscillation as measured in Figure 25(a). For comparison, the stationary particle positions as calculated using the opto-hydrodynamic theory are also shown. It is clear that there is good quantitative agreement between the theoretical and experimental positions for arrays up to 12 particles. The calculation parameters were chosen to match the experiment, shown in Figure 24. A fifth-order Gaussian beam with width equal to the fiber-optic beam width was used to approximate the emission from each fiber. It is expected that the Gaussian will slightly underestimate the diffraction from the fiber, since it is multi-mode at 980 nm, and this is a source of error in the present representation of

the theory. It should be emphasized that the opto-hydrodynamic theory parameters were determined a priori from the experiment using the accepted material parameters - no fitting was attempted a posteriori.

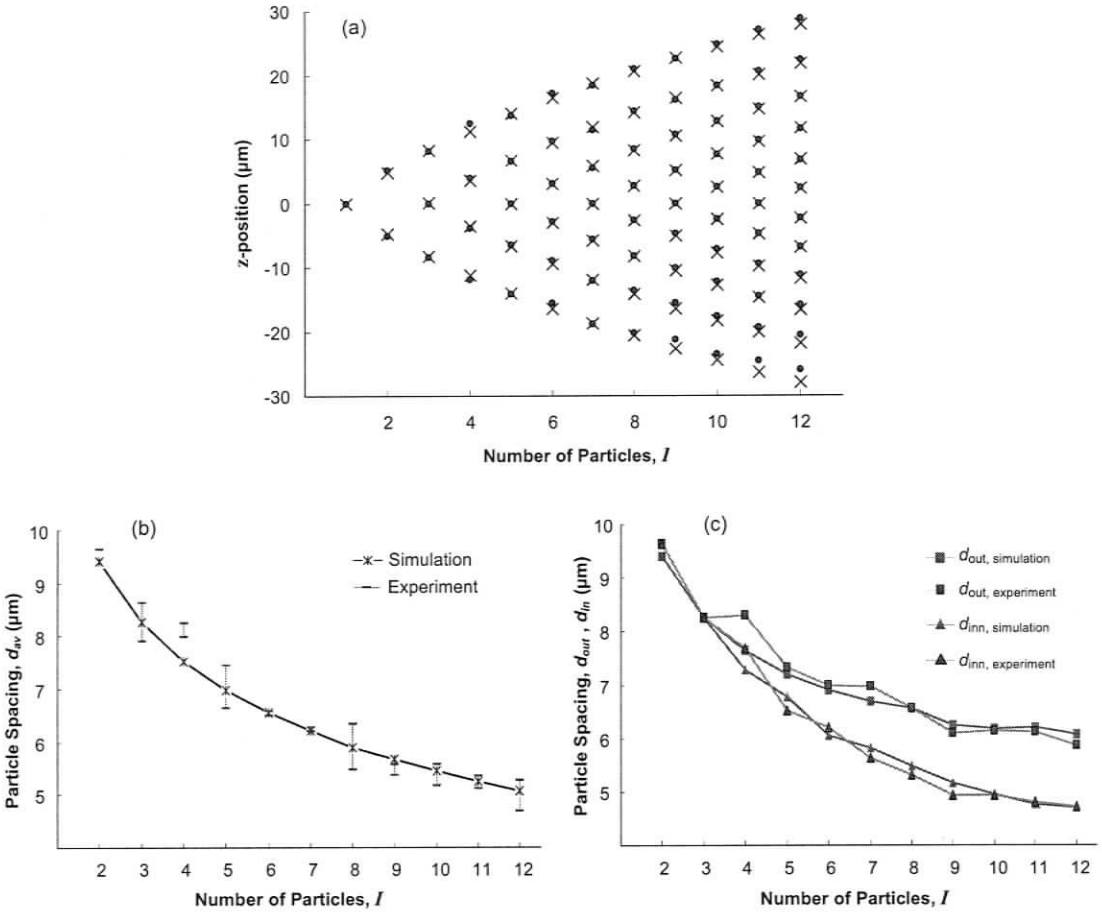

Figure 26 Inhomogeneous properties of inter-particle spacing. (a) Equilibrium positions of PSMs in a dual-beam optical trap for different numbers of particles forming the arrays, calculated using the opto-hydrodynamic theory (×) and as observed in the experiment (•) (averaged over several trials to remove small thermodynamic fluctuations) [14]. The z-positions are with respect to the central particle. (b) Averaged inter-particle spacing, d_{av}, as a function of the number of particles, I. A standard deviation plot is applied to the experimental results [15]. (c) The inner most inter-particle spacing, d_{inn}, and the outer most inter-particle spacing, d_{out}, as a function of I. Blue and red positions denote theory and experiment, respectively [15].

To find the stationary particle positions, the calculation method was to introduce a particle offset from the other particles and then to integrate in time until all the particles reached their equilibrium positions. The particles showed an exponential approach to their equilibrium positions. The final equilibrium positions were not dependent on the hydrodynamic coupling between the particles - when this coupling was artificially removed, the same final positions were found. This is expected because the hydrodynamic interaction is mediated through the motion of fluid, and in the stationary state, there is no fluid motion. The rate of approach to the final positions, however, visibly decreased when the hydrodynamic interaction was removed.

Previously, the self-organization of particles into a stationary linear array in a dual-beam trap was attributed to the approximately parabolic optical potential created by two counter-propagating beams [12]. In that work, the interaction between the particles was considered to increase the overall energy in the potential and reduce particle spacing. It has also been observed in the experiments and opto-hydrodynamic theory that the average inter-particle spacing, d_{av}, decreases nonlinearly as more particles are added to the array, as shown in Figure 26(b). A past work has described the particle spacing as regular [81]. Contrary to that work, the optical interactions between the particles given in Figure 26(c) show inhomogeneous inter-particle spacings. In particular, particles near to the end of the linear array have a further spacing, d_{out}, than those towards the centre, d_{inn}, and that the difference between the two increases with increasing particle numbers. Alternately, for a fixed 12-particle array, the transition from outer to inner inter-particle spacing is depicted by the trend given experimentally in Figure 27(a) and compared theoretically with the MST-GMT simulation results in Figure 27(b). The general trend is in agreement with results observed in Figure 22(d) for a single beam acting against flow, specifically that a sharp decrease in spacing initially occurs, followed by an area of minimal decrease (plateau), and continued by another sharp decrease when translating from the outer to the inner particle pairs. The absence of a counter-propagating optical source serves as additional justification that standing wave interference does not play a significant role in the formation of self-organized regularly spaced arrays.

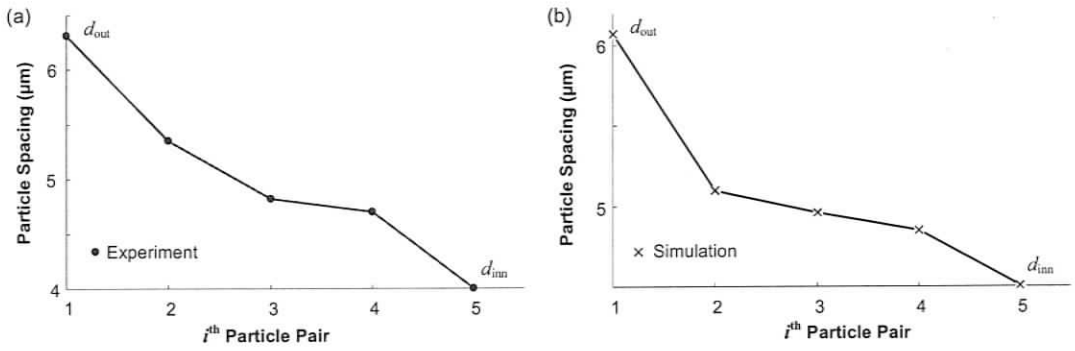

Figure 27 Decrease in inter-particle pair spacing for the first 5 pairs of a 12-particle array.

Standing wave interference occurs when two counter-propagating coherent electromagnetic waves interfere, usually within the coherence length of a laser. The coherence length determines how far spatially (and in time) a wave is perfectly coherent, that is, for what distance a wave will remain in phase. For a wave that is in phase, all points on its waveform remain predictable. A sine wave, for example, exists only for a finite time duration, Δt, and length, l, then becomes unpredictable, *i.e.*, is no longer a perfect sine wave and contains a number of different frequencies in its spectrum. The coherence length is defined as $l = c\Delta t = c/\Delta f$, where $\Delta f = c\Delta\lambda/\lambda_o^2$. A typical 100-200 mW, 980 nm fiber pump laser diode has a spectral width, $\Delta\lambda$, of ~2 nm, resulting in a coherence length of 480 μm. The coherence length of the lasers employed in this work is, therefore, much longer than the separation distance between the two laser sources (2 m) and standing wave interference is not pronounced, existing only instantaneously and at randomly changing positions. Any momentary coherence will be rapidly lost and these momentary standing wave patterns will not influence particle equilibrium positions.

The inhomogeneous spacing arises from the optical interaction - while each particle alone has a reduced scattering force away from the source of the divergent beam, the forward Mie-scattering from adjacent particles increases the scattering force as the particles are brought closer together. For this particle size, backward Mie-scattering is negligible. The force from Fiber 1 equals the force from Fiber 2 at equilibrium, as depicted in Figure 24(a). To achieve this balance, the force from each fiber increases towards the center of the array by Mie-scattering, then decreases. The inward force on each end particle is the scattering force from the nearest fiber, without optical interaction.

Figure 28(a) shows the calculated forces using the opto-hydrodynamic theory, for the 7-particle case, where the maximum force (from one fiber only) is in the centre of the array, where the particles are more closely-spaced. The MST-GMT model reproduces the standing-wave modulation in the force distribution (Figure 42, Appendix) reported previously for two particles [45], that leads to bistability [83], however for the parameters of the experiment, the modulation is weak and it does not play an important role in the observed large-scale dynamics.

Figure 28(b) shows that the optical interaction between the particles tends to focus the scattered near-field electric-field intensity towards the centre of the array, again where the strongest optical interaction is felt and the particles are closest.

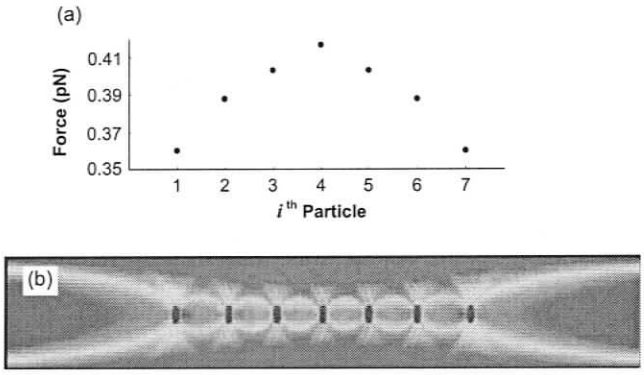

Figure 28 (a) Calculated forces on each particle from a single beam [14]. (b) Calculated near-field scattering of the electric field from both beams in the x-y plane [14].

6.4 Array Oscillation

When the counter-propagating beams were perfectly collinear, the theory showed no particle oscillations. Symmetry breaking, in the form of a small transverse offset (x-direction in Figure 24(a)) between the two beams, leads to the spontaneous emergence of self-sustained oscillations for a critical number of particles and offset. Symmetry breaking was observed in the experiments for equilibrium positions of PSMs (Figure 26(a)) - particularly for the asymmetric outer-particle positions in the 12-particle array. In past works, self-sustained oscillations were observed to occur spontaneously for more than 7 PSMs [12]. In our initial experiments, the critical number of PSMs required to

observe oscillation was 13 for an offset, D_{off}, of 4 ± 1μm. Additional experiments were performed with the fibers offset by 5 ± 1 μm, with oscillations appearing for 8 PSMs.

Figure 29(a) shows the dynamic x-z trajectory of the outermost PSM in a 7-particle array with a 4 μm x-axis offset between the beam paths. The offset is 4 sphere diameters, which is less than the beam diameter of the divergent beams and significantly less than the separation between the fibers. This trajectory shows a damped oscillatory behaviour for this offset, resulting in a final resting position. The x-offset final position of the particle is due to the optical interaction with other PSMs, and to the offset of the beams with respect to their optical axes. For several small variations, it was found that the final steady-state positions did not depend upon the initial conditions. For a greater offset of 5 μm, the trajectory spiralled outwards towards a stable oscillating limit-cycle as in Figure 29(b), with a *z*- and x-direction amplitude of 21.1 μm and 3.1 μm, respectively.

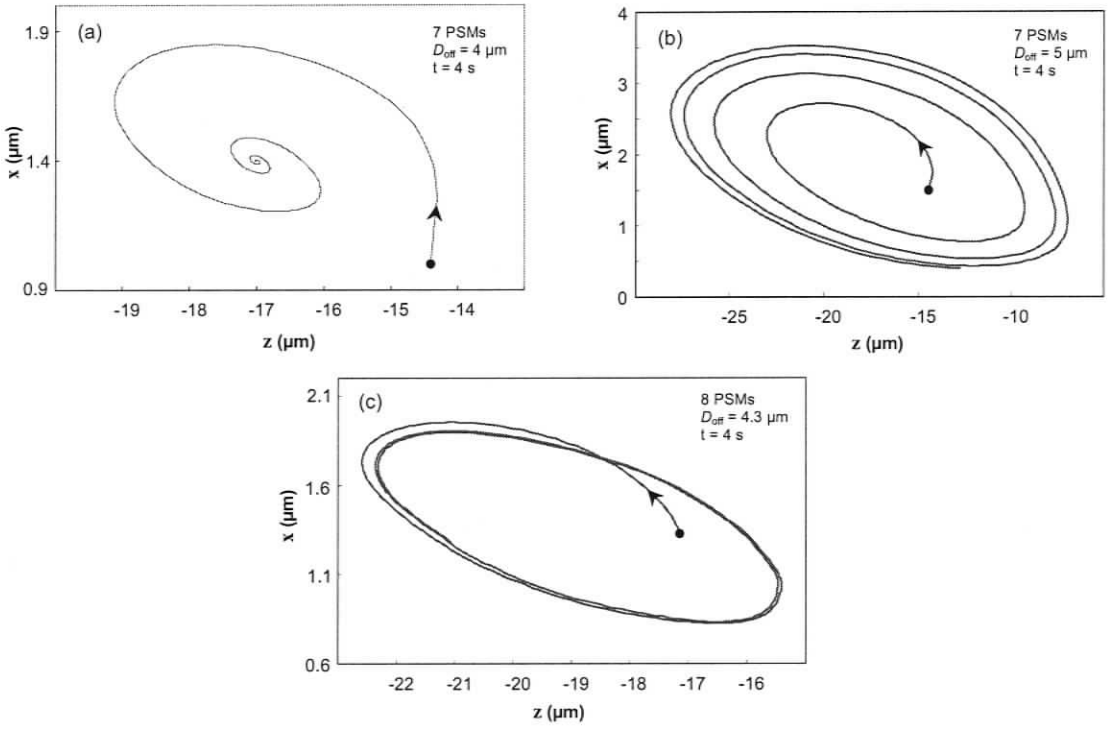

Figure 29 Theoretical trajectory in the x-z plane of the outermost PSM in an array of particles. The initial particle position is shown with a dot. (a) Damped oscillation as the outer PSM of a 7-particle array approaches stable equilibrium for a 4 μm x-offset between the optical beams [14]. (b) Self-sustained oscillation as the particle approaches a stable oscillating limit cycle for a 5 μm offset with 7 PSMs. (c) Self-sustained oscillation for an offset of 4.3 μm with 8 PSMs [14].

Figure 29(c) shows the x-z trajectory of the outermost particle for the case of 8 PSMs when the offset is 4.3 μm. This was near the critical offset required to observe self-sustained oscillations for 8 PSMs. The amplitude of oscillation approaches a stable limit cycle, with a z-direction amplitude of 7.1 μm and x-direction amplitude of 1.1 μm. This agrees well with the observed dynamics of Figure 25(b), to within experimental error. For larger fiber-offsets, the amplitude of oscillation increased and less particles were required to reach sustained oscillation.

Inter-particle hydrodynamic interactions (HDI) are considered for oscillating arrays because the movement of one particle will impart a Stokes' drag force onto adjacent particles. This drag force is due to the particle displacing fluid onto adjacent particles in its path. The position of each particle in the array is therefore based on the subsequent movement of neighbouring particles. For stationary PSMs, HDI does not affect the final equilibrium positions because the effects of hydrodynamic coupling decay very rapidly with a relaxation time on the order of 100 ms [86, 110]. For particles in motion, however, HDI acts to alter neighbouring inter-particle separation (*i.e.* r_{ij} in Eq. (A.12)) and velocity ($d\mathrm{R}_i/dt$). The effective strength of hydrodynamic coupling is inversely proportional to the particle spacing as seen by the Oseen tensor in Eq. (A. 12) [111]. A time delay on the order of 1 ms exists before hydrodynamic coupling reaches a maximum and is independent of particle separation [110, 111].

For 13 particles oscillating, it was experimentally measured that the back bus inter-particle spacing (with respect to the direction of motion) to middle bus spacing difference increased by a factor of 2 when compared with the static case. This decrease in spacing difference is attributed to the additive cascading effects of hydrodynamic coupling from moving particles. It was also noticed that the outermost front and back bus inter-particle spacings were no longer symmetric for moving particles, as for the static case of Figure 26(a). The front bus spacing was 2 μm smaller than for the back bus spacing. This effect is clearly visible in the oscillating array frames of Figure 24(c). The strength of hydrodynamic interaction can be estimated by carrying out a 1-dimensional summation of Eq. (A.11) for 13 PSMs, whereby further up-bus particle velocities increase due to cascaded hydrodynamic coupling. With an average inter-particle spacing of 5.8 μm, the excess force from HDI was calculated to be 0.04 pN, 0.09 pN, and 0.11 pN for the second

to last, middle and front PSMs, respectively. Experimentally, there was also a noticeable increase in front and middle particles velocities compared with those in the back.

Here an opto-hydrodynamic theory is used to explain why the self-sustained oscillations emerge spontaneously for a critical number of PSMs. Particle trajectories at various fiber offsets, D_{off}, and particle numbers, I, were fitted to the damping relation $A\cos(\Omega t)\exp(-\Lambda t)+B$, where Ω is the frequency and Λ is the damping coefficient. It was found that the damping rate decreases as the number of PSMs increase, as shown in Figure 30(a). Results with and without hydrodynamic interaction are included for reference. For a critical threshold in the number of PSMs, the damping goes to zero and then becomes negative, which corresponds to amplification. For an increasing number of particles, the length of the particle chain increases and the edge particles are drawn in by the gradient forces of the respective fiber, whereby oscillation occurs as the array can no longer maintain a linear orientation. Consequently, self-sustained oscillations arise spontaneously for a critical number of PSMs. With the inclusion of HDI, viscous coupling due to collective drag forces from many PSMs acts to increase the damping motion of the system. In the initial experiments, the critical particle number was 13 PSMs (Figure 24(c)), which corresponds to an offset of less than 0.5 μm in the theory. The critical number of PSMs to observe oscillation is dependent on the offset between the beams. Greater offsets produce oscillations for a smaller number of PSMs. Damping reduces with offset increase because an even greater breaking of array linearity occurs and a stable equilibrium position will not exist for arrays greater than a critical length.

In the present system, inertia is effectively damped out immediately and so there is no kinetic energy contribution to the dynamics. The origin of self-sustained oscillations in a viscously over-damped media can be explained by considering the different components of the optical force acting on each particle. In Figure 25(b) and Figure 29(c), the z-displacement corresponds to varying the potential energy of the particle due to the optical scattering force [32]. Similarly, the x-displacement corresponds to varying the potential of a particle due to the optical gradient potential, which increases with increasing distance from the beam centre [32]. This allows for an interpretation of the observed oscillations: the potential energy is exchanged between the optical scattering potential and optical gradient potential to move the particle in an orbit in the x-z plane. The perturbation in the

electromagnetic field by each particle influences the force on its neighbours. This pushes the particles transverse to the beam axis; thereby, the axial scattering potential is translated into a transverse gradient potential. This is fundamentally different from other coupled-particle systems where inertia plays an important role [90]; in those systems there is an exchange between the potential and the kinetic energies. Here, the usual kinetic energy contribution is replaced by the gradient potential of the optical trap. It is clear from the opto-hydrodynamic theory that transverse symmetry breaking is required to produce the observed self-sustaining oscillations. The symmetry breaking allows for the coupling exchange between the scattering potential and the gradient potential, as mediated through optical interaction.

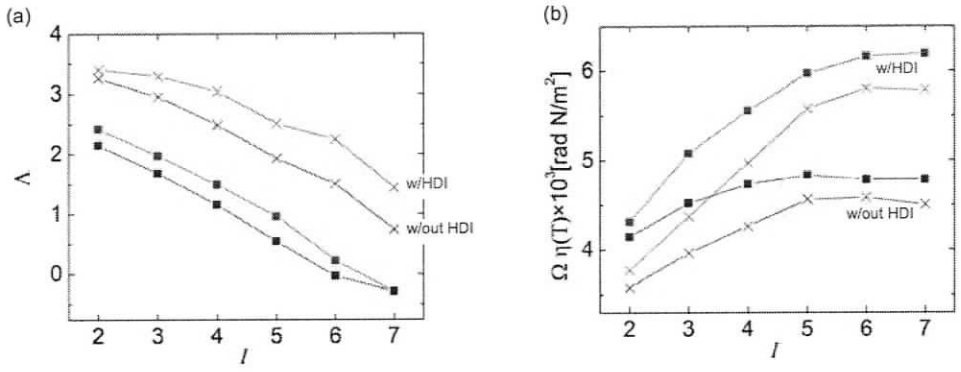

Figure 30 Damping and oscillation frequency as a function of a number of the particles, I, for various offsets, D_{off}. Squares (■) and crosses (×) represent results for D_{off} = 5 μm and 4 μm, respectively; Red and blue lines represent results with and without HDI, respectively [15]. (a) Damping coefficient Λ. (b) Frequency Ω.

Figure 30(b) shows the dependency of angular oscillation frequency on the number of particles, fiber offset, and on hydrodynamic interactions. The frequency of oscillation increased with an increase in the number of PSMs in the array. For example, in going from 4 to 5 PSMs for the same offset, the oscillation frequency increased by 10%, but a damped trajectory towards a final stationary position was still observed. After reaching the critical number of PSMs for sustained oscillation, in this case 7 PSMs, the frequency decreased by 10% when transitioning from 7 to 8 PSMs. This can be understood by considering that the total particle velocity increases due to the summation of synchronous drag forces induced by adjacent particle motion, as in Eq. (A.11). With increased particle

velocity, the array will change direction in less time as compared to the situation without HDI, thereby yielding a higher oscillation frequency. The oscillation frequency also increased as the transverse offset was increased. For example, in going from a 4 μm offset to a 5 μm offset for 7 PSMs, the oscillation frequency increased by 10%. By artificially removing the hydrodynamic interactions (by setting the second term of Eq. A.12 to zero) it was found that both the oscillation frequency and the damping rate decreased. For example, for the 7 PSM case with a 4 μm offset between the fibers, the oscillation frequency decreased by 20% and the damping rate decreased by 50% when removing the hydrodynamic interactions. The hydrodynamic interactions are not required to observe oscillation.

The experimentally observed oscillation frequency was approximately 2 Hz (for both the 13 PSM and 8 PSM oscillation conditions). The same oscillation frequency for an 8-particle array was obtained from the simulation given the viscosity of water at 60 °C. While an exact temperature measurement within the microfluidic system was not obtained, temperatures in this range are expected due to optically-induced heating of the relatively small liquid volume. The dominance of thermal diffusion at small length-scales results in negligible temperature variations on the scale of the PSMs, and precludes local thermal convection effects. It is possible, however, to get significant heating in the larger fluid volume over time and localized boiling, for instance, has been observed. While both the lateral offset and temperature contain uncertainty in the experiments, the main features of the experiment are captured within the opto-hydrodynamic theory.

In the above examples, the offset was set greater than the experimental tolerances to observe oscillations for a small number of particles, since the calculation time for many particles is prohibitive for the current single-processor implementation of the numerical model. Although systematic studies of greater than 7 particles have not yet been performed, the base mechanism presented here concludes that the occurrence of spontaneous oscillation is the result of asymmetry, for example, from misalignment of the beam axes.

6.5 Summary

Regularly spaced array-style trapping was observed for configurations containing 1 μm PSMs and a trapping wavelength of 980 nm. This regime of trapping is distinct from arrangements containing 2 μm spheres, which formed stacked particle configurations. The occurrence of spontaneous oscillation was observed experimentally for both a fiber offset and a particle number dependency. Inhomogeneous inter-particle spacing was observed for increasing distance from the array centre and as the number of particles increased. An opto-hydrodynamic theory was adopted to describe the dynamics of optical interaction of dielectric polystyrene microspheres in a dual-fiber system and was found to agree well with experimental observations. The simulations, which incorporate hydrodynamic interactions between particles, naturally reproduce the inhomogeneous self-organization and the spontaneous onset of self-sustained oscillations of particles, both of which agree qualitatively and quantitatively with the experiments. Two types of inhomogeneous properties in equilibrium spacing were shown for a trapped particle array; one is that, for a fixed *I*-particle array, the inner inter-particle spacing is smaller than the outer spacing, and the other is a nonlinear decrease in the averaged equilibrium spacing as the number of trapped particles increases. The origin of the inhomogeneous spacing is found to arise from enhanced optical interaction in the presence of forward Mie scattering. The self-sustained oscillations arise spontaneously once a critical number of particles is reached, where the optical gradient force takes over the usual role of kinetic energy. It was shown that a transverse misalignment of beam axes is the mechanism responsible for spontaneous self-sustained oscillation in the dual-beam trap.

CHAPTER 7

CONCLUSIONS

7.1 CONTRIBUTIONS

A variety of particle trapping capabilities were developed through the planar integration of optics and fluid dynamics to actively control particle dynamics in an optofluidic lab-on-chip. A low cost method was adopted for the integration of high power fiber optics directly into a microfluidic environment and a variety of optofluidic trap configurations were demonstrated using video microscopy and streak imaging. Selective control of optical orientation, beam characteristics, power, and flow rate enabled a broad range of innovative functionality. Increasing the flow rate in an angularly biased trap, for example, permitted a previously stable particle trap to become circular and can be extended to enable the rotation of trapped specimens or to applications requiring microfluidic mixing in a localized environment. Single upstream-oriented fiber configurations in a defined size regime permitted the formation of optically and hydrodynamically coupled arrays of numerous particles and may lead to methods for large-scale cell confinement used in bio-analysis or for particle counting through optical feedback. Single- and multi-particle trapping was established in systems containing an upstream-oriented lensed fiber and precise axial position control was possible through optical intensity and flow rate manipulation. The knowledge of a trapped particle's position in a given flow could be used to design new devices for flow rate monitoring and calibration. Discrete particle waveguiding and trapping was observed in systems where light was oriented against flow and may offer a system of optofluidic waveguiding which is distinct from established methods, such as solid-core/liquid-cladding and liquid-core/liquid-cladding waveguides. The work on flow-dependent trapping was well-received at three highly regarded conferences, CLEO 2007, APS 2007, and CLEO 2008,

and the majority of these efforts has been published simultaneously in *Lab on a Chip* [13].

A defined regime of trapping was observed for trapping wavelengths approximately equal to the particle size and lead to the formation of regularly spaced particle arrays. The occurrence of spontaneous oscillation was observed for both a fiber offset and a particle number dependency. Inhomogeneous inter-particle spacing was observed for both a fixed particle number and as the number of particles increased. Specifically, the separation between inner particle pairs was smaller than that for outer particle pairs for a fixed number of particles, and the average inter-particle spacing decreased nonlinearly as the number of trapped particles increased. An opto-hydrodynamic theory was presented to describe the dynamics of optical interaction of dielectric polystyrene microspheres in a dual-fiber system and was found to agree well with experimental observations. The self-sustained oscillations arise spontaneously once a critical number of particles is reached, where the optical gradient force takes over the usual role of kinetic energy and a transverse misalignment of beam axes was the mechanism responsible for spontaneous self-sustained oscillation in the dual-beam trap. The majority of this work was also recently published in *Physical Review B* [14] and *Optics Express* [15] and conference contributions included *OMEMS* 2007 and *CLEO* 2008.

7.2 Outlook

The experimental setup employed in this work is attractive from the perspective of being robust, cost-effective, and dimensionally small. For the fiber-integrated lab-on-chip to be widely exploited commercially, enhancements may be required, thereby increasing on-demand functionality. On-chip piezoelectric actuators can be directly integrated into a sealed fiber channel to enable voltage-controlled fiber alignment and reorientation. I recently presented a proof of concept design in a graduate MEMS course which demonstrated maximum obtainable fiber displacements of ~5 μm for 150 μm thick integrated PZT-5A plate actuators. For ease of connection to various laser sources outside the laboratory setting, on-chip connectorized fiber fittings can be PDMS sealed directly into the micro-channels. This would also simplify the disposability of the chip

unit after use. Alternately, chip thicknesses and fluid volumes can be further reduced by fabricating a fiber housing independent of a thinner sample chamber, by incorporating etched optical fibers, or through the integration of on-chip optical waveguides, such as those demonstrated for on-chip PDMS waveguides, where the core/cladding structure contained a step in PDMS refractive index [112]. On-chip waveguides such as this may find application in complex optical trapping networks.

To extend the emphasis of the current work to the biological community, future directions should include trapping of biological specimens. Angularly biasing with regard to the flow-dependent work, for example, would benefit from experiments involving the reorientation of non-spherical micro-organisms. A characterization of rotational speed vs. the power-to-flow ratio would also be an asset. Localized mixing times for the scheme depicted in Figure 13 would be of interest and selective on/off laser strategies may be useful for creating pockets of mixed analyte downstream. The demonstration of discrete-particle waveguiding would benefit from an FDTD, or other type simulation, characterizing ideal particle spacing for enhanced waveguiding. Experiments demonstrating optical loss as a function of particle number, or maximum particle numbers achievable in a given flow, would additionally be desirable. Investigations involving dual-beam particle arrays may be extended to include an offset vs. particle number criterion for the occurrence of spontaneous oscillation. At a fundamental level, this knowledge would offer insight as to alignment offset, where more particles required for spontaneous oscillation would indicate improved fiber alignment. Such a demonstration may prove beneficial for configurations containing an integrated piezoelectric alignment scheme.

The following chapter titled, *Avenues for Exploration,* characterizes a few recent discoveries in experiments containing dissimilar trapping wavelengths, immiscible 2- and 3-phase systems, and thermal gradients. Many of the effects contained in this chapter are not entirely understood and are provided at this stage for academic curiosity.

CHAPTER 8

AVENUES FOR EXPLORATION

In this chapter, experimentally observed effects of optically induced joule heating in a PDMS microfluidic environment are discussed and characterized. Prolonged high power optical delivery into the host fluid was found to induce gas phase formation and affected the stability of trapping positions. The development of immiscible water-in-oil systems are discussed and opto-thermal activation of micro-spheres in a two-phase system were observed. Lastly, optical-particle self-trapping is demonstrated with a tapered fiber and distinct oscillation and circulatory behaviour are observed in trapping configurations containing different wavelength fibers.

8.1 MULTIPLE WAVELENGTHS

8.1.1 Power-dependent Oscillation

In this section, the results of experiments containing counter-propagating 980 nm and 1550 nm laser light are considered. Figure 31(a) shows a method of motion control that is similar to that demonstrated for a single particle (Figure 10), however interesting dynamics were observed when particles were trapped at specific inter-fiber positions. The power of the 980 nm fiber was varied while the power of the 1550 nm fiber was held constant at 54 mW. The transverse and lateral offset between the fibers was 3 μm and 140 μm, respectively and flow was not visible between the fibers. The assembly of three 9 μm particles shown in Figure 31(a) was initially stably trapped at a distance of 17.4 μm from the facet of the 980 nm fiber and translated axially to a position of 82.6 μm, where it remained trapped in position with an output power of 41.7 mW. Increasing the power further resulted in oscillation of the 3 PSM assembly, and is observed by the central oscillating region in Figure 31(a), and by the area of solid gray shading in Figure 31(b).

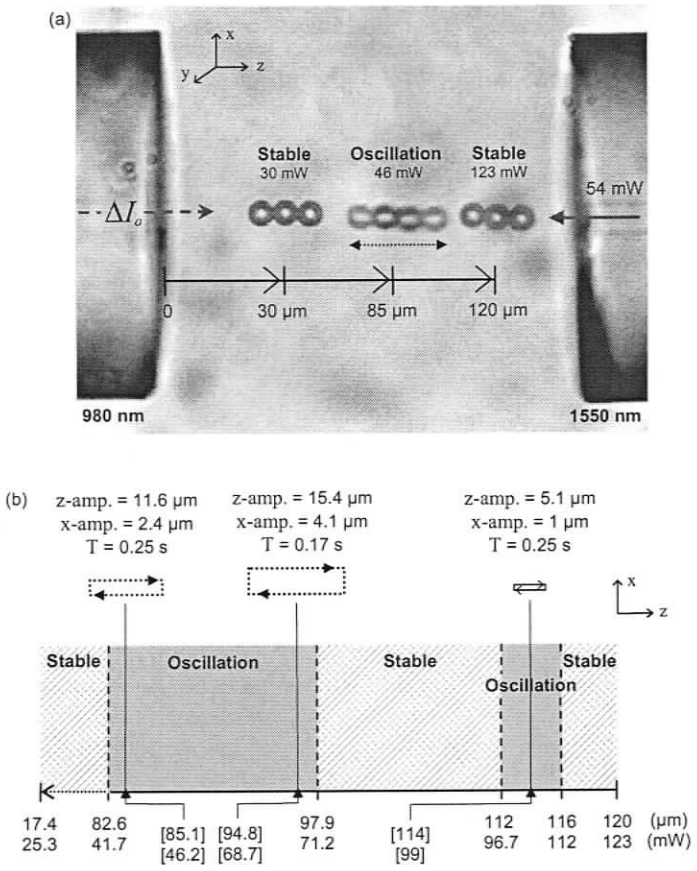

Figure 31 (a) Four superimposed images demonstrating power-dependent oscillation for a particular region of trapping (46 mW), while stable for other regions. (b) Regions of stable trapping and oscillation as a function of distance from the 980 nm fiber and output power. Dashed trajectories within these regions are drawn to the indicated scale. Employed PSM diameters are 9 μm.

Two positions extending the first oscillation region were characterized. Oscillation occurring at the beginning of this region (85.1 μm, 46.2 mW) had a z- and x-direction amplitude of 11.6 μm and 2.4 μm, respectively, and an oscillation period of 0.25 s. Oscillation occurring at the end of the oscillation region (94.8 μm, 68.7 mW) had increased amplitudes of 15.4 μm and 4.1 μm in the z- and x-directions, respectively, and the period of oscillation was 0.17 s. Various regions of stability and oscillation are shown in Figure 31(b). The distance and power scale shown are with respect to the 980 nm fiber and rectangular lines with arrows indicate particle trajectories, to-scale, measured with respect to the centre particle. The width of the oscillation and stable

regions decreased noticeably with increasing proximity to the 1550 nm fiber and the oscillation amplitudes decreased by a factor of 3 in the 2nd oscillation region. When optical power was then reduced from the furthest extent of trapping (123 mW), oscillation and stability regions occurred at approximately the same locations reported previously. The process showed repeatability for several trials. The right most stable region shown in Figure 31(b) was limited to the maximum output power of the 980 nm fiber and trapping proximity to the facet of the 1550 nm fiber. Dynamic ranges for the 2nd and 3rd stable regions were 65 μm and 14 μm, respectively, and 15 μm and 4 μm for the 1st and 2nd oscillation regions, respectively.

With radially offset beams (~1 μm), an axial dependence on oscillation may be a result of the particle interfering with the spatial region of a higher order mode, for example an LP_{11} mode, where the particle beats between the LP_{01} and LP_{11} modes of the 980 nm fiber and the LP_{01} mode of the 1550 nm fiber. The existence of these higher order modes is due to operating the 980 nm laser diode in a fiber below the cut-off wavelength for single mode (LP_{01}) operation (LP_{01} is simply two orthogonal components of the linearly polarized HE_{11} mode), being approximately 1450 nm in the 1550 nm fiber. Similarly, a power dependence on oscillation may be caused by a destabilization in optical intensity due to increasing significance of higher order modes at larger injection currents. Oscillation trajectories and periods were similar to those observed for 13 PSM arrays as in Figure 25, however the theoretical existence for regions of stability and instability are not entirely understood and may be influenced by unexpected standing wave effects, thermal gradients across relatively large particles, or the specific alignment and configuration.

8.1.2 Continuous Circulator

When the fiber offset for the configuration described by Figure 31 was increased to ~5 μm, the particle assembly transitioned into a circulatory mode at output powers near the critical onset of oscillation (42.7 mW). Figure 32 shows 6 overlaid images demonstrating continuous circulation of an assembly of three, 9 μm PSMs. The assembly was observed to circulate continuously for over 2 minutes. The particles in the top half of the circulation had a velocity, v_{top}, of 100 μm/s, as influenced by the scattering force

from the 980 nm fiber due to the specific fiber offset, and the bottom half had a velocity of 300 μm/s and was influenced by the 1550 nm fiber. The factor of 3 increase in particle velocity may be due to the 1550 nm fiber operating at 25% higher power, the effects of thermal gradients imposed by 1550 nm light, or by an increase in radiation pressure cross-section associated with this wavelength. The latter two of these effects are discussed further in §8.2 and §8.3. The overall period of oscillation was 1.2 s and the z- and x-direction amplitudes were 85 μm and 5 μm, respectively. The slight tilting observed in Figure 32 near the fiber facets is due to optical gradient forces pulling the outer most particle into the axis of the opposing fiber.

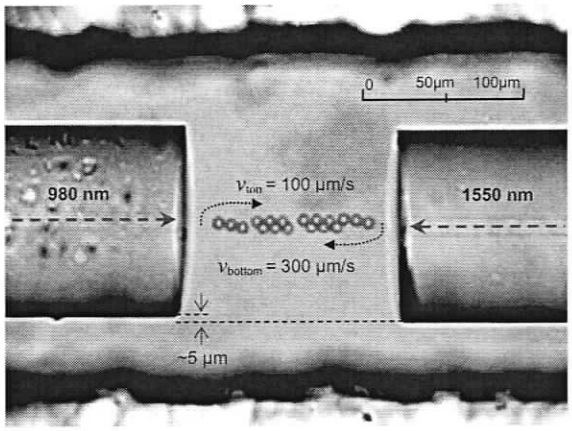

Figure 32 Six overlaid images demonstrating a three-particle assembly of 9 um PSMs undergoing continuous circulation.

8.1.3 Active Particle Storage

For the same 5 μm fiber offset and seven, 9 μm PSMs, selective on/off switching of opposite fibers was found to enable particle storage on the opposing fiber facet. Figure 33 shows this effect, where in (a) Fiber 2 is held on and Fiber 1 is off and the particles are maintained on the facet of Fiber 1. When Fiber 2 is switched off and Fiber 1 is switched on, the particles transition to the opposite facet as shown in Figure 33(b). Figure 33 (c) shows the particles being held on the facet of Fiber 2. The switching process was repeated in Figure 33(d)-(e). The switching time was limited by the on/off cycle time of the laser diodes (3-4 s) and by particle rearrangement and transfer (6-8 s). The output

power of both fibers was fixed at ~50 mW. The total switching time for all particles to transition from one fiber to the next was ~10 s. This cycle was repeated continuously for 5 cycles, where the maximum holding time experimented with was 30 s and the minimum achievable was 4 s.

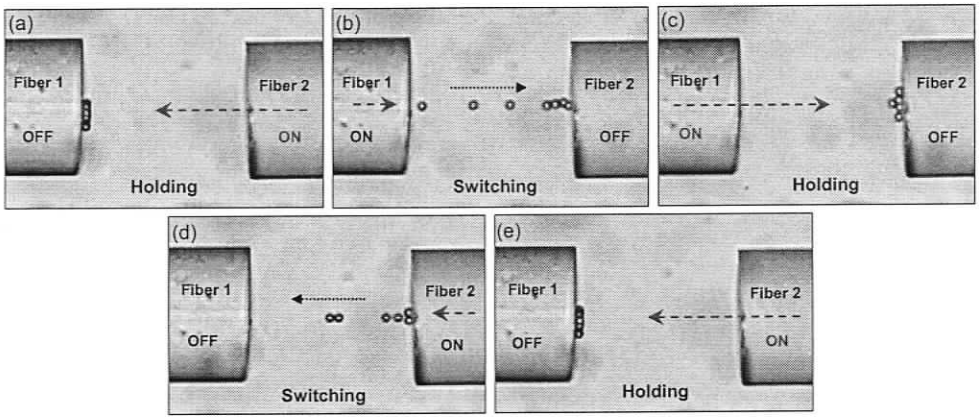

Figure 33 Particle transitioning and holding between opposing fiber facets by actively switching on or off the respective fiber.

8.1.4 Polarization-dependent Oscillation

A polarization dependence was also observed for the situation described in Figure 31. Changing the state of polarization in the 1550 nm fiber by means of an externally connected Fiber Polarization Controller (FPC) allowed for induced particle oscillation within the 2nd stable region of Figure 31(b). An FPC contains three paddles of set radius with looped fiber around the paddles and can be rotated from -120° to +120° degrees (0° being vertical). The rotation of the paddles, which twists the fiber, induces birefringence within the fiber's silica. Birefringence is a degeneracy between the two fundamental orthogonally polarized modes inside the fiber and is determined by the difference between their effective refractive indices. Birefringence occurs due to variations in the core shape (not perfectly circular), external anisotropic stress acting on the core, and variations in the refractive-index profile. The 1st and 3rd paddles contain one fiber loop and act as a quarter wave plate while the middle paddle contains two loops and acts as a half wave plate. A quarter wave plate converts linearly polarized light into circularly polarized light and circularly polarized light into linearly polarized light. A half wave

plate converts linearly polarized light into linearly polarized light with the plane of polarization rotated by 90°, and right/left circularly polarized light into left/right circularly polarized light. A quarter wave plate also delays the phase between two orthogonal polarizations, E_x and E_y, by $\pi/4$ and a half-wave plate by $\pi/2$.

The FPC, which is designated to work with single-mode 1550 nm fibers, was initially verified with a polarizer and power meter to ensure proper functionality. With all three paddles initially vertical [0°, 0°, 0°] and Fibers 1 and 2 at 35.5 mW and 54 mW, respectively, the three 9 μm PSMs were stably trapped within the stable region as indicated in Figure 31(b). Particle oscillation occurred in a fashion analogous to the oscillation regions of Figure 31(b) when the FPC paddles were at positions [+120°, +120°, -120° thru 0°], [+120°, +120° thru 0°, 0°], and [+120° thru +5°, 0°, 0°]. Stable trapping occurred again when the first paddle was rotated from +5° back to 0°, for final paddle positions of [0°, 0°, 0°]. When the paddles were at [+120°, +120°, -120°], for example, the z- and x-direction amplitudes were 3.0 μm and 1.1 μm, respectively. When paddles were at [+120°, 0°, 0°], the z- and x-direction amplitudes were 4.6 μm and 0.5 μm, respectively. Generally, reflected, scattered, and absorbed light at boundaries is polarization sensitive [47] and the occurrence of polarization-dependent oscillation is likely due to the effects of polarization on optical force, in particular a dependence on trapping efficiency [113, 114]. Variations in the trapping force induced by the FPC on the 1550 nm fiber effectively alters the equilibrium state of the particle, thereby transitioning the PSM in or out of the oscillation/stable regions shown in Figure 31(b). The introduction of angular momentum from circularly polarized light may also induce oscillation of the assembly as a whole due to its non-spherical symmetry [102], especially near a transition region. Additionally, distinct counter-propagating spatial intensity distributions may interfere such that more than one equilibrium position exists (as with weakly guided LP_{11} modes [97]), whereby a trapped particle may oscillate between two such equilibrium positions.

8.1.5 3-Dimensional Rotator

Figure 34(a) shows a configuration of five 9 μm PSMs undergoing 3-dimensional counter-clockwise rotation in y-z plane. The particles are bound optically and in physical contact, however were free to move with respect to one another while maintaining

contact. It was observed that the position of the top centre particle was fixed with respect to rotation and the bottom 4 particles rotated in the y-z plane, however displacements in the x-direction were also observed. The direction of rotation was initially counter clockwise (CCW) and spanned a linear distance of 17 μm in the z-direction as shown in Figure 34(a). Once the particle configuration completed a full rotation, that is, having spun CCW while translating 17 μm in the -z-direction and then back 17 μm in the +z-direction, it rotated in place in the clockwise (CW) direction as indicated in Figure 34(b). The period of rotation for a complete cycle was 0.5 s.

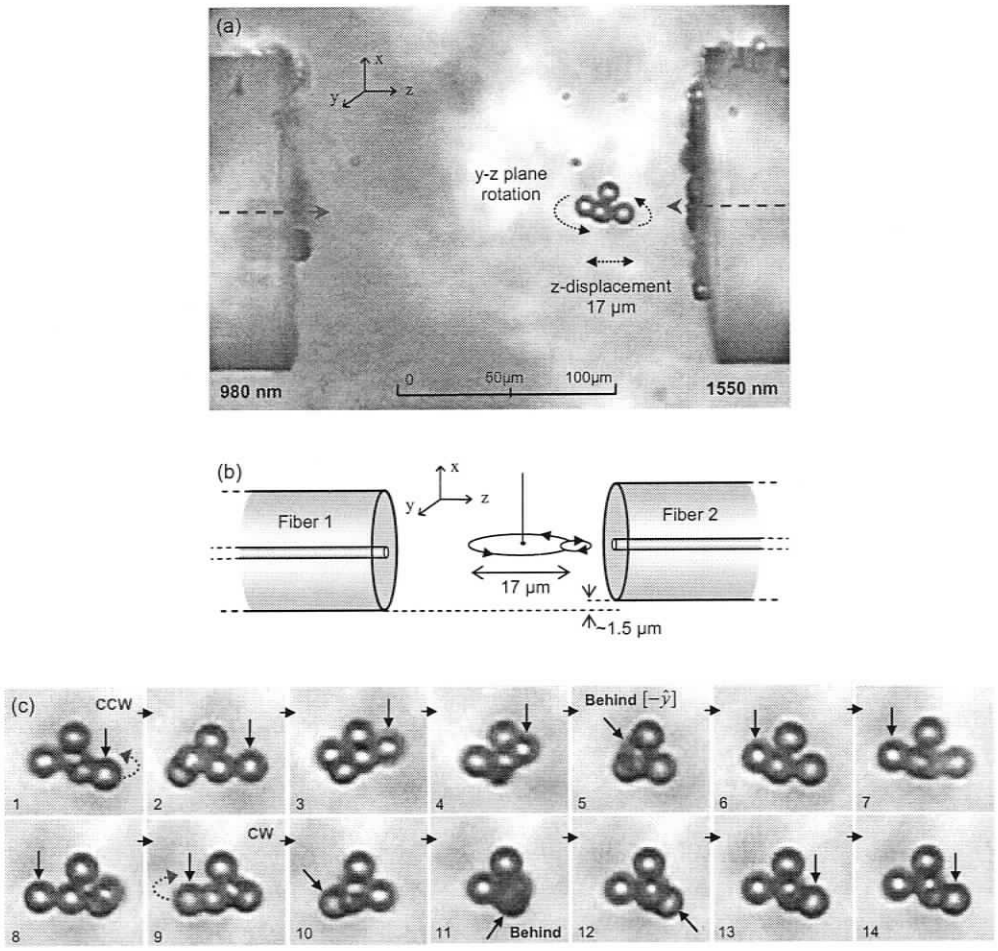

Figure 34 (a) Assembly of five 9 μm particles rotating in three dimensions. (b) Direction of rotation as it switches from counter-clockwise to clockwise during one cycle. (c) Relative dynamics of sphere rotation demonstrating back-and-forth rotation.

Figure 34(c) shows 14 frames from a complete cycle where a select particle is tracked as indicted by the vertical arrows. Frames 1 – 8 show a select particle as it rotates CCW behind the centre particles (the assembly as a whole is also being displaced 17 μm in $\hat{z}$) and frames 9 – 14 show the same particle as it rotates CW behind the centre particles (no $\hat{z}$ displacement).

The counter-clockwise rotation and z-direction displacement can be understood in a manner similar to that described for single particle circulation (Figure 12) provided that a y-direction offset exists between the fibers. An offset in this direction was not directly measureable, however it is a valid assumption considering uncertainties in chip fabrication thicknesses. Positional shifts in the x-direction are explained by an x-direction fiber offset of 1.5 μm, however the in-place CW rotation observed remains an open question. Left and right fibers were operated at 980 nm and 1550 nm, respectively and emit at ~50 mW. The distance between fibers was 170 μm and flow in the channel was negligible. The total observed continuous rotation time was 90 s, and was limited due to the gradual formation of a gas phase inside the channel (refer to §8.2). Several instances of the 14-frame series were compared throughout the 90 s duration and particle positions and orientations were found to be nearly identical throughout.

8.2 Optical Heating

With prolonged use, light radiation from embedded fiber optics in water had the tendency to vaporize water molecules, leaving undesired bubbles in the trapping channels. The main disadvantage of using PDMS in the present work is that it is gas permeable, allowing this gas phase to seep through the PDMS into the ambient environment. The effect of localized boiling was noticeably more pronounced when the trapping wavelength was 1550 nm compared with 980 nm and the increased occurrence of gas formation discouraged continued development at 1550 nm. Gas phases were not initially observed when the 1550 nm laser was switched on, however formation occurred between 1-5 minutes of laser on-time. The size of the gas bubble observed in Figure 10(a) had an average diameter of 94 um which increased by ~17% during the course of 50 s. Growth of the gas phase ceased immediately once the 1550 nm laser was switched off (980 nm

still on). The occurrence of gas phases also occurred with 980 nm sources, however, only after ~15 minutes of on-time. Particle fluctuations occurred when transitioning the particle along the z-axis in Figure 10(a). These positional fluctuations may be due to the existence of thermal gradients along the beam axis of the 1550 nm fiber or possibly due to conflicting gradient forces from two fibers not in absolute alignment.

Figure 35 shows a three fiber implementation, where the two vertical 980 nm fibers are used to stably trap a 9 μm particle and the angled 1550 nm fiber induced gas formation in close proximity to the trapping position. The gas phase shown here was initially absent and appeared after ~5 minutes of laser on-time. Gas phase formation was not observed on opposing ends of the 980 nm fibers. Before the appearance of the gas phase, the particle was stably trapped, however fluctuations in the equilibrium position occurred in the vertical direction once the gas phase reached the size shown in Figure 35 (average diameter of 86 μm).

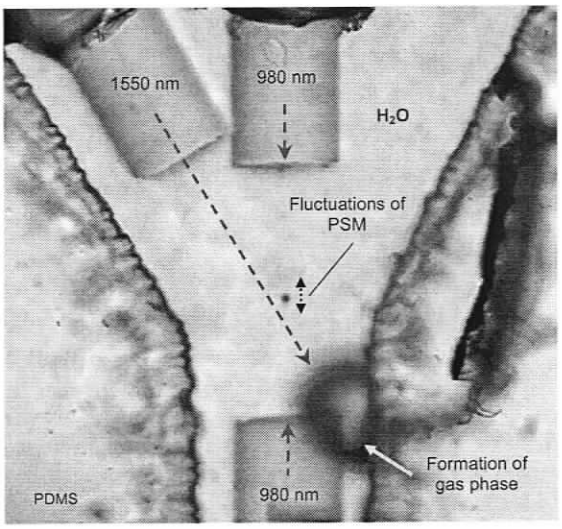

Figure 35 Laser induced boiling and trapping fluctuations from the 1550 nm laser. The two 980 nm fiber lasers are used to trap the particle while the angled 1550 nm fiber induces gas phase formation and vertical fluctuations of the PSM in water.

The measured oscillation amplitude varied from 7 μm – 17 μm and the period of oscillation varied between 0.2 s – 0.4 s. The oscillation amplitude increased over time, particularly as the gas phase rapidly enlarged, *i.e.* from an average in-plane diameter of 86 μm to 127 μm over 14 s. The growth of the gas phase and the observed positional

fluctuations are consistent with that found in Figure 10 for a 1550 nm source. Again, positional fluctuations are likely due to the presence of temperature gradients near the gas-water interface or the occurrence of localized flows induced by gas expansion.

The increased occurrence of localized boiling associated with 1550 nm fibers may be due to a two-fold increase in the Lambert absorption coefficient in water at a wavelength of 1550 nm compared to 980 nm [115]. As an example, the expected localized increase in temperature across a 10 μm diameter sample volume at 980 nm was measured to be approximately 5.1 °C for every 100 mW of laser power entering the sample and 10.2 °C/100 mW at 1550 nm [96]. The time-dependent effects within a glass micro-chamber have been reported and indicate a minimal temperature change of 0.03 °C/s at ~980 nm for the first 10 s [116-118] (after initial temperature increase, ~1 ms), however long-term temperature change will also be determined by the rate of heat dissipation. It was observed in the experiments that chips with a PDMS channel structure sealed directly to glass had a decreased occurrence of gas formation as compared to chips with a PDMS-PDMS seal. This is likely due to an order of magnitude increase in the thermal conductivity of glass over PDMS, *e.g.* 0.2 W/m-K for PDMS [93] and 1.4-1.7 W/m-K for glass [119], and the thickness of the PDMS. The time-dependent effects of temperature in an all-PDMS chamber are therefore expected to be greater than in the case reported for an all-glass chamber due to the insulating properties of PDMS. Future work may include the use of Rhodamine B dye to accurately measure the temperature profile in the microfluidic channels [108]. The fluorescence intensity of Rhodamine B is strongly dependent on its temperature in the range of 0 °C to 100 °C and can be calibrated and mapped out using a coupled CCD camera.

For increased environment temperatures, improved temperature estimates become important as temperature affects optical force calculations inasmuch as the refractive index of both polystyrene and water are influenced by temperature (thermal gradients and absorption also influence the total force). For a temperature shift from 20 °C to 99 °C, for example, the refractive index of polystyrene spheres will increase by 0.015 [120] and the refractive index of water at 1 atm will decrease by 0.01 [121], leading to an overall increase in imparted optical scattering force of ~20% as determined by Eq. (2.1) for

1-9 μm PSMs. Similarly, a decrease in fluid viscosity with increasing temperature, *e.g.* from 20 °C to 100 °C, reduces the estimated Stokes' drag by a factor of ~3.4 [122].

8.3 Immiscible Systems

Multiphase flows have been the subject of recent interest for microfluidic lab-on-chip devices due to reduced axial dispersion and enhanced mixing, and are of general interest to studying chemical reactions [123]. At the interface between two immiscible fluids, water-in-oil for example, an interfacial tension exists which is dependent on temperature, surfactant concentration and electrostatic potential [6]. Surfactant molecules in fluids typically contain a hydrophilic head immersed in an aqueous solution and an external hydrophobic tail [124]. The presence of surfactant therefore creates infinitesimal concentration fluctuations at the immiscible fluid boundary and adds to the overall surface tension. Surface tension gradients create motion within the bulk fluid at the fluid-fluid interface in a process known as thermocapillary, or Marangoni, flow. This effect is particularly pronounced at microscales where surface tension forces dominate inertial forces due to the large surface area to volume ratio. The fluid-fluid interface experiences a shear stress (force) in the direction of increasing surface tension, thereby inducing motion of the adjacent fluid [125]. The effect of heat reduces surface tension because of thermal expansion and can drive droplets towards colder regions to minimize their interfacial area and total surface energy [126].

Gas bubble [127] and oil [128, 129] migrations have been observed using embedded microheaters and laser induced heating has been used to transition aqueous droplets (30 μm to 1.5 mm in diameter) at speeds up to 3 mm/s, where opposite facets of the droplet experienced a 10 °C temperature variance [126]. Optical manipulation of microscale liquid films have also been demonstrated [130] and optical heating has been used to hinder droplet formation at a T-junction and actively fuse aqueous droplets [131]. Thermal droplet fusing has been shown to enable spontaneous mixing caused by the fusion process, and not by diffusion [126]. Similarly, the effects of surface tension can drive recirculating cellular flows in a fluid layer and is caused by regions of heating and cooling [132]. This effect is known as generally as Marangoni convection and the

tendency of an interfacial fluid to convect is given by the Marangoni number, which characterizes variations in surface tension with temperature. Further detail on the Marangoni number can be found elsewhere [124, 132, 133].

Figure 36 shows two immiscible liquid regions, one containing Perfluorodecalin (PFD) oil (Acros Organics, Morris Plains, NJ) and Tridecafluoro-1 octanol surfactant (Acros Organics, Morris Plains, NJ), outlined in yellow, and the other containing an aqueous water region with 9 um PSMs in solution, outlined in blue. The optical fiber shown to the right is encompassed in PFD and emits at a wavelength of 980 nm with an output power of 120 mW. The existence of surface tension gradients at the oil-water interface are established primarily by temperature gradients from optical heating and the presence of surfactant in the PFD. When the fiber laser is switched on, clockwise convective flow is observed in the water/PSM phase as indicated by the particle streak imagery of Figure 36. It was observed that inner diameter convective currents had a rotational speed much greater to that of the outer diameter currents by a factor of 5. For example, particles at a distance of 450 μm from the cycle centre had a linear velocity of 130 μm/s, where particles 100 μm from the centre had a velocity of 600 μm/s. The area affected by the convective flow was approximately 700 μm × 700 μm.

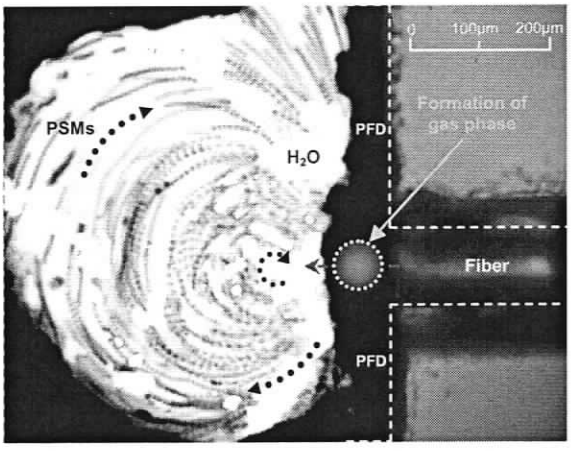

Figure 36 Thermally activated tornado-like particle circulation at a water-oil-gas interface (r_o = 1 μm). Stationary out of plane surface particles have been edited from the image for clarity.

After ~5 s of continuous lasing, gas development occurred at the fiber facet as shown by the dashed circle in Figure 36. When the gas phase reached a diameter of ~60 μm, particle velocities increased to 350 μm/s and 2400 μm/s for distances of 450 μm and 100 μm, respectively, from the cycle centre. This 3-4 factor increase in convective speed may be attributed to larger surface tension coefficients associated with water-gas interfaces as opposed to water-oil interfaces. Thermally induced velocities of this magnitude are consistent with recirculating currents found elsewhere for Marangoni-Benard convective flows [132] and the introduction of surfactant has been observed to increase the intensity of convection [134, 135]. It should be noted that the evaporation of water which formed the gas phase, also increases temperature variations and alters surface tension further. The convective flow shown in Figure 36 also formed a doublet flow pattern when multiple gas phases were present near the fiber facet. High speed recirculating flows may find use in broad area microfluidic mixing applications where the constituents to be mixed are within a single phase.

Figure 37 shows the process used to create water-in-oil droplets within a T-junction geometry, where the employed immiscible fluids are PFD oil and deionized water containing 9 μm PSMs. The inlets of the PFD oil and H_2O channels (not shown) were connected to separate syringes, the flows of which were controlled by a stepper motor. The flow rates set for the PFD oil, Q_o, and water, Q_w, phases were 10 μl/min and 0.70 μl/min, respectively. Figure 37(a) shows the effects of surface tension at the water-oil interface which acts to reduce the interfacial area of the water phase. Viscous stresses induced by the flowing PFD act to drag the water phase downstream. When the surface stresses balance the viscous stresses, the water phase separates, forming a water droplet. The droplet transitions downstream with the flowing PFD as shown in Figure 37(b). Figure 37(c) shows the final droplet at a point where it has reached a PDMS reservoir with dimensions 1 mm wide by 250 μm tall. The diameter of the droplet shown is ~330 μm, indicating contact with upper and lower PDMS faces. Increasing Q_o/Q_w was found to decrease droplet size, however the current configuration, particularly the channel height, limited the droplet size to ~330 μm.

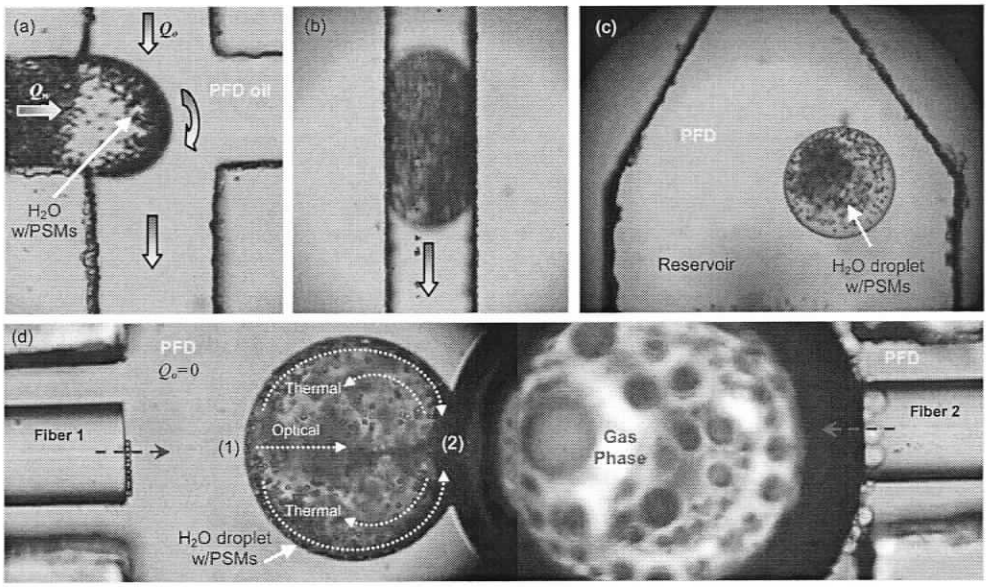

Figure 37 Sphere filled water droplet formation (a)-(c) and optically/thermally induced inner-droplet particle circulation (d).

Initially, when the droplet containing PSMs is brought into contact with optical forces (only Fiber 1 is activated), inter-droplet scattering of the PSMs is observed initially in the axial direction, the trajectories of which are indicated by the dashed horizontal line in Figure 37(d). The velocity of particles once transitioning from the water-PFD interface, marked by position (1), were ~90 μm/s and particle velocities along the droplet perimeter were ~5 μm/s in a direction towards (1). When Fiber 2 was turned on, stable trapping inside the droplet was possible, however the presence of a gas phase between the droplet and Fiber 2 developed some time later, as indicated in Figure 37(d). As discussed previously, surface tension imbalances induced by thermal gradients at phase boundaries can induce convective flows, however the change in diameter of the gas phase shown in Figure 37(d) may have also affected the surface characteristics at (2). Rapid circulation of inner-droplet flows were observed after formation of the gas phase, the directions of which are indicated by the dashed lines. The inner and outer radial particle trajectories shown occurred on noticeably different planes (out of page direction) and may indicate a toroidal form of Marangoni convection. The optical path trajectory shown in the figure may also contain some thermal component due to the PFD-water interface at (1). This is

supported by a factor of 3 increase in the horizontal particle velocity at (1) after the appearance of a gas phases. For reference, the linear velocity of particles along the perimeter of the droplet was ~50 μm/s near (1) and ~500 μm/s near (2).

An improved configuration for decreasing droplet size was implemented, as shown in Figure 38(a). This configuration uses a flow focusing technique where liquid is contained between two counter-flowing streams of oil and water. Droplet formation in this type of configuration is due primarily to the Rayleigh-Plateau instability [6]. The dimensions shown in Figure 38(a) are up-scaled by a factor of 1.5 from a popular configuration published by Anna *et al.* [136]. To minimize droplet sizes, a large fabrication aspect ratio of 4:1 (depth/width) was used and individual SU-8 pieces needed to be manually picked from PDMS channels after casting. Initial trials achieved droplet sizes of approximately 300 μm (Figure 38(b)) with a low contrast flow ratio, Q_o/Q_w, of 5:1 (PFD to water), however it is expected that 5 μm - 20 μm droplets are achievable with a Q_o/Q_w ratio of 400:1, *e.g.* with $Q_o = 4.2 \times 10^{-3}$ mL/s [112]. It is, however, left to future work to experiment with various flow conditions. A desirable result would be to optically manipulate PSM-filled aqueous droplets within a PFD phase through optical scattering forces with droplets much smaller than 300 μm. Droplets smaller than the channel height should also prevent upper and lower chip surfaces from coming into contact with the droplet, provided the PDMS is rendered hydrophobic. Alternately, varying thickness SU-8 masters, or double-layer PDMS chips can be devised where one region contains a T-junction of minimal dimensions, *e.g.* L×15×15 μm for droplet formation, and another region contains a tall sample reservoir with embedded optical fibers, such as in Figure 37(c).

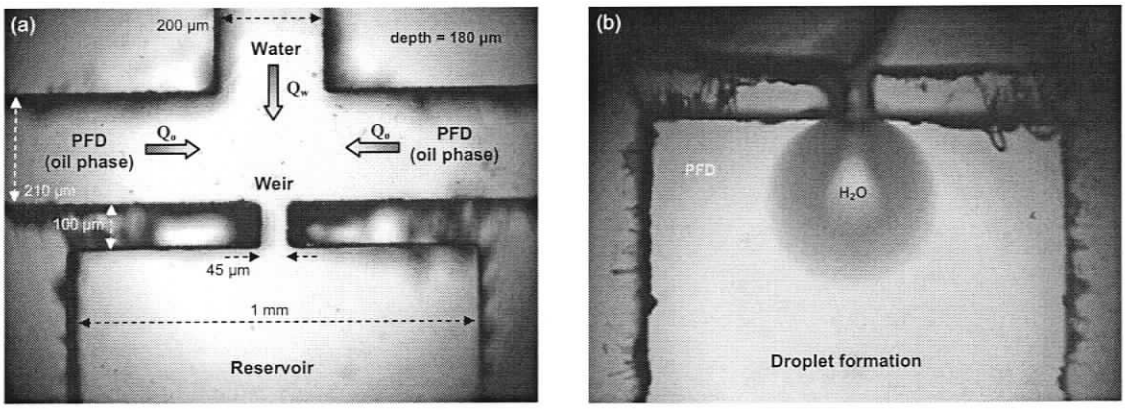

Figure 38 Microscope images of a flow focusing design used for two-phase droplet formation. (a) Channel dimensions and constituent flows are indicated. (b) Initial demonstrations of water-in-oil droplet formation for a low contrast, Q_o/Q_w, ratio.

8.4 Optical–particle Self–trapping

Optical spatial solitons are self-induced optical waveguides where a nonlinearity in the medium's refractive index compensates for the natural diffraction of the optical beam [137]. The nonlinearities leading to these solitons have been effectively instantaneous, such as in the Kerr type [138], or slow to respond, such as in the photorefractive type [139]. Another effective Kerr medium is found in liquid suspensions of dielectric nanoparticles [140]. In that medium, optical trapping is used to introduce an effective nonlinear response. The gradient force in optical trapping [3] works against diffusion to concentrate the particles within the high-intensity region of a beam. This, in turn, influences the local refractive index and allows for optical waveguiding. Self-focusing and self-trapping of light have been demonstrated experimentally [140, 141]. Figure 39 shows schematically how particle trapping forms a waveguide and that the trapping process is limited by diffusion and diffraction. Recently, it has been shown that low-loss optical waveguiding may be achieved from a liquid-core nanosphere suspension stream within a liquid-cladding waveguide [142]. The presence of the nanospheres offers new opportunities for nonlinear optical functionality in fluid environments.

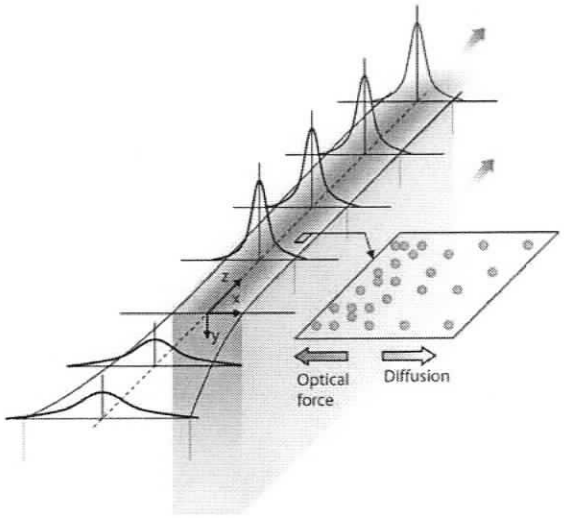

Figure 39 Schematic of particle-optical self-trapping (POST) [16]. Gradients in the local electric field intensity pull Rayleigh particles towards the beam axis. The resulting increase in particle concentration serves to waveguide the output light and further increase the trapping force on the particles. These processes are balanced by diffusion and diffraction, to give a steady beam geometry.

In this section, experimental results are provided which show an increase in Rayleigh particle concentration along the axis of a divergent beam, thus forming the basis for particle-optical self-trapping (POST). An analytic POST solution for the low-optical-intensity regime and a numerical study, including both particle transport and the optical wave equation, were presented elsewhere [16]. Figure 40(a) shows an image of a divergent PANDA-type 1550 nm lensed optical fiber, which operates at 980 nm with an output power of 100 mW. The beam is expected to be initially divergent ($>10^{o}$) in the host medium (deionized water) with a refractive index of 1.33. The particles employed were 60 nm fluorescent polystyrene spheres with refractive index of 1.574 and the sphere concentration in water was 0.1% by volume, or ~8 spheres/λ at 980 nm. The initial view of the fiber and sphere solution after 20 s of laser on-time is seen in Figure 40(a). After 5 hours of continuous lasing, a region of high sphere concentration is formed along the beam axis as shown in Figure 40(b) and is indicated by the bright region of increased fluorescence and field scattering. Spheres in solution are pulled towards the beam axis by gradient optical forces, F_g; this in turn alters the effective refractive index of the fluid near the beam axis, and in effect creates a graded index liquid/sphere-core, liquid-

cladding waveguide. Light guided through the medium allows for extended propagation and concentration distances and can be seen more visibly in Figure 40(c) for a similar experiment. The average measured width of the scattered light-field observed in Figure 40(c) was 4 μm for propagation distances between 0 μm and 80 μm from the fiber tip. The fluid nature of POST presents multiple opportunities for photonic devices and research, such as self-formed dynamic optical waveguide networks or self-healing splices for optical fibers.

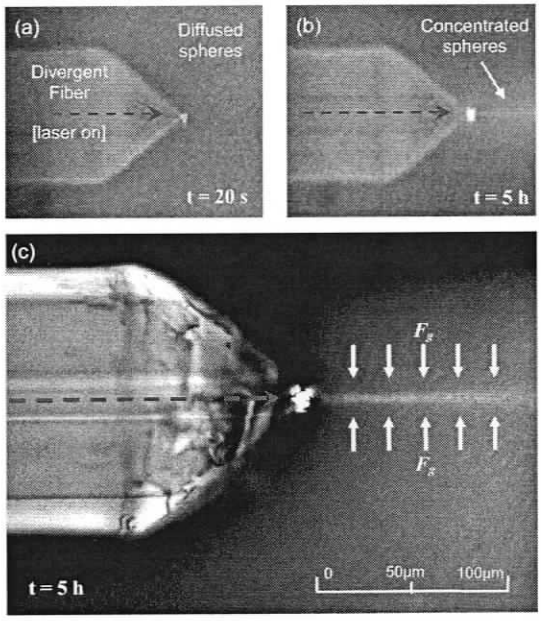

Figure 40 Far-field scattering on the beam axis of a divergent 980 nm fiber source. (a) Initial conditions after 20 s of laser on-time and (b)(c) after 5 hours of on-time. The medium surrounding the fiber is water with a Rayleigh sphere concentration of 1:1000 by volume.

8.5 SUMMARY

In this chapter the effects optical joule heating with embedded optical fibers were considered in a PDMS microfluidic environment. The occurrence of localized boiling and gas phase formation was found to increase greatly when 1550 nm sources were used as compared with 980 nm sources. The existence of thermal effects near the gas-water boundary was found to cause fluctuations in trapped particle positions and collective large scale particle circulation was observed for water-oil-gas systems. For dual-beam

trapping configurations containing counter-propagating 980 nm and 1550 nm sources, defined axial trapping regions were found to exist where particles either oscillated or trapped stably depending on particle position in the beam. This state of trapping could be controlled by either power or polarization manipulation. Other demonstrations in this trapping regime included continuous circulation of a particle assembly, active particle switching/storage, and three-dimensional rotation of an assembly of spheres. The formation of two-phase systems were considered and inner droplet trapping and circulation was characterized. Finally, particle-optical self-trapping was demonstrated with a lensed optical fiber in a contained microfluidic system.

BIBLIOGRAPHY

[1] A. Ashkin, "Optical trapping and manipulation of neutral particles using lasers," *Proceedings of the National Academy of Sciences of the United States of America,* vol. 94, pp. 4853-4860, 1997.

[2] D. G. Grier, "A revolution in optical manipulation," *Nature,* vol. 424, pp. 810-816, 2003.

[3] K. C. Neuman and S. M. Block, "Optical trapping," *Review of Scientific Instruments,* vol. 75, pp. 2787-2809, 2004.

[4] K. Dholakia and P. Reece, "Optical micromanipulation takes hold," *Nano Today,* vol. 1, pp. 18-27, 2006.

[5] A. Ashkin, "Acceleration and trapping of particles by radiation pressure," *Physical Review Letters,* vol. 24, pp. 156-159, 1970.

[6] T. M. Squires and S. R. Quake, "Microfluidics: Fluid physics at the nanoliter scale," *Reviews of Modern Physics,* vol. 77, pp. 977-1026, 2005.

[7] G. M. Whitesides, "The origins and the future of microfluidics," *Nature,* vol. 442, pp. 368-373, 2006.

[8] P. S. Dittrich, K. Tachikawa, and A. Manz, "Micro total analysis systems. Latest advancements and trends," *Analytical Chemistry,* vol. 78, pp. 3887-3907, 2006.

[9] D. Psaltis, S. R. Quake, and C. H. Yang, "Developing optofluidic technology through the fusion of microfluidics and optics," *Nature,* vol. 442, pp. 381-386, 2006.

[10] C. Monat, P. Domachuk, and B. J. Eggleton, "Integrated optofluidics: A new river of light," *Nature Photonics,* vol. 1, pp. 106-114, 2007.

[11] H. C. Hunt and J. S. Wilkinson, "Optofluidic integration for microanalysis," *Microfluidics and Nanofluidics,* vol. 4, pp. 53-79, 2008.

[12] S. A. Tatarkova, A. E. Carruthers, and K. Dholakia, "One-dimensional optically bound arrays of microscopic particles," *Physical Review Letters,* vol. 89, 093045, 2002.

[13] J. T. Blakely, R. Gordon, and D. Sinton, "Flow-dependent optofluidic particle trapping and circulation," *Lab Chip,* vol. 8, pp. 1350-1356, 2008.

[14] R. Gordon, M. Kawano, J. T. Blakely, and D. Sinton, "Optohydrodynamic theory of particles in a dual-beam optical trap," *Physical Review B,* vol. 77, 245125, 2008.

[15] M. Kawano, J. T. Blakely, R. Gordon, and D. Sinton, "Theory of dielectric micro-sphere dynamics in a dual-beam optical trap," *Optics Express,* vol. 16, pp. 9306-9317, June 2008 2008.

[16] R. Gordon, J. T. Blakely, and D. Sinton, "Particle-optical self-trapping," *Physical Review A,* vol. 75, 055801, 2007.

[17] H. He, M. E. J. Friese, N. R. Heckenberg, and H. Rubinsztein-Dunlop, "Direct observation of transfer of angular momentum to absorptive particles from a laser beam with a phase singularity," *Physical Review Letters,* vol. 75, pp. 826-829, 1995.

[18] M. E. J. Friese, J. Enger, H. Rubinsztein-Dunlop, and N. R. Heckenberg, "Optical angular-momentum transfer to trapped absorbing particles," *Physical Review A,* vol. 54, pp. 1593-1596, 1996.

[19] M. E. J. Friese, T. A. Nieminen, N. R. Heckenberg, and H. Rubinsztein-Dunlop, "Optical alignment and spinning of laser-trapped microscopic particles," *Nature,* vol. 394, pp. 348-350, 1998.

[20] L. Allen, M. W. Beijersbergen, R. J. C. Spreeuw, and J. P. Woerdman, "Orbital angular momentum of light and the transformation of Laguerre-Gaussian laser modes," *Physical Review A,* vol. 45, pp. 8185-8189, 1992.

[21] H. C. van de Hulst, *Light scattering by small particles*. New York,: Wiley, 1957.

[22] G. Gouesbet, B. Maheu, and G. Grehan, "Light scattering from a sphere arbitrarily located in a Gaussian beam, using a Bromwich formulation," *Journal of the Optical Society of America a-Optics Image Science and Vision,* vol. 5, pp. 1427-1443, 1988.

[23] K. F. Ren, G. Greha, and G. Gouesbet, "Radiation pressure forces exerted on a particle arbitrarily located in a Gaussian beam by using the generalized Lorenz-Mie theory, and associated resonance effects," *Optics Communications,* vol. 108, pp. 343-354, 1994.

[24] W. J. Wiscombe, "Improved Mie scattering algorithms," *Applied Optics,* vol. 19, pp. 1505-1509, 1980.

[25] K. Svoboda and S. M. Block, "Biological applications of optical forces," *Annual Review of Biophysics and Biomolecular Structure,* vol. 23, pp. 247-285, 1994.

[26] A. Ashkin, "Forces of a single-beam gradient laser trap on a dielectric spheres in the ray optics regime," *Biophysical Journal,* vol. 61, pp. 569-582, 1992.

[27] S. O. Kasap, *Optoelectronics and Photonics*. Upper Saddle River, New Jersey: Prentice Hall, 2001.

[28] Z. H. Liu, C. K. Guo, J. Yang, and L. B. Yuan, "Tapered fiber optical tweezers for microscopic particle trapping: fabrication and application," *Optics Express,* vol. 14, pp. 12510-12516, 2006.

[29] T. Kaneta, Y. Ishidzu, N. Mishima, and T. Imasaka, "Theory of optical chromatography," *Analytical Chemistry,* vol. 69, pp. 2701-2710, 1997.

[30] Y. Harada and T. Asakura, "Radiation forces on a dielectric sphere in the Rayleigh scattering regime," *Optics Communications,* vol. 124, pp. 529-541, 1996.

[31] L. Novotny and B. Hecht, *Principles of Nano-Optics*. Cambridge: Cambridge University Press, 2006.

[32] A. Ashkin, J. M. Dziedzic, J. E. Bjorkholm, and S. Chu, "Observation of a single-beam gradient force optical trap for dielectric particles," *Optics Letters,* vol. 11, pp. 288-290, 1986.

[33] J. D. Jackson, *Classical Electrodynamics*, 3 ed. New York: Wiley, 1999.

[34] Hafner Christian., *The generalized multipole technique for computational electromagnetics*. Boston: Artech House, 1990.

[35] D. Ganic, X. S. Gan, and M. Gu, "Exact radiation trapping force calculation based on vectorial diffraction theory," *Optics Express,* vol. 12, pp. 2670-2675, 2004.

[36] A. Rohrbach and E. H. K. Stelzer, "Trapping forces, force constants, and potential depths for dielectric spheres in the presence of spherical aberrations," *Applied Optics,* vol. 41, pp. 2494-2507, 2002.

[37] T. M. Grzegorczyk, B. A. Kemp, and J. A. Kong, "Trapping and binding of an arbitrary number of cylindrical particles in an in-plane electromagnetic field," *Journal of the Optical Society of America a-Optics Image Science and Vision,* vol. 23, pp. 2324-2330, 2006.

[38] B. T. Draine and P. J. Flatau, "Discrete dipole approximation for scattering calculations," *Journal of the Optical Society of America a-Optics Image Science and Vision,* vol. 11, pp. 1491-1499, 1994.

[39] M. I. Mishchenko, "Light scattering by randomly oriented axially symmetrical particles," *Journal of the Optical Society of America a-Optics Image Science and Vision,* vol. 8, pp. 871-882, 1991.

[40] A. R. Zakharian, M. Mansuripur, and J. V. Moloney, "Radiation pressure and the distribution of electromagnetic force in dielectric media," *Optics Express,* vol. 13, pp. 2321-2336, 2005.

[41] R. C. Gauthier, "Computation of the optical trapping force using an FDTD based technique," *Optics Express,* vol. 13, pp. 3707-3718, 2005.

[42] K. F. Ren, G. Grehan, and G. Gouesbet, "Prediction of reverse radiation pressure by generalized Lorenz-Mie theory," *Applied Optics,* vol. 35, pp. 2702-2710, 1996.

[43] J. A. Lock, "Calculation of the radiation trapping force for laser tweezers by use of generalized Lorenz-Mie theory. I. Localized model description of an on-axis tightly focused laser beam with spherical aberration," *Applied Optics,* vol. 43, pp. 2532-2544, 2004.

[44] V. Karasek, K. Dholakia, and P. Zemanek, "Analysis of optical binding in one dimension," *Applied Physics B: Lasers and Optics,* vol. 84, pp. 149-156, 2006.

[45] V. Karasek and P. Zemanek, "Analytical description of longitudinal optical binding of two spherical nanoparticles," *Journal of Optics A: Pure and Applied Optics,* vol. 9, pp. S215-S220, 2007.

[46] N.-T. Nguyen, *Fundamentals and Applications of Microfluidics*. Norwood, MA: Artech House, 2002.

[47] B. E. A. Saleh and M. C. Teich, *Fundamentals of Photonics*. New York: John Wiley & Sons, 1991.

[48] R. W. Applegate, J. Squier, T. Vestad, J. Oakey, and D. W. M. Marr, "Optical trapping, manipulation, and sorting of cells and colloids in microfluidic systems with diode laser bars," *Optics Express,* vol. 12, pp. 4390-4398, 2004.

[49] B. S. Schmidt, A. H. J. Yang, D. Erickson, and M. Lipson, "Optofluidic trapping and transport on solid core waveguides within a microfluidic device," *Optics Express,* vol. 15, pp. 14322-14334, 2007.

[50] A. Ashkin, "Applications of laser radiation pressure," *Science,* vol. 210, pp. 1081-1088, 1980.

[51] A. Ashkin and J. M. Dziedzic, "Optical trapping and manipulation of viruses and bacteria," *Science,* vol. 235, pp. 1517-1520, 1987.

[52] S. B. Smith, Y. J. Cui, and C. Bustamante, "Overstretching B-DNA: The elastic response of individual double-stranded and single-stranded DNA molecules," *Science,* vol. 271, pp. 795-799, 1996.

[53] R. M. Lorenz, J. S. Edgar, G. D. M. Jeffries, Y. Q. Zhao, D. McGloin, and D. T. Chiu, "Vortex-trap-induced fusion of femtoliter-volume aqueous droplets," *Analytical Chemistry,* vol. 79, pp. 224-228, 2007.

[54] N. Pamme, R. Koyama, and A. Manz, "Counting and sizing of particles and particle agglomerates in a microfluidic device using laser light scattering: application to a particle-enhanced immunoassay," *Lab on a Chip,* vol. 3, pp. 187-192, 2003.

[55] D. L. Yin, E. J. Lunt, M. I. Rudenko, D. W. Deamer, A. R. Hawkins, and H. Schmidt, "Planar optofluidic chip for single particle detection, manipulation, and analysis," *Lab on a Chip,* vol. 7, pp. 1171-1175, 2007.

[56] Q. Kou, I. Yesilyurt, V. Studer, M. Belotti, E. Cambril, and Y. Chen, "On-chip optical components and microfluidic systems," *Microelectronic Engineering,* vol. 73-4, pp. 876-880, 2004.

[57] S. Camou, H. Fujita, and T. Fujii, "PDMS 2D optical lens integrated with microfluidic channels: principle and characterization," *Lab on a Chip,* vol. 3, pp. 40-45, 2003.

[58] S. K. Hsiung, C. H. Lin, and G. B. Lee, "A microfabricated capillary electrophoresis chip with multiple buried optical fibers and microfocusing lens for multiwavelength detection," *Electrophoresis,* vol. 26, pp. 1122-1129, 2005.

[59] A. Constable, J. Kim, J. Mervis, F. Zarinetchi, and M. Prentiss, "Demonstration of a fiber optic light-force trap," *Optics Letters,* vol. 18, pp. 1867-1869, 1993.

[60] M. Ozkan, M. Wang, C. Ozkan, R. Flynn, A. Birkbeck, and S. Esener, "Optical manipulation of objects and biological cells in microfluidic devices," *Biomedical Microdevices,* vol. 5, pp. 61-67, 2003.

[61] S. Cran-McGreehin, T. F. Krauss, and K. Dholakia, "Integrated monolithic optical manipulation," *Lab on a Chip,* vol. 6, pp. 1122-1124, 2006.

[62] P. Domachuk, I. C. M. Littler, M. Cronin-Golomb, and B. J. Eggleton, "Compact resonant integrated microfluidic refractometer," *Applied Physics Letters,* vol. 88, 093513, 2006.

[63] B. Lincoln, S. Schinkinger, K. Travis, F. Wottawah, S. Ebert, F. Sauer, and J. Guck, "Reconfigurable microfluidic integration of a dual-beam laser trap with biomedical applications," *Biomedical Microdevices,* vol. 9, pp. 703-710, 2007.

[64] C. Jensen-McMullin, H. P. Lee, and E. R. Lyons, "Demonstration of trapping, motion control, sensing and fluorescence detection of polystyrene beads in a multi-fiber optical trap," *Optics Express,* vol. 13, pp. 2634-2642, 2005.

[65] V. Lien and F. Vollmer, "Microfluidic flow rate detection based on integrated optical fiber cantilever," *Lab on a Chip,* vol. 7, pp. 1352-1356, 2007.

[66] C. H. Lin, G. B. Lee, L. M. Fu, and S. H. Chen, "Integrated optical-fiber capillary electrophoresis microchips with novel spin-on-glass surface modification," *Biosensors & Bioelectronics,* vol. 20, pp. 83-90, 2004.

[67] J. Guck, S. Schinkinger, B. Lincoln, F. Wottawah, S. Ebert, M. Romeyke, D. Lenz, H. M. Erickson, R. Ananthakrishnan, D. Mitchell, J. Kas, S. Ulvick, and C. Bilby, "Optical deformability as an inherent cell marker for testing malignant transformation and metastatic competence," *Biophysical Journal,* vol. 88, pp. 3689-3698, 2005.

[68] P. R. T. Jess, V. Garces-Chavez, D. Smith, M. Mazilu, L. Paterson, A. Riches, C. S. Herrington, W. Sibbett, and K. Dholakia, "Dual beam fibre trap for Raman microspectroscopy of single cells," *Optics Express,* vol. 14, pp. 5779-5791, 2006.

[69] F. C. Huang, C. S. Liao, and G. B. Lee, "An integrated microfluidic chip for DNA/RNA amplification, electrophoresis separation and on-line optical detection," *Electrophoresis,* vol. 27, pp. 3297-3305, 2006.

[70] L. Cui, T. Zhang, and H. Morgan, "Optical particle detection integrated in a dielectrophoretic lab-on-a-chip," *Journal of Micromechanics and Microengineering,* vol. 12, pp. 7-12, 2002.

[71] A. Yang, S. Mandal, and D. Erickson, "Microfluidic and nanofluidic transport using advanced photonic devices," in *ASME International Mechanical Engineering Congress and Exposition* Chicago, 2006.

[72] J. Enger, M. Goksor, K. Ramser, P. Hagberg, and D. Hanstorp, "Optical tweezers applied to a microfluidic system," *Lab on a Chip,* vol. 4, pp. 196-200, 2004.

[73] T. Hatano, T. Kaneta, and T. Imasaka, "Application of optical chromatography to immunoassay," *Analytical Chemistry,* vol. 69, pp. 2711-2715, 1997.

[74] N. Mishima, T. Kaneta, and T. Imasaka, "The "Optical Funnel". A technique for measuring a microorganism's power," *Analytical Chemistry,* vol. 70, pp. 3513-3515, 1998.

[75] J. Makihara, T. Kaneta, and T. Imasaka, "Optical chromatography: Size determination by eluting particles," *Talanta,* vol. 48, pp. 551-557, 1999.

[76] T. Kaneta, J. Makihara, and T. Imasaka, "An "optical channel": A technique for the evaluation of biological cell elasticity," *Analytical Chemistry,* vol. 73, pp. 5791-5795, 2001.

[77] S. J. Hart and A. V. Terray, "Refractive-index-driven separation of colloidal polymer particles using optical chromatography," *Applied Physics Letters,* vol. 83, pp. 5316-5318, 2003.

[78] A. Terray, J. Arnold, and S. J. Hart, "Enhanced optical chromatography in a PDMS microfluidic system," *Optics Express,* vol. 13, pp. 10406-10415, 2005.

[79] E. Yablonovitch, "Inhibited spontaneous emission in solid-state physics and electronics," *Physical Review Letters,* vol. 58, pp. 2059-2062, 1987.

[80] M. M. Burns, J. M. Fournier, and J. A. Golovchenko, "Optical binding," *Physical Review Letters,* vol. 63, pp. 1233-1236, 1989.

[81] W. Singer, M. Frick, S. Bernet, and M. Ritsch-Marte, "Self-organized array of regularly spaced microbeads in a fiber-optical trap," *Journal of the Optical Society of America B-Optical Physics,* vol. 20, pp. 1568-1574, 2003.

[82] H. C. Nagerl, W. Bechter, J. Eschner, F. Schmidt-Kaler, and R. Blatt, "Ion strings for quantum gates," *Applied Physics B-Lasers and Optics,* vol. 66, pp. 603-608, 1998.

[83] N. K. Metzger, K. Dholakia, and E. M. Wright, "Observation of bistability and hysteresis in optical binding of two dielectric spheres," *Physical Review Letters,* vol. 96, 2006.

[84] N. K. Metzger, E. M. Wright, W. Sibbett, and K. Dholakia, "Visualization of optical binding of microparticles using a femtosecond fiber optical trap," *Optics Express,* vol. 14, pp. 3677-3687, 2006.

[85] D. McGloin, A. E. Carruthers, K. Dholakia, and E. M. Wright, "Optically bound microscopic particles in one dimension," *Physical Review E,* vol. 69, 021403, 2004.

[86] N. K. Metzger, R. F. Marchington, M. Mazilu, R. L. Smith, K. Dholakia, and E. M. Wright, "Measurement of the restoring forces acting on two optically bound particles from normal mode correlations," *Physical Review Letters,* vol. 98, 2007.

[87] J. Ng, C. T. Chan, P. Sheng, and Z. F. Lin, "Strong optical force induced by morphology-dependent resonances," *Optics Letters,* vol. 30, pp. 1956-1958, 2005.

[88] T. Cizmar, V. Garces-Chavez, K. Dholakia, and P. Zemanek, "Optical conveyor belt for delivery of submicron objects," *Applied Physics Letters,* vol. 86, 2005.

[89] M. Guillon, O. Moine, and B. Stout, "Longitudinal optical binding of high optical contrast microdroplets in air," *Physical Review Letters,* vol. 96, 2006.

[90] F. J. G. de Abajo, "Collective oscillations in optical matter," *Optics Express,* vol. 15, pp. 11082-11094, 2007.

[91] J. D. Prestage, A. Williams, L. Maleki, M. J. Djomehri, and E. Harabetian, "Dynamics of charged-particles in a paul radiofrequency quadrupole trap," *Physical Review Letters,* vol. 66, pp. 2964-2967, 1991.

[92] D. C. Duffy, J. C. McDonald, O. J. A. Schueller, and G. M. Whitesides, "Rapid prototyping of microfluidic systems in poly(dimethylsiloxane)," *Analytical Chemistry,* vol. 70, pp. 4974-4984, 1998.

[93] J. C. McDonald and G. M. Whitesides, "Poly(dimethylsiloxane) as a material for fabricating microfluidic devices," *Accounts of Chemical Research,* vol. 35, pp. 491-499, 2002.

[94] MicroChem, "Nano SU-8: Negative tone photoresist, formulations 50-100," Newton, MA, 2002.

[95] J. M. K. Ng, I. Gitlin, A. D. Stroock, and G. M. Whitesides, "Components for integrated poly(dimethylsiloxane) microfluidic systems," *Electrophoresis,* vol. 23, pp. 3461-3473, 2002.

[96] S. P. Gross, "Application of optical traps in vivo," *Biophotonics, Pt B,* vol. 361, pp. 162-174, 2003.

[97] D. Gloge, "Weakly guiding fibers," *Applied Optics,* vol. 10, pp. 2252-2258, 1971.

[98] E. Snitzer, "Cylindrical dielectric waveguide modes," *Journal Optical Society of America,* vol. 51, pp. 491-498, 1961.

[99] W. Silfvast, *Laser Fundamentals*, 2 ed. Cambridge, UK: Cambridge University Press, 2004.

[100] A. T. O'Neil and M. J. Padgett, "Three-dimensional optical confinement of micron-sized metal particles and the decoupling of the spin and orbital angular momentum within an optical spanner," *Optics Communications,* vol. 185, pp. 139-143, 2000.

[101] H. He, M. E. J. Friese, N. R. Heckenberg, and H. Rubinsztein-Dunlop, "Direct observation of transfer of angular momentum to absorptive particles from a laser beam with a phase singularity," *Physical Review Letters,* vol. 75, pp. 826-829, 1995.

[102] P. Galajda and P. Ormos, "Orientation of flat particles in optical tweezers by linearly polarized light," *Optics Express,* vol. 11, pp. 446-451, Mar 2003.

[103] X. Y. Ma, J. Q. Lu, R. S. Brock, K. M. Jacobs, P. Yang, and X. H. Hu, "Determination of complex refractive index of polystyrene microspheres from 370 to 1610 nm," *Physics in Medicine and Biology,* vol. 48, pp. 4165-4172, 2003.

[104] S. Prahl, "Mie Scattering Calculator," 2007, p. http://omlc.ogi.edu/calc/mie_calc.html (Accessed: Sept. 2007).

[105] D. Sinton, "Microscale flow visualization," *Microfluidics and Nanofluidics,* vol. 1, pp. 2-21, 2004.

[106] R. Gomez-Medina, P. San Jose, A. Garcia-Martin, M. Lester, M. Nieto-Vesperinas, and J. J. Saenz, "Resonant radiation pressure on neutral particles in a waveguide," *Physical Review Letters,* vol. 86, pp. 4275-4277, 2001.

[107] K. Koba, H. Ikuno, and M. Kawano, *Numerical analysis of electromagnetic scattering from 3-D dielectric objects using the Yasuura method.* New York: Wiley, 2004.

[108] D. Erickson, D. Sinton, and D. Q. Li, "Joule heating and heat transfer in poly(dimethylsiloxane) microfluidic systems," *Lab on a Chip,* vol. 3, pp. 141-149, 2003.

[109] A. Ashkin and J. M. Dziedzic, "Observation of optical resonances of dielectric spheres by light scattering," *Applied Optics,* vol. 20, pp. 1803-1814, 1981.

[110] P. Bartlett, S. I. Henderson, and S. J. Mitchell, "Measurement of the hydrodynamic forces between two polymer-coated spheres," *Philosophical Transactions of the Royal Society A,* vol. 359, pp. 883-893, May 2001.

[111] J. C. Meiners and S. R. Quake, "Direct measurement of hydrodynamic cross correlations between two particles in an external potential," *Physical Review Letters,* vol. 82, pp. 2211-2214, 1999.

[112] V. Lien, Y. Berdichevsky, and Y. H. Lo, "A prealigned process of integrating optical waveguides with microfluidic devices," *Ieee Photonics Technology Letters,* vol. 16, pp. 1525-1527, 2004.

[113] W. H. Wright, G. J. Sonek, and M. W. Berns, "Parametric study of the forces on microspheres held by optical tweezers," *Applied Optics,* vol. 33, pp. 1735-1748, 1994.

[114] R. S. Dutra, N. B. Viana, P. A. M. Neto, and H. M. Nussenzveig, "Polarization effects in optical tweezers," *Journal of Optics A: Pure and Applied Optics,* vol. 9, pp. S221-S227, 2007.

[115] K. F. Palmer and D. Williams, "Optical properties of water in near infrared," *Journal of the Optical Society of America,* vol. 64, pp. 1107-1110, 1974.

[116] Y. Liu, D. K. Cheng, G. J. Sonek, M. W. Berns, C. F. Chapman, and B. J. Tromberg, "Evidence for localized cell heating induced by infrared optical tweezers," *Biophysical Journal,* vol. 68, pp. 2137-2144, 1995.

[117] A. Schonle and S. W. Hell, "Heating by absorption in the focus of an objective lens," *Optics Letters,* vol. 23, pp. 325-327, 1998.

[118] P. M. Celliers and J. Conia, "Measurement of localized heating in the focus of an optical trap," *Applied Optics,* vol. 39, pp. 3396-3407, 2000.

[119] W. Callister, *Materials Science and Engineering: An Introduction.* Hoboken, NJ: John Wiley & Sons, 2003.

[120] P. Michel, J. Dugas, J. M. Cariou, and L. Martin, "Thermal variations of refractive index of PMMA, Polystyrene, and Poly(4-methyl-1-pentene)," *Journal of Macromolecular Science-Physics,* vol. B25, pp. 379-394, 1986.

[121] P. Schiebener, J. Straub, J. Sengers, and J. S. Gallagher, "Refractive index of water and steam as a function of wavelength, temperature, and density," *Journal of Physical and Chemical Reference Data,* vol. 19, pp. 677-717, 1990.

[122] I. Shames, *Mechanics of fluids*, 4 ed. New York: McGraw-Hill, 2002.

[123] A. Gunther and K. F. Jensen, "Multiphase microfluidics: from flow characteristics to chemical and materials synthesis," *Lab on a Chip,* vol. 6, pp. 1487-1503, 2006.

[124] C. N. Baroud and H. Willaime, "Multiphase flows in microfluidics," *Comptes Rendus Physique,* vol. 5, pp. 547-555, 2004.

[125] C. J. Morris and B. A. Parviz, "Self-assembly and characterization of Marangoni microfluidic actuators," *Journal of Micromechanics and Microengineering,* vol. 16, pp. 972-980, 2006.

[126] K. T. Kotz, K. A. Noble, and G. W. Faris, "Optical microfluidics," *Applied Physics Letters,* vol. 85, pp. 2658-2660, 2004.

[127] E. Lajeunesse and G. M. Homsy, "Thermocapillary migration of long bubbles in polygonal tubes. II. Experiments," *Physics of Fluids,* vol. 15, pp. 308-314, 2003.

[128] A. A. Darhuber, J. P. Valentino, J. M. Davis, S. M. Troian, and S. Wagner, "Microfluidic actuation by modulation of surface stresses," *Applied Physics Letters,* vol. 82, pp. 657-659, 2003.

[129] R. H. Farahi, A. Passian, T. L. Ferrell, and T. Thundat, "Microfluidic manipulation via Marangoni forces," *Applied Physics Letters,* vol. 85, pp. 4237-4239, 2004.

[130] N. Garnier, R. O. Grigoriev, and M. F. Schatz, "Optical manipulation of microscale fluid flow," *Physical Review Letters,* vol. 91, 2003.

[131] C. N. Baroud, M. R. de Saint Vincent, and J. P. Delville, "An optical toolbox for total control of droplet microfluidics," *Lab on a Chip,* vol. 7, pp. 1029-1033, 2007.

[132] A. D. Stroock, R. F. Ismagilov, H. A. Stone, and G. M. Whitesides, "Fluidic ratchet based on Marangoni-Benard convection," *Langmuir,* vol. 19, pp. 4358-4362, 2003.

[133] T. T. Lam, "Thermocapillary convection in an absorbing-scattering medium subjected to irradiation," *International Journal of Heat and Fluid Flow,* vol. 14, pp. 349-356, 1993.

[134] D. Agble and M. A. Mendes-Tatsis, "The prediction of Marangoni convection in binary liquid-liquid systems with added surfactants," *International Journal of Heat and Mass Transfer,* vol. 44, pp. 1439-1449, 2001.

[135] E. Nakache, M. Dupeyrat, and M. Vignesadler, "The contribution of chemistry to new Marangoni mass-transfer instabilities at the oil-water interface," *Faraday Discussions,* vol. 77, pp. 189-196, 1984.

[136] S. L. Anna, N. Bontoux, and H. A. Stone, "Formation of dispersions using "flow focusing" in microchannels," *Applied Physics Letters,* vol. 82, pp. 364-366, 2003.

[137] G. I. Stegeman and M. Segev, "Optical spatial solitons and their interactions: Universality and diversity," *Science,* vol. 286, pp. 1518-1523, 1999.

[138] R. Y. Chiao, E. Garmire, and C. H. Townes, "Self-trapping of optical beams," *Physical Review Letters,* vol. 13, p. 479, 1964.

[139] M. Segev, B. Crosignani, A. Yariv, and B. Fischer, "Spatial solitons in photorefractive media," *Physical Review Letters,* vol. 68, pp. 923-926, 1992.

[140] P. W. Smith, P. J. Maloney, and A. Ashkin, "Use of a liquid suspension of dielectric spheres as an artificial Kerr medium," *Optics Letters,* vol. 7, pp. 347-349, 1982.

[141] V. E. Yashin, S. A. Chizhov, R. L. Sabirov, T. V. Starchikova, N. V. Vysotina, N. N. Rozanov, V. E. Semenov, V. A. Smirnov, and S. V. Fedorov, "Formation of soliton-like light beams in an aqueous suspension of polystyrene particles," *Optics and Spectroscopy,* vol. 98, pp. 466-469, 2005.

[142] R. S. Conroy, B. T. Mayers, D. V. Vezenov, D. B. Wolfe, M. G. Prentiss, and G. M. Whitesides, "Optical waveguiding in suspensions of dielectric particles," *Applied Optics,* vol. 44, pp. 7853-7857, 2005.

[143] J. A. Stratton, *Electromagnetic theory*. New York: McGraw-Hill, 1941.

[144] M. Doi and S. F. Edwards, *The theory of polymer dynamics*. Oxford: Oxford Press, 1994.

[145] J. P. Barton and D. R. Alexander, "Fifth-order corrected electromagnetic field components for a fundamental Gaussian beam," *Journal of Applied Physics,* vol. 66, pp. 2800-2802, 1989.

[146] L. S. Inc., "FDTD Solutions," http://www.lumerical.com, 2008.

APPENDIX

OPTO–HYDRODYNAMIC THEORY

To analyze the experimentally observed results, an opto-hydrodynamic numerical model is provided and has been reported recently in a joint publication with Dr. Kawano [15]. Figure 41 shows polystyrene microspheres (PSMs) of radius a trapped between opposing fibers separated by a distance D_{bf}. The divergent beams (DB_1 and DB_2) from the optical fibers (OF_1 and OF_2) are modeled by a Gaussian beam. To make the model realistic, we consider the case of transversely misaligned beam axes ($D_{off} \neq 0$), in addition to the case of perfectly aligned beam axes ($D_{off} = 0$), where D_{off} is the distance between the beam axes (BA_1 and BA_2). As shown previously, this misalignment results in spontaneous oscillation of the particle array.

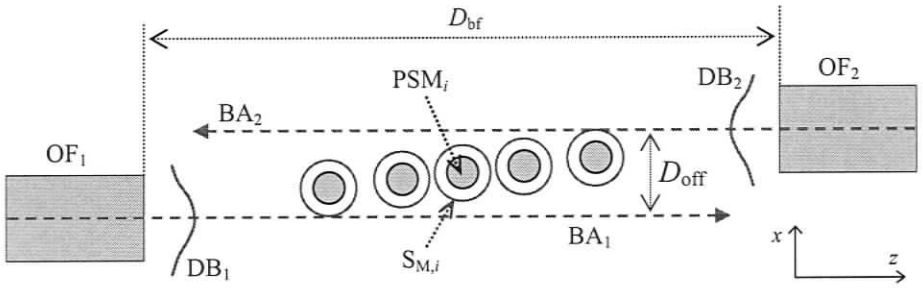

Figure 41 Schematic used to model the dual-beam fiber trap [15].

Optical Force Calculation

To calculate the inhomogeneous spacing and the spontaneous oscillation observed in the experiment, the optical force acting on particles in the dual-beam trap needs to be calculated. The time averaged optical force $\mathbf{F}_i$ acting on the i^{th} particle can be calculated by integrating the Maxwell stress tensor $\ddot{\mathbf{T}}$ over a closed surface $S_{M,i}$ which surrounds the particle [33]:

$$\mathbf{F}_i = \int_{S_{M,i}} \ddot{\mathbf{T}} \cdot \mathbf{v}_M dS, \tag{A.1}$$

where $\mathbf{v}_M$ is a unit normal vector of the closed surface. The Maxwell stress tensor (MST), $\ddot{\mathbf{T}}$ is given by

$$\ddot{\mathbf{T}} = \frac{1}{2}\mathrm{Re}\left[\varepsilon\mathbf{E}(\mathbf{r})\mathbf{E}^*(\mathbf{r}) + \mu\mathbf{H}(\mathbf{r})\mathbf{H}^*(\mathbf{r}) - \frac{1}{2}\left\{\varepsilon|\mathbf{E}(\mathbf{r})|^2 + \mu|\mathbf{H}(\mathbf{r})|^2\right\}\ddot{\mathbf{I}}\right], \tag{A.2}$$

where ε and μ are the permittivity and the permeability of the surrounding medium, respectively, * represents the complex conjugate of, **EE*** is a dyadic product, $\ddot{\mathbf{I}}$ is the unit tensor, and Re is the real part of. The electric and magnetic fields **E** and **H** are, respectively, given by

$$\mathbf{E} = \mathbf{E}^{\mathrm{in}} + \mathbf{E}^{\mathrm{sc}} \text{ and } \mathbf{H} = \mathbf{H}^{\mathrm{in}} + \mathbf{H}^{\mathrm{sc}}, \tag{A.3}$$

where $\mathbf{E}^{\mathrm{in}}$ and $\mathbf{H}^{\mathrm{in}}$ are the incident fields, *i.e.* divergent beams from the fiber facets, and $\mathbf{E}^{\mathrm{sc}}$ and $\mathbf{H}^{\mathrm{sc}}$ are the scattered fields by the particles.

In order to obtain the scattered fields $\mathbf{E}^{\mathrm{sc}}$ and $\mathbf{H}^{\mathrm{sc}}$ numerically, we apply the generalized multipole technique (GMT) [34, 107] to the multi-sphere system. To apply this method, we first express the approximate scattered electric field at a point **r**, $\mathbf{E}_{\mathrm{N}}^{\mathrm{sc}}(\mathbf{r})$, as

$$\mathbf{E}_{\mathrm{N}}^{\mathrm{sc}}(\mathbf{r}) = \sum_{i=1}^{I} \mathbf{E}_{i,\mathrm{N}}^{\mathrm{sc}}(\mathbf{r}_i), \tag{A.4}$$

where I is the total number of particles, $\mathbf{r}_i$ denotes a position **r** in the i^{th} local coordinate system with origin O_i located at the centre of the i^{th} particle, and $\mathbf{E}_{i,N}^{\mathrm{sc}}(\mathbf{r}_i)$ is the scattered electric field from the i^{th} particle. Following the GMT, we expand $\mathbf{E}_{i,N}^{\mathrm{sc}}(\mathbf{r}_i)$ as

$$\mathbf{E}_{i,N}^{\mathrm{sc}}(\mathbf{r}_i) = \sum_{n=1}^{N} \sum_{m=-n}^{n} a_{nm}^{i}(N)\mathbf{m}_{nm}^{(4)}(k\mathbf{r}_i) + b_{nm}^{i}(N)\mathbf{n}_{nm}^{(4)}(k\mathbf{r}_i), \tag{A.5}$$

where $\mathbf{m}_{nm}^{(4)}$ and $\mathbf{n}_{nm}^{(4)}$ are the Hankel function-based spherical vector wave functions (SVWFs) [143], N is a truncation size of the expansion that is given depending on a desired accuracy of the solution, and a_{nm}^{i} and b_{nm}^{i} are unknown coefficients to be determined. To calculate these coefficients, we also need to expand the transmitted field inside the i^{th} particle, $\mathbf{E}_{i,N}^{\mathrm{tr}}(\mathbf{r}_i)$, by SVWFs as

$$\mathbf{E}_{i,N}^{\mathrm{tr}}(\mathbf{r}_i) = \sum_{n=1}^{N} \sum_{m=-n}^{n} c_{nm}^{i}(N)\mathbf{m}_{nm}^{(1)}(k_i\mathbf{r}_i) + d_{nm}^{i}(N)\mathbf{n}_{nm}^{(1)}(k_i\mathbf{r}_i), \tag{A.6}$$

where $\mathbf{m}_{nm}^{(1)}$ and $\mathbf{n}_{nm}^{(1)}$ are Bessel function based SVWFs [143], and c_{nm}^{i} and d_{nm}^{i} are unknown coefficients. Using Faraday's law and the relation, $\nabla\times\mathbf{m}=k\mathbf{n}$ and $\nabla\times\mathbf{n}=k\mathbf{m}$, where k is the wave number, the scattered magnetic field from the i^{th} particle, $\mathbf{H}_{i,N}^{\text{sc}}(\mathbf{r}_i)$, and the transmitted magnetic field inside the i^{th} particle, $\mathbf{H}_{i,N}^{\text{tr}}(\mathbf{r}_i)$, are given by

$$\mathbf{H}_{i,N}^{\text{sc}}(\mathbf{r}_i)=\frac{\sqrt{-1}}{Z_{\text{out}}}\sum_{n=1}^{N}\sum_{m=-n}^{n}a_{nm}^{i}(N)\mathbf{n}_{nm}^{(4)}(k\mathbf{r}_i)+b_{nm}^{i}(N)\mathbf{m}_{nm}^{(4)}(k\mathbf{r}_i) \tag{A.7}$$

$$\mathbf{H}_{i,N}^{\text{tr}}(\mathbf{r}_i)=\frac{\sqrt{-1}}{Z_{\text{in}}}\sum_{n=1}^{N}\sum_{m=-n}^{n}c_{nm}^{i}(N)\mathbf{n}_{nm}^{(1)}(k_i\mathbf{r}_i)+d_{nm}^{i}(N)\mathbf{m}_{nm}^{(1)}(k_i\mathbf{r}_i), \tag{A.8}$$

where Z_{out} and Z_{in} are the intrinsic impedance of surrounding medium and that inside the i^{th} particle, respectively.

The unknown coefficients, a_{nm}^{i}, b_{nm}^{i}, c_{nm}^{i}, and d_{nm}^{i} are determined by matching the boundary conditions on the surface of the particles. Here we numerically match the boundary conditions in a least squares sense [107], *i.e.* we calculate the unknown coefficients that minimize a squared norm as

$$\Omega(N)=\sum_{j=1}^{J}\frac{\int_{S_{\text{P},j}}|\mathbf{v}_{\text{P}}(\mathbf{r}_j')\times\{\sum_{i=1}^{I}\mathbf{E}_{i,N}^{\text{sc}}(\mathbf{r}_j')+\mathbf{E}^{\text{in}}(\mathbf{r}_j')-\mathbf{E}_{j,N}^{\text{tr}}(\mathbf{r}_j')\}|^2\,dS}{\int_{S_{\text{P},j}}|\mathbf{v}_{\text{P}}(\mathbf{r}_j')\times\mathbf{E}^{\text{in}}(\mathbf{r}_j')|^2\,dS}+\frac{\int_{S_{\text{P},j}}|\mathbf{v}_{\text{P}}(\mathbf{r}_j')\times\{\sum_{i=1}^{I}\mathbf{H}_{i,N}^{\text{sc}}(\mathbf{r}_j')+\mathbf{H}^{\text{in}}(\mathbf{r}_j')-\mathbf{H}_{j,N}^{\text{tr}}(\mathbf{r}_j')\}|^2\,dS}{\int_{S_{\text{P},j}}|\mathbf{v}_{\text{P}}(\mathbf{r}_j')\times\mathbf{H}^{\text{in}}(\mathbf{r}_j')|^2\,dS}, \tag{A.9}$$

where $\mathbf{v}_{\text{P}}$ is unit normal vector on the particle surface $S_{\text{P},j}$. Minimization of the squared norm results in a $K\times K$ ($K = 4(I)(N)(N+2)$) matrix equation [107]. The discretization of the squared norm is important from a numerical point of view and the discretization rule can be found elsewhere [107]. Once we obtain the expansion coefficients by solving the matrix equation, we can determine the field distributions inside and outside the particles by substituting these coefficients into Eq. (A.5) - (A.8). For a multi-particle array, the convergence on the number of basis functions used in the expansion was checked, and the typical number required for our calculations was N = 7-10. Once the electromagnetic field is calculated using GMT, we integrate the MST on a closed surface $S_{\text{M},i}$ outside the particles numerically to obtain the optical force acting on the i^{th} particle. For the closed

surface $S_{M,i}$, we choose a concentric sphere surface with radius b (>a) which surrounds only the i^{th} particle as shown in Figure 41. In our simulation, we assume that the counter-propagating beams are mutually incoherent [81, 84]; this is a reasonable assumption given that the laser diodes are separated by over 1 m of fiber in the experiments. As an example of computation time, when scattering by 7-particles was calculated, the memory requirements for the matrix calculation was 480 MB and the computation lasted 16 hours using a 1.6 GHz PowerPC 970 single processor.

Dynamic Simulation

To calculate the equilibrium positions for a large-number particle array and to investigate the dynamics of the particles in the array, we perform a dynamic simulation. The dynamic simulation can be performed by solving the equation of motion,

$$\frac{d\mathbf{R}_i}{dt} = \mathbf{v}_i, \tag{A.10}$$

where $\mathbf{R}_i$ and $\mathbf{v}_i$ are the centre position and the velocity of the i^{th} particle, respectively. To include all-to-all hydrodynamic coupling between particles [111], we approximate the velocity $\mathbf{v}_i$ using the Oseen tensor $\ddot{\mathbf{H}}$ [144],

$$\mathbf{v}_i = \sum_{j=1}^{I} \ddot{\mathbf{H}}_{ij} \mathbf{F}_j, \tag{A.11}$$

where F_j is the optical force acting on the j^{th} particle and

$$\ddot{\mathbf{H}}_{ij} = \frac{\ddot{\mathbf{I}}}{\zeta} \delta ij + \frac{3a}{4\zeta r_{ij}} (1 - \delta ij) \left(\ddot{\mathbf{I}} + \frac{\mathbf{r}_{ij} \mathbf{r}_{ij}}{r_{ij}^{\,2}} \right). \tag{A.12}$$

Here $\zeta = 6\pi\eta a$ is the friction coefficient (with viscosity of the surrounding medium η and PSM radius a), δ_{ij} is Kronecker delta, and r_{ij} is the displacement vector between the i^{th} and j^{th} PSM, where $r_{ij} = |\mathbf{r}_{ij}| = |\mathbf{r}_i - \mathbf{r}_j|$. With viscous damping being inherently strong in this microfluidic system, inertial effects were neglected and the optical force was equated to the Stokes' drag force to find the velocity of each particle. The first term in Eq. (A.12) represents the viscous drag and the second term represents the hydrodynamic interaction between the PSMs. This hydrodynamic coupling is required since the fluid displaced by

one particle will interact with other particles in the system. To evaluate Eq. (A.10) numerically, we use an Euler integration method, *i.e.* the position at time t = $(m+1)\Delta t$ is determined by

$$\mathbf{R}_i^{m+1} = \mathbf{R}_i^m + \mathbf{v}_i^m \Delta t, \ (m = 0,1,2,3\cdots), \tag{A.13}$$

where Δt is an appropriate time increment.

Numerical Results

In the following numerical calculations, we use a fifth-order Gaussian beam [145] to simulate the divergent beam emitted from the optical fibers. The waist radius and the wavelength are set at w_o = 3.0 μm and λ = 980 μm in free space, respectively, and the distance between the two fibers is set at D_{bf} = 160 μm. The radius and refractive index of the particles are 0.5 μm and 1.574, respectively, and the refractive index of the surrounding water medium is 1.33.

Equilibrium spacing of two- and three- particle arrays

The equilibrium spacing for the two- and three-particle array can be obtained by calculating the optical force as a function of distance between neighbouring particles and locating a point where the optical forces are zero. To verify the proposed MST-GMT numerical method, equilibrium spacing for the two- and three-particle array are compared with experimental results and with numerical results obtained by MST using a finite difference time domain method (MST-FDTD). For cases requiring MST-FDTD, a commercial FDTD software package, FDTD Solutions, provided by Lumerical Solutions Inc. [146] was used. In this section, we consider the case of perfectly aligned beam axes ($D_{off} \neq 0$) with particles trapped symmetrically between the axes.

Figure 42(a) shows optical forces acting on a pair of particles when the spacing between particles, *d*, is changed from 2 μm to 20 μm. A modulation was found in the force calculations, as reported previously [44]. For the conditions of our experiment, the modulation is small so it does not modify significantly the large-scale dynamics. As shown in Figure 42(a), good agreement exists between the MST-GMT and MST-FDTD method. As the spacing, *d*, is increased, the absolute value of the forces acting on

particles 1 and 2 decrease and the forces take opposite sign after crossing the zero force line around d = 9.4 μm. For d < 9.4, particles repel each other, while for d > 9.4 μm, particles attract. For d = 9.4 μm, the net force acting on the particles is zero, and the calculated equilibrium spacing for the two particles is $d_{2,cal}$ = 9.4 μm. This spacing is in good agreement with the experimental result, $d_{2,exp}$ = 9.6 μm. In Figure 42(b), forces acting on a three-particle array are shown, where the centre particle is fixed at z = 0 and the distance, d, between this particle and the neighbouring particles is varied. In this case, the calculated equilibrium spacing is around $d_{3,cal}$ = 8.3 μm and is also in good agreement with experimental result $d_{3,exp}$ = 8.0 μm. In agreement with Ref. [12], our experimental and numerical results show inhomogeneous equilibrium spacing for a two- and a three-particle array, *i.e.* the equilibrium spacing of a two-particle array is larger than that of a three-particle array. Equilibrium forces were calculated for different refractive index values (n = 1.64, 1.74, 1.84), however, substantial changes in the results were not observed.

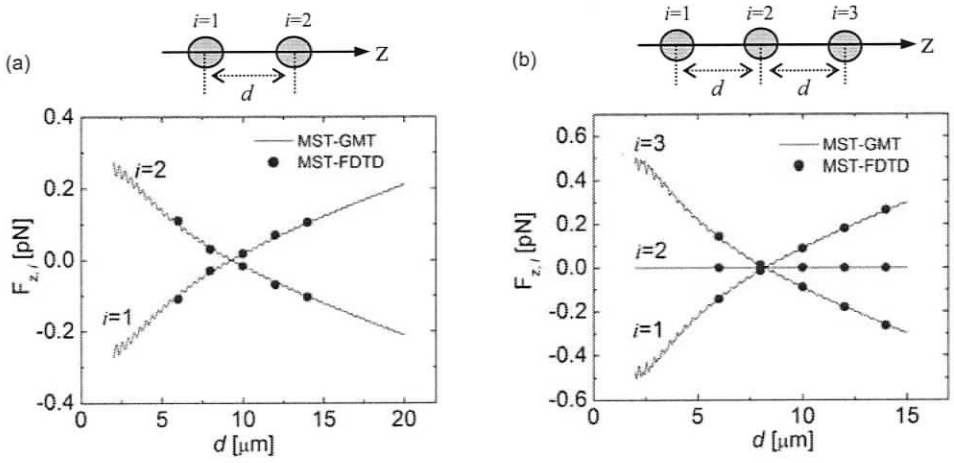

Figure 42 Optical forces acting on trapped particles as a function of distance between neighbouring particles. Solid lines and blue dots are results obtained using MST-GMT and MST-FDTD, respectively [15]. (a) Two-particle array. (b) Three-particle array.

Equilibrium positions of an N-particle array

To calculate the equilibrium positions of an array consisting of more than three-particles, the dynamic simulation proposed previously is used. The case of perfectly aligned beam axes (D_{off} = 0) is considered, where particle motion is confined to the z-axis.

Figure 43(a) shows the results of this dynamic simulation. Simulation results with and without hydrodynamic interaction are displayed simultaneously, where red lines represent the inclusion of HDI, and blue lines without. The force without HDI is calculated by neglecting the second term in Eq. (A.12). This does not correspond to a real physical system, but it is useful for observing quantitative changes in the dynamics that result from modifications to the physical model. At $t = 0$, the 1st particle is initially located at an equilibrium position, $z_{1,1} = 0$, and a 2nd particle is introduced 20 μm away from the 1st particle, at $z = 20$ μm, to model an incoming particle. As the 2nd particle is introduced, the two particles shift in the negative z-direction and settle at their new equilibrium positions, $z_{2,1} = -4.7$ μm and $z_{2,2} = 4.7$ μm, which yields an equilibrium spacing $d_{2,\mathrm{dyn}} = 9.4$ μm. This result is identical to results obtained in the previous section, where $d_{2,\mathrm{cal}} = 9.4$ μm. Once the two particles have settled, a 3rd particle is introduced 20 μm from the 2nd particle ($z = 4.7 + 20$ μm) at $t/\eta(T)/10^3 \approx 0.9$ m^2/N, where $\eta(T)$ is the viscosity of water as a function of temperature T [122]. The two previously stable particles shift in the negative z-direction and settle to their new equilibrium positions, $z_{3,1} = -8.3$ μm, $z_{3,2} = 0$ and $z_{3,3} = 8.3$ μm, for the 1st, 2nd, and 3rd particles, respectively, resulting in an equilibrium spacing $d_{3,\mathrm{dyn}} = 8.3$ μm. This result also matches the value obtained in the previous section, where $d_{3,\mathrm{cal}} = 8.3$ μm. Extending this procedure to a 13-particle array, which was the critical number in the experiments that lead to array oscillations, equilibrium positions for a 13-particle array were calculated as shown in Figure 43(b). At $t = 0$, 12 particles are initially located at their equilibrium positions and a 13th particle is introduced 20 μm from the 12th particle. As in the previous case, the 13 particles settle to their new equilibrium positions and the onset of the spontaneous oscillation does not occur for this model containing perfectly aligned beam axes. The results with and without HDI do not show significant deviation for a collinear dual-fiber arrangement; however, the results differ significantly for offset beams. Even for perfect alignment, it is clear that HDI has a stronger influence for more closely spaced particles, as expected from Eq. (A.12). For example, the deviation between the equilibrium-approach with and without HDI for 4 particles is greater than for just two as in Figure 43(a).

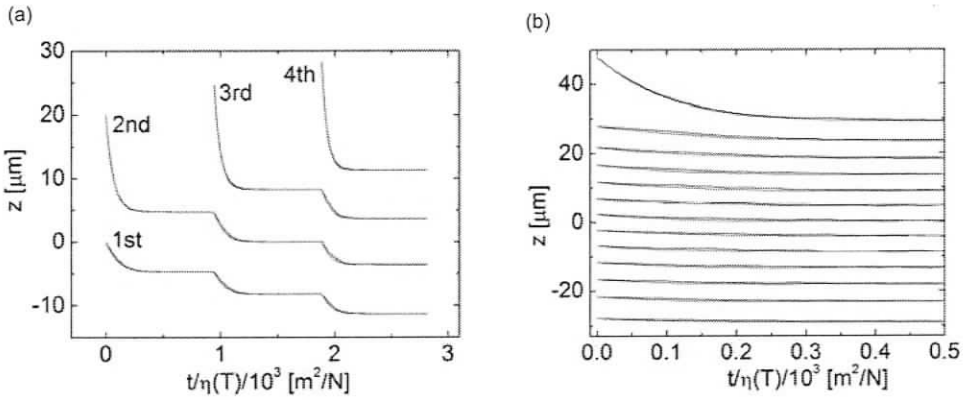

Figure 43 Trajectories of particles obtained by the dynamic simulation. Red and blue lines are the results with and without HDI, respectively [15]. (a) From two- to four- particle array. (b) Thirteen-particle array.

Dynamic Simulation of Spontaneous Oscillation

Here, we consider the case of a transversely misaligned model ($D_{off} \neq 0$, §6.4) which results in spontaneous oscillation as observed in the experiment. We assume that the axis of a beam propagating in the positive z-direction lies on the z-axis and that propagating in the negative z-direction is located on a parallel axis with an offset in the positive x-direction (D_{off}, as shown in Figure 41). Due to this beam offset, the particles are free to move in x-z plane. Calculations were performed using the procedure mentioned previously. First, a particle is positioned at the equilibrium position, *i.e.* $(x_1, z_1) = (D_{off}/2, 0)$, and a second particle is introduced at $(x_2, z_2) = (D_{off}, 20\ \mu m)$ to model an incoming particle. Once the second particle is added, the two particles move towards their new equilibrium positions and settle as described previously. After settling, a third particle is added and this procedure is iterated for up to 7 particles. The results of the dynamic oscillation are provided in §6.4.